University of California

Los Angeles

Search for Heavy Stable Charged

Particles with the Compact Muon
Solenoid Detector at the Large Hadron Collider

A dissertation submitted in partial satisfaction

of the requirements for the degree

Doctor of Philosophy in Physics and Astronomy

by

Christopher Patrick Farrell

2013

The dissertation of Christopher Patrick Farrell is approved.

_____

Other person

_____

Michael Gutperle

_____

David Saltzberg

_____

Jay Hauser, Committee Chair

University of California, Los Angeles

2013

ii

I guess I have to write something here

TABLE OF CONTENTS

List of Figures

List of Tables

Acknowledgments

Thanks for money

Vita

2008   B.S. (Physics), University of Florida.

PUBLICATIONS

A lot How many do I list here?

Abstract of the Dissertation

Search for Heavy Stable Charged

Particles with the Compact Muon
Solenoid Detector at the Large Hadron Collider

by

Christopher Patrick Farrell

Doctor of Philosophy in Physics and Astronomy

University of California, Los Angeles, 2013

Professor Jay Hauser, Chair

HSCPs

CHAPTER 1

Introduction

I wrote a thesis

CHAPTER 2

Theoretical Motivation

2.1 Introduction

Where I found this info

2.2 Standard Model

Fermions and bosons and shit

2.2.1 Cosmic rays

Discuss here so I don't have to in background section

2.3 Beyond Standard Model

SM issues, SUSY

2.4 Conclusion

Recap

CHAPTER 3

Experimental Apparatus

3.1 Introduction

The apparatus used for this paper is larger than how the term is normally used. Protons are accelerated and brought to a collision by the Large Hadron Collider (LHC) located outside Geneva, Switzerland spanning the Swiss-French border. The protons are accelerated in smaller linear and cyclical accelerators before being injected into the LHC. The protons are brought to a collision at four spots insode of the LHC. Surrounding one of these spots is the Compact Muon Solenoid (CMS) detector. The CMS detector consists of multiple which work together to identify signatures of different types of particles.

3.2 Large Hadron Collider

A full description of the LHC can be found can be found in Reference [6], a short summary is included here. The LHC is a two-ring superconducting synchotron designed to collide particles at high energy and high luminosity. It sits in 26.7 km tunnel located 45-170m underneath the French-Swiss border outside of Geneva, Switzerland. The LHC can create collisions with either protons or heavier ions. This leads to three possible operational modes, proton-proton, ion-ion, and proton-ion. Only in proton-proton operational mode is there a possibility to

discover HSCPs and it is the only mode discussed in this paper.

The LHC was designed to accelerate protons to an energy of seven TeV and collide them at a center of mass energy($\sqrt{s}$ of fourteen TeV with an instantaneous luminosity of $10^{34}cm^{-2}s^{-1}$. The protons are brought to a collision at four points along the LHC beamline. Surrounding two of these interaction points sit the general purpose detectors of CMS and ATLAS. These points are meant to recieve the highest instantaneous luminosity the LHC can supply. The other interaction points are surrounded by the special purpose detectors LHCb and ALICE and are designed to have instantaneous luminosities of $2 \times 10^{29}cm^{-2}s^{-1}$ and $10^27cm^{-2}s^{-1}$, respectively. This paper considers data collected by the CMS detector.

The acceleration of protons to their final energy of 7 TeV is done in series of steps employing smaller accelerators located on the CERN campus. The protons originate in the linear accelerator Linac2 where they are passed through a series of synchotron accelerators, Proton Synchotron Booster, Proton Synchotron, and Super Proton Synchotron, with their energy raised to 1.4 GeV, 25 GeV, and 450 GeV, respectively. After passing through the Super Proton Synchotron the protons are passed into the LHC. The LHC then accelerates the protons to their final design energy of 7 TeV.

The beams are designed to contain proton bunches spaced such that collisions at the interaction points every 25ns. The LHC can hold a total of 2,808 bunches, in some places there are gaps larger than 25ns between bunches to allow for dumping of the beam without harming the LHC. Each collision between the proton bunches can result in more than one proton-proton collision. This results in the the detectors around the LHC interaction points seeing numerous proton-proton collisions overlayed on one another. The effect of this on the search for HSCPs is discussed in Section 5.10.

The commsioning of the LHC saw it run at a progression of lower energies building towards the design energy. In 2008 the LHC was run at $\sqrt{s} = 900$ GeV and for a short period at 2.36 TeV. Then after further work on the LHC the energy was raised to 7 TeV for both 2010 and 2011 and then to 8 TeV in 2012. This paper only covers the data collected at 8 TeV in 2012. It is planned to raise to raise the energy to its design goal of 14 TeV through additional work on the LHC and the injector system.

Similarly, the instantaneous luminosity was ramped during the commisioning phase. During the 2012 running the machine ran with the proton bunches separated by 50ns. The instantaneous luminosity was normally at approximately $7 \times 10^{33} cm^{-2} s^{-1}$. With 50ns spacing this means that the per bunch luminosity actually the design value. It is planned to run with 25ns bunch spacing in future running with CMS.

3.3   Compact Muon Solenoid

The CMS detector is built around one of the interaction points of the LHC. A full description of CMS be found in References **??** and **??**.

CMS was designed to be a general purpose detector that would have sensitivity to a wide range of physics. This is important for the HSCP search as the detector is used in ways not typically done in most CMS analyses. The central feature of CMS is a superconducting solenoid magnet with a 6m diameter and 13m length that provides a 4T magnetic field. The return field from the solenoid is powerful enough to saturate 1.5m of iron, this allows for a strong magnetic field to be present outside of the solenoid. CMS has a cylindrical shape with an onion like design where inner subdetectors are nested inside of outer ones. From inside out
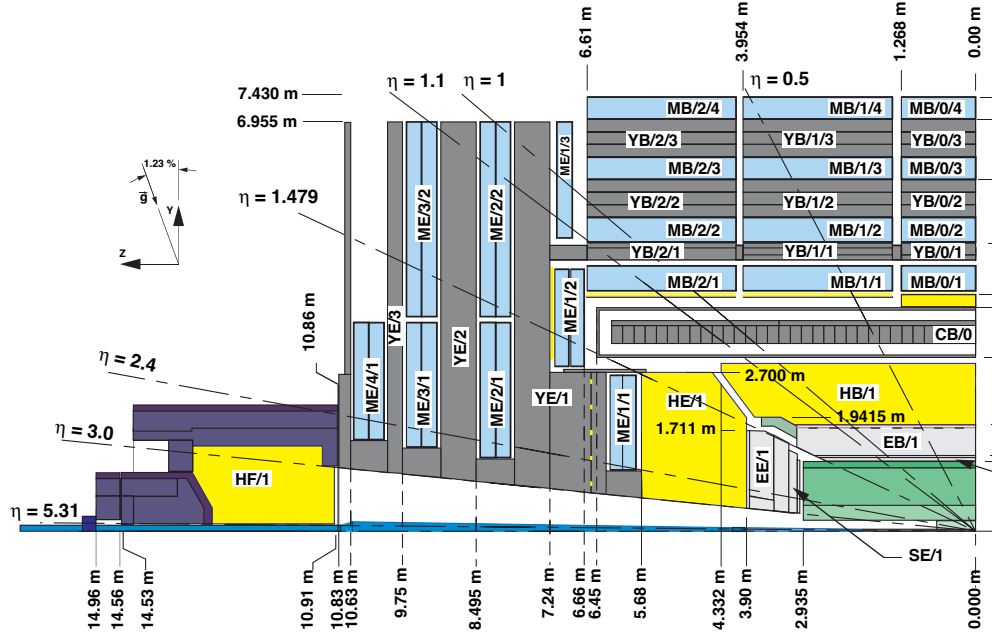
Figure 3.1: Particles traversing CMS

those subdetectors are an all silicon tracker, an electromagnetic and hadronic calorimeter, the magnet, and finally the muon system. The various subdetectors and their role in identifying SM particles can be seen in Figs 3.2 and 3.1.

CMS employs a right handed coordinate system with the x-axis pointing to the center of the LHC ring, the y-axis pointing vertically upward, and thus making the z-axis be along the beam line pointing in the clockwise direction if looking at LHC from above. The azimuthal angle, θ, is defined relative to the z-axis. The variable psuedorapidity, η, is defined as $\eta = -\ln\left[\tan\left(\theta/2\right)\right]$. The polar angle, ϕ, is defined relative to the x-axis, meaning that vertically upward, downward has a ϕ value of $\pi/2$, $-\pi/2$.

The possibility that a HSCP can interact with the detector and change its charge means that it may not look like any of the particles in Figure 3.2. The particle may be produced neutral and only gain charge as it passes through the

6
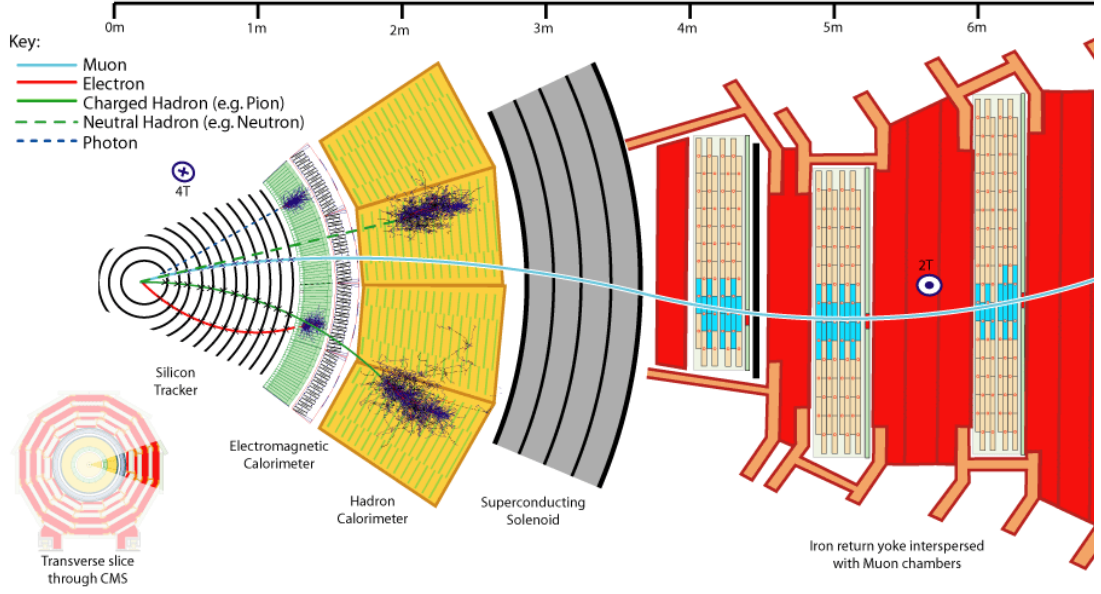
Figure 3.2: Identification of SM particles in CMS

calorimeter. The only record of its hits will be in the muon system giving the signature shown in Figure 3.3. To discover HSCP of this type it is necessary to conduct a search which does not require any hits in the inner portion of CMS. A search of this type is presented in Chapter 5.

3.3.1 Subdetectors

The innermost part of CMS is an all silicon tracker. Closest to the interaction point are pixel detectors with three barrel layers and two endcap disks,totalling 1,440 modules. Outside of this are strip detectors with ten barrel layers and three plus nine endcap disks. It extends up to a psuedorapidity range of 2.5 with the resolution on track p_T being approxiamtely 1.5% for 100 GeV/c particle at $|\eta| = 1.6$ and growing larger at high $|\eta|$ due to the decreased lever arm. Both the strips and the pixels have an analog readout of the deposited charge with a

7
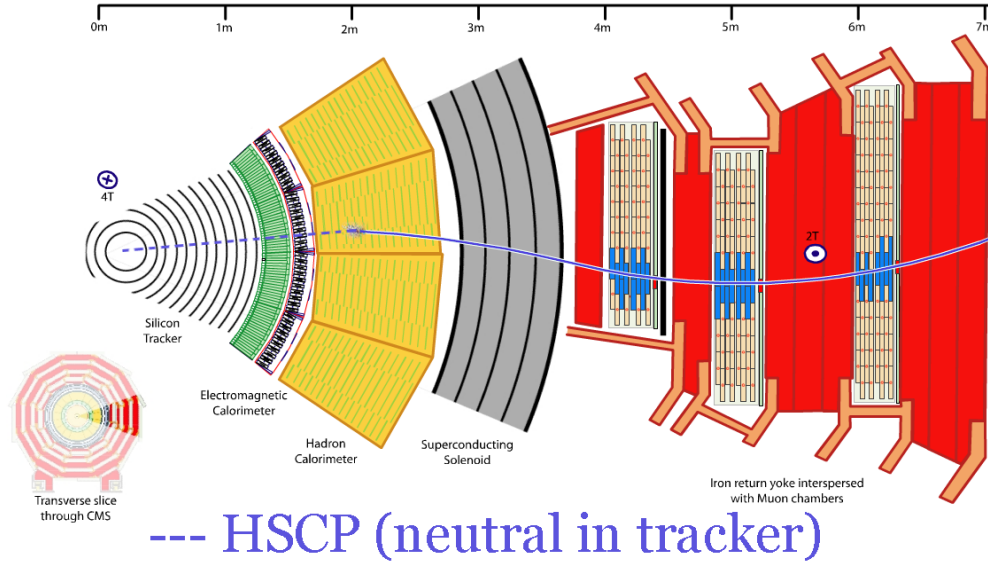
Figure 3.3: HSCP becoming neutral in CMS.

maximum readout of roughly three times the charge expected to be deposited by a muon. Charge from particles traversing the inner tracker is expected to be spread out among multiple modules in the same layer allowing the position of the particle to be calculated more precisely then simply the center of the module. The charge sharing also allows the possibility to identify hits where two particles have overlapped.

Outside of the muon system is the calorimeter. The purpose of the calorimeter is to measure the energy of particles and aid in their identification by stopping particles at different points in the calorimeter. The calorimeter is split into an inner electromagnetic calorimeter (ECAL) and an outer hadronic calorimeter (HCAL). The ECAL is made of 75,848 lead tungstate ($PBWO_4$) crystals split between the barrel and endcap. As particles lose energy in the ECAL the crystals emit scintillation light which is collected by photodetectors. The HCAL consists

of plates of brass absorbers interleaved with scintillator detectors. Electrons and photons are likely to stop in the ECAL where they deposit all of their energies. Hadrons, electrically charged or neutral, will deposit some energy in the ECAL but will deposit most in the HCAL where they are very likely to come to a rest. Muons will deposit of the order of two GeV of energy in the calorimeter and are generally the only charged SM particles that are able to exit the calorimeter.

The outermost part of the detector is the muon system which is split into three parts, Cathode Strip Chambers(CSC), Drift Tubes(DT), and Resistive Plate Chambers(RPC). The CSC cover the forward part of the detector with $|\eta| > 0.9$ while the DT and the RPC cover the barrel portion extending up to $|\eta|$ of 1.2 and 1.6, respectively. The muon system is comprised of four stations of chamber with the lead for the magnet return yoke inbetween the stations. The magnet return yoke provides a magnetic field in the muon system.

CSC chambers have a trapezoidal shape with six alternating layers of cathode strips and anode wires arranged in a nearly orthogonal pattern. The strips run radially away from the beam line and measure the ϕ of hits while the wires measure the radial position of hits. Charge collected on the wires is passed to a constant fraction discriminator which outputs a 40ns pulse. The pulse is sampled every 25ns and this sampling is readout. The amount of charge on the strips is readout every 50ns. The charge is used offline to get a more precise estimate of the position and time of the hit.

DT chambers have two or three superlayers which themselves are composed of four layers of drift cells which are staggered by half a cell. All of the DT chambers have two superlayers oriented parallel to the beam line measuring, these superlayers measure the position of particles in the $r - \phi$ plane. The three inner stations additionally have a superlayer running perpendicular to the beamline to

9

measure the position of particles in the $r-z$ plane.

RPC chambers are gaseous parallel plate detectors that can provide a time resolution of 2ns, which is much smaller than the design LHC spacing of 25ns allowing for a very high efficiency to correctly tag an event with the correct bunch crossing, and a spatial resolution sufficient to be able to associate RPC hits with hits from the other muon subdetectors.

3.3.2 Computing

The rate of proton-proton collisions inside of CMS is too large for all of them to be readout and stored offline. To deal with this CMS employs a two level trigger that selects interesting events online. The level one (L1) trigger must reduce the rate of events readout to less than 100,000 Hz in less than three μs requiring a completely firmware based approach. Events are selected by a variety of algorithms but most of them look for a high momentum track in the muon system, large amount of energy in the ECAL or HCAL, or a combination of these. Signals from these systems trigger the readout of the rest of detector with through the Data Acquisition (DAQ) infrastructure for the event. As the LHC was designed to operate with 25ns spacing many of the subsystems, the tracker especially, only readout the data in the 25ns window associated with the event. That means that triggers that pre or post-fire will not contain much of the data from the event. This can be issue for HSCP that are travelling so slowly that they reach the muon system in the time window associated with the next. However, a special configuration of the RPC trigger exploits the fact that current running of the LHC has been done with at least 50ns spacing

All hits in the RPC are sent to the trigger electronics (PAC) twice, once for the bunch crossing prior to the one it is associated with and also for the one it

10

is associated with. From there the trigger electronics treat the advanced RPC hits in the same manner as they do all other hits. The result is that the RPC signals to the readout the event both in the event it arrived in and the one before it. This means that HSCP which arrive to the muon system up to 37.5ns after a muon is expected to would still trigger the readout of the data in the rest of the detector corresponding with the bunch crossing it was created in. Despite the RPC signaling to readout two events only one will ever be actually collected as readout of consecutive events is forbidden by the DAQ. To ensure in-time muons still maintain the correct behavior, accept signals sent for the bunch crossing immediately preceding a bunch crossing with protons passing through CMS are rejected. So signals from in-time muons will attempt to pre-fire but this will be vetoed and the correct event will be readout. A schema illustrating this behavior is shown in 3.4. This configuration is only possible when proton collsions are spaced by at least 50ns so that accept signals from successive bunch crossings can be unambiguously classified.

The next step in the trigger is the High Level Trigger (HLT) which must reduce the number of events to a few hundred Hz in the order of a second. The HLT is software based and there are a wide variety of algorithms used to identify interesting events and store them for offline analysis. The HLT is split into two different phases, Level 2 (L2), and Level 3 (L3). The L2 step is mostly concerned with confirming the L1 decision and reducing the rate so that higher level objects can be built within the time restrictions. The L3 step builds these objects, often reconstructing tracks of particles in the inner tracker and matching them to objects in other parts of the detector, and then applies cuts on the objects selecting which events to pass for storage at computers located at CERN and throughout the world.
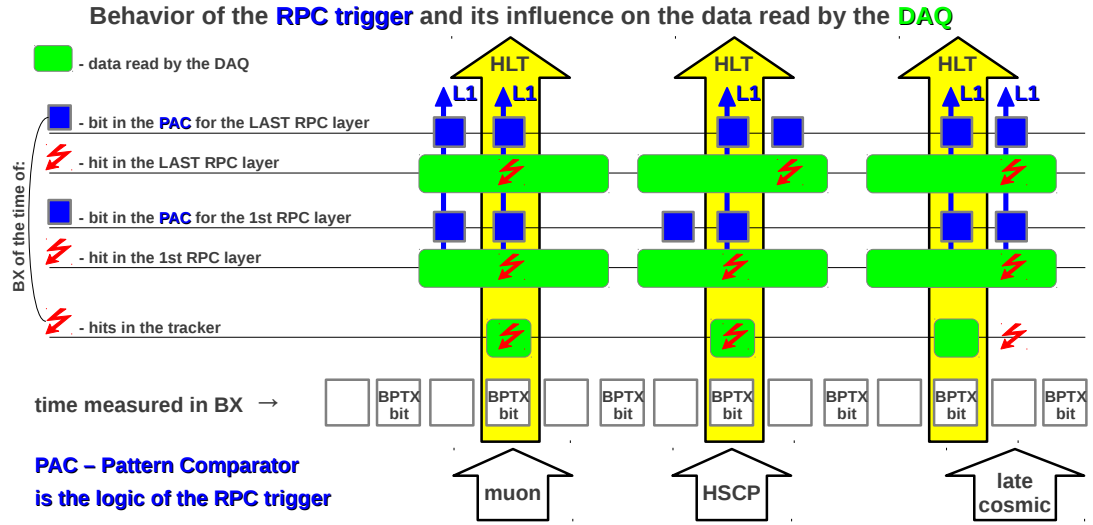
Figure 3.4: Schema of a temporal behavior of the RPC trigger and its influence on the data read by the data acquisition system. Time measured in BX quanta goes from left to right. The results of appearance of three (separate in time) objects of different type is shown: pp collision muon, HSCP which is delayed by one BX at the exit from the muon system and outward going cosmic muon delayed by one BX with respect to muons from pp collision. Each hit (read bolts) in the RPC is advanced by one BX and duplicated (blue squares) in the PAC (Pattern Comparator, chip in which main part of the RPC trigger logic is implemented). Only first and last RPC layers are shown. A coincidence (pattern) of bits in the PAC in the same BX gives L1 trigger (blue arrows). But to obtain the HLT trigger a coincidence of the RPC L1 trigger with BPTX bit is required (yellow arrows). DAQ reads tracker data from HLT selected BX and RPC data from adjacent BXs (green rectangles). Both pp mouns and (not too slow) HSCPs give HLT trigger. Outward cosmic muons, which are late by one BX, also give HLT trigger (rightmost yellow arrow), but its tracker hits are not selected. Such cosmic muons will not become global muons.

CMS maintains a software, CMSSW, which attempts to reconstruct the particles in the event, identify them as one of the long-lived SM particles, give a multitude of information about the particle, and apply any necessary calibration constants. The code also calculates event level quantities such as the total momentum of all the particles in the event. After all this the data size is at the scale of PB which is too large for offline analyzers to run over frequently. To deal with this copies of the data are produced dropping lower level quantities and selecting only events that a particular analysis is interested in studying.

CMSSW is also tasked with simulating how particles, coming from both SM processes and new physics, would interact with the detector so that this can be used to compare against data. The simulation has two steps before it reaches point that it has the same format as data read out from the detector, at that point it follows the same chain with the only allowed difference being calibration constants. The first step is the simulation of the proton-proton collision and the particles that are created from it, the detector is not used at all in this step. The next step is the simulation of these particles with the detector and how the detector electronics handles this data, including the L1 trigger. From there the simulation is handled the same as data.

CHAPTER 4

Muon System Timing

4.1 Introduction

Muons coming from collisions in the LHC take approxiamtely 25-40ns to travel from the interaction point to the muon system. As CMS was designed to collect data with protons colliding every 25ns the time of flight (TOF) of muons is a significant time interval. The muon system must be able associate tracks in the system to the correct bunch crossing at L1 to trigger the readout of the data in the rest of the detector associated with the collsion that the track came from. The method to determine timing synchronization of the CSC subdetector is described below.

Additionally, the timing in the muon system can be used to separate out different sources of tracks in the muon system. These sources include collision muons from the triggered bunch crossing, muons from adjacent bunch crossings, muons from cosmic rays, muons travelling with the proton beams in the LHC, and possibly HSCPs predicted in theories of new physics. To do this the time of hits in the muon system is measured and a combined time for each track is calculated.

4.2 CSC Hit Timing

Hits in the CSC are found from a combination of signals from the anode wires and cathode strips. Both of the signals can be used to estimate the time of the hits.

Time is measured by the cathode strips in two ways, one for online use in the L1 trigger and one for offline measurement. The online measurement finds the peak of the charge distribution and associates it with a particular bunch crossing. To determine the position and time of the hits offline the charge on cathode strips is sampled every 50ns. The time of the hits is estimated with a five pole fit to the charge. Calibration constants are subtracted from the times during reconstruction to center the times at zero. The constants are found for each chamber and are derived from times associated with high quality, high momentum muons. Cathode times have a resolution of approxiamtely 7.0ns.

As stated in Section 3.3.1, signals from the anode wires are passed to a constant fraction discriminator which outputs a 40ns pulse that is then digitized every 25ns. Depending on when the pulse starts the hit can have either one of two bits being high. Given the same first high bit it can be inferred that hits with the next bit low arrived earlier than hits with the next bit high. Thus, it is possible to estimate the time of anode hits with a 12.5ns quantization. The anode times are calibrated to have a mean of zero in the same method as per the cathode times. The resolution of the anode hit timing is approximately 8.6ns

The distribution of the time of anode and cathode hits is shown in Fig 4.1. As can be seen in the right plot the anode time has a large tail of positive times. This is dealt with by a cleaning procedure defined below.

CMSSW takes the anode and cathode hits in a chamber and reconstructs a

Figure 4.1: Left column: Distribution of cathode time of hits. Right column: Distribution of anode time of hits. Top row: Linear scale. Bottom row: Log scale.
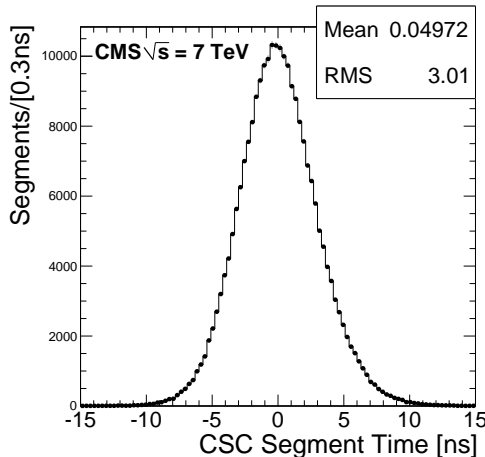
Figure 4.2: Times of segments associated with high quality muons.

segment which is meant to represent the passage of the particle through the chamber. A time is associated with the segments by averaging the anode and cathodes times associated with the segments. The times are weighted by one over their variance To remove the large tail of anode hits a cleaning procedure is applied to the times, both anode and cathode, to remove outlier hits. The procedure removes anode times more than three sigma different from the average. The times of segments associated with high quality muons is shown in Fig. fig:SegTimes. The resolution on the segment times is 3.0ns.

4.3 CSC Trigger Timing

The CSCs are a key component of the L1 trigger system and it is important that they associate tracks in the system with the correct LHC bunch crossing. The CSCs build tracks for the L1 trigger with the CSC Track Finder (CSCTF) by combining track stubs coming from the CSC chambers. The stubs are associated with a particular bunch crossing and the track finder uses majority logic of the

stubs used to build the track to associate the track with a bunch crossing. In cases where there are an equal number of stubs from different bunch crossings, say two track stubs coming from adjacent bunch crossings, the CSCTF preferentially selects the later bunch crossing.

As mentioned in Section 3.3.1, there are six layers of cathode strips and anode wires in a CSC chamber. Electronics on the chamber collect hits from the cathode strips and anode wires and separately create trigger primitives called Cathode Local Charged Track (CLCT) and Anode Local Charged Track (ALCT), respectively. The two separate trigger primitives are then combined to form a Local Charged Track (LCT). The trigger primitives must be associated with events within three bunch crossings of one another to be combined. The bunch crossing that the LCT is associated with is set by the ALCT.

The timing of the ALCT is determined by the timing of the third anode hit, the first high bit, to arrive to the ALCT circuit board. A common offset per chamber can be applied to the anode hits in order to achieve the best synchronization. To determine the offset the arrival time of the anode hits is studied offline using hits from high quality muons. The average time of the anode hits can be correlated with the probability for a chamber to produce an ALCT in the bunch crossing before it should (pretrigger) and after it should (posttrigger). The offsets for each chamber can be tuned to give an expected pretrigger and psttrigger probability.

However, the CSCTF logic means that simply setting the offset to give an equal probability to pretrigger and posttrigger is not optimal. This can be seen by looking at the case where the CSCTF only receives two track stubs, this is also the case where the CSC online timing is most important. If the CSCTF receives one LCT in the bunch crossing before the collision and one in the correct bunch

crossing it will preferentially choose the later LCT and associate the combined track with the correct bunch crossing, in order to pretrigger the readout of the event more than one LCT must arrive early. On the other hand, if it recieves one LCT in the correct bunch crossing and one in the proceeding bunch crossing the track will be associated with the bunch crossing following the collision. Thus, the probability to pretrigger the event can be written as P_{LCTPre}^2 while the posttrigger probability can be written as $2 \times P_{LCTPost} - P_{LCTPost}^2$.

Figure 4.3 shows the probabilities to pretrigger and posttrigger both at the chamber level and the expected probability at the CSCTF versus the average anode time of a chamber. The chambers are split into three categories depending on which station and ring they belong to. One category is chambers in the first ring and station, another the chambers in the first ring not in the first station, and the last those not in the first ring. The design of these chambers are all slightly different so it is allowed for them to have different optimal times.

From these plots an optimal value of 204ns is chosen the chambers in the first ring not in the first station and 205ns for all other chambers. The plot of the pretriggering and posttriggering in the track finder somewhat implies an earlier optimal but these are not used for two reasons. The first is that pretriggering grows as the square of the pretriggering probability and since, as described below, the offsets can not be set exactly chambers that are slightly below optimal could lead to significant pretriggering in those chambers. Second, pretriggering prevents the readout of the collision event even by another portion of the detector, CMS can not readout two consecutive, while posttriggering does not have this issue. For these reasons slightly later times that still have very low posttriggering are used.

The offsets can be moved in roughly two ns steps in the chamber firmware
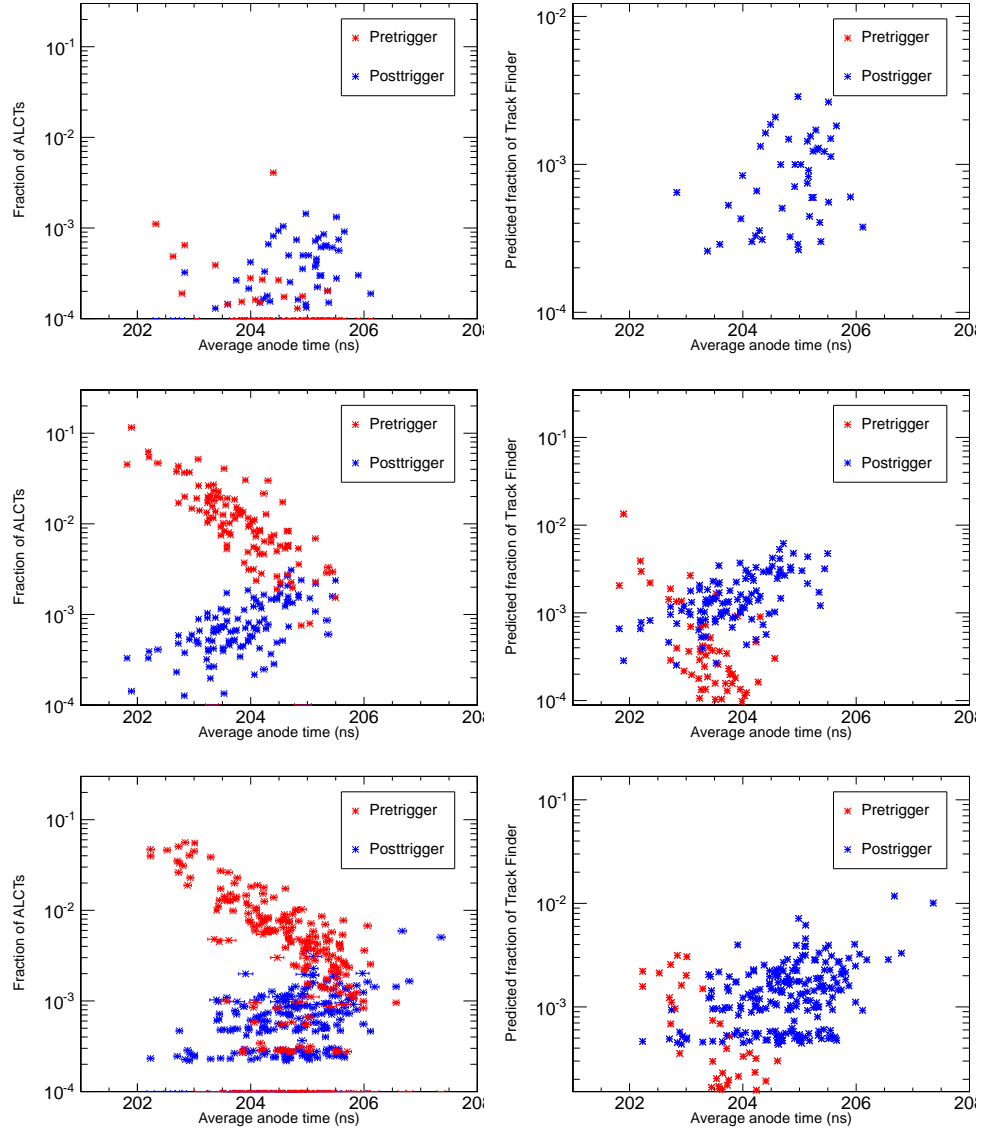
Figure 4.3: Pretriggering and posttriggering versus average anode time.
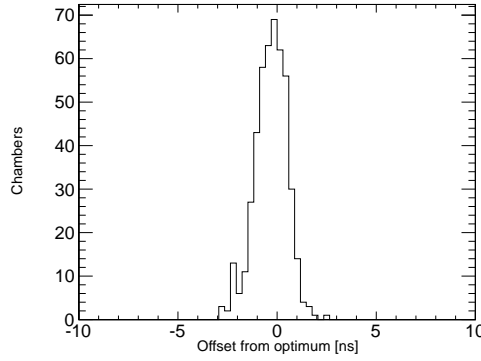
Figure 4.4: Average anode time of chambers relative to optimal values.

with the actual number possibly being different chamber to chamber. Shifting the offsets is a somewhat complicated procedure and carries the risk of accidentally shifting the timing of a chamber by a large amount. Thus, the offsets are changed only when deemed necessary, numerous iterations to get a perfect synchronization is not done. The synchronization with respect to the optimal values for all chambers is shown in Fig. 4.4, most of the chambers are within one ns of the optimal time with none more than three ns off.

After this synchronization procedure is performed the timing of the LCTs is very good. This can be seen in Fig. 4.5 which shows the bunch crossing tagging for LCT matched to high quality muons. The distribution is purposefully made asymmetric to account for the CSCTF logic used further downstream. The efficiency is 99% better than the 92% design requirement.

4.4   Muon Track Timing

Tracks, meant to represent muons or other particles passing through the detector, are built in the muon system connecting together the hits in the different
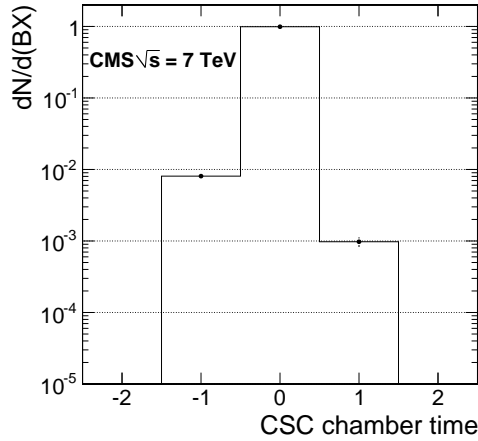
Figure 4.5: Fraction of LCT versus LCT bunch cross assignment relative to collision event

chambers of the CSCs, DTs, and RPCs. Numerous different timing quantities about the track are calculated under three different assumptions on how the particle that track is meant to represent travels between the interaction point and the muon system. Only time measurements from the CSCs and DTs are used to calculate the timing quantities.

A particle of speed, v, travelling along a line, will arrive at a location d, distance relative to some arbitrary origin point of the line, on the line at 4.2

$$t = d/v + t_0 \tag{4.1}$$

where t_0 is an overall offset. When the local timing variables were defined, they were calibrated such that a speed of light, c, particle would have an average time of zero. Thus d/c has already been subtracted from the times so the same quantity must be subtracted from the right hand side of 4.2. Additionally it is easier to work with β^{-1} ($\equiv c/v$) instead of c. With these two Eg. 4.2 now becomes The equation now becomes

$$t = d/v - d/c + t_0$$
$$t = d \times \beta^{-1}/c - d/c + t_0 \qquad (4.2)$$
$$t = (d/c) \times (\beta^{-1} - 1) + t_0$$

The three assumptions relate to how the β^{-1} and t_0 parameters are fixed. The formula has two pieces of input datum, time, t, and distance, d. The distance from the interaction point to the hit location is known to a much better degree than the time of the hit so the uncertainty on the variables comes almost entirely from the time measurement.

The first quantity is the speed of the particle assuming it left the origin at $t_0 = 0$ reducing 4.2 to $t = (d/c) \times (\beta^{-1} - 1)$ or simpler $\beta^{-1} = tc/d + 1$, with the measurement coming from the average of this quantity for CSC and DT hits associated with the track weighted as one over their variance in the same manner as was done to caluclate their segment times. Outlier hits from anode hits are again cleaned in the same manner as per the segment times. The weighting by one over variance and outlier cleaning is performed for all three measurements.

The motivation for using β^{-1} now becomes clear, the β^{-1} measurement is linear with t, the source of the largest uncertainty. This means that β^{-1} will have a much more normal shape than β which would be skewed. The speed of the particle is very useful in separating standard model muons from HSCP produced in new physics as is shown in Section 5. Figure 4.6 shows the β^{-1} measurement for; data, completely dominated by collision muons; cosmic ray muons, the sample is defined in 5; and HSCPs, again sample defined in 5. It can be seen that the data is strongly peaked at one, the cosmic ray muons are roughly flat, while the HSCP have β^{-1} greater than one, indicating they are travelling slowly.
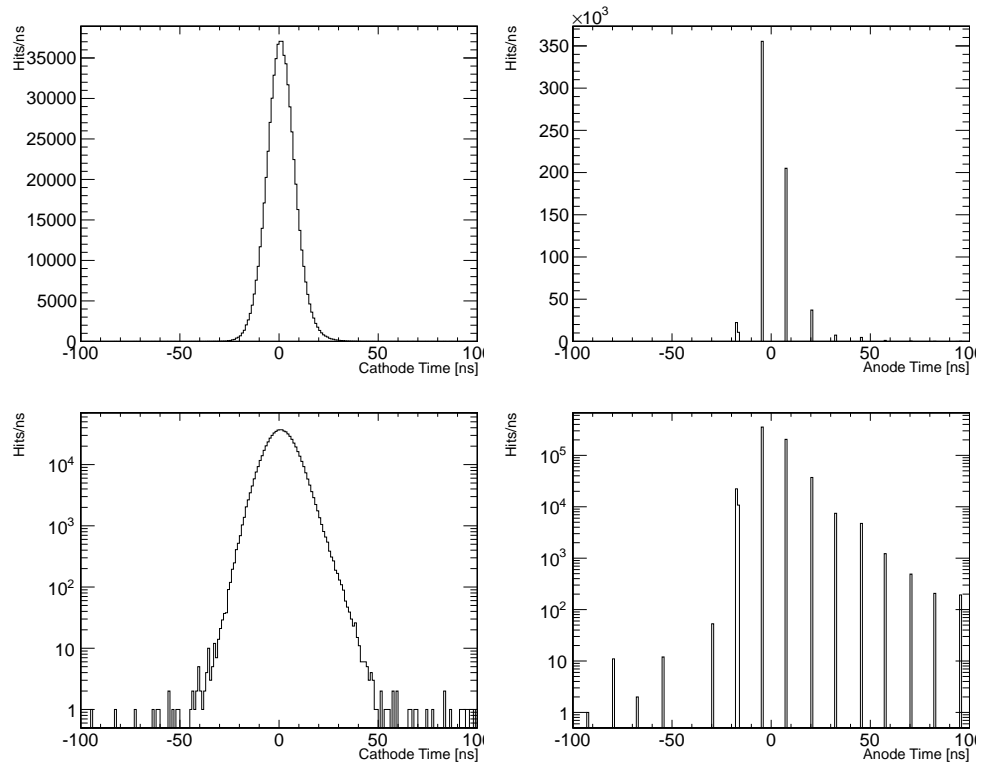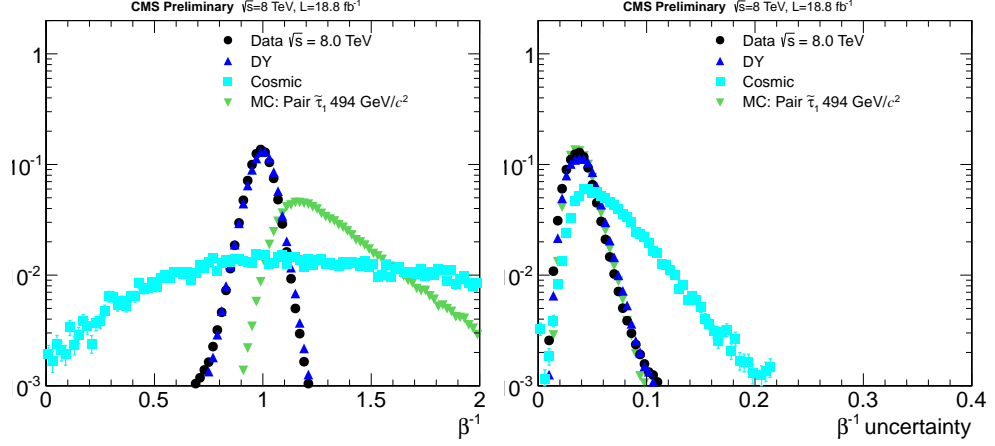
Figure 4.6: Left column: Distribution of cathode time of hits. Right column: Distribution of anode time of hits. Top row: Linear scale. Bottom row: Log scale.

The next quantitiy is the estimated time the particle the track is meant to represent left the interaction point assuming the particle travelled at the speed of light. This means setting β^{-1} to be one in 4.2 reducing the equation to simply $t = t_0$. For muons with at least a modest amount of p_T that are produced in a collision in the triggered bunch crossing this assumption is valid and thus the value should be centered at zero. Figure 4.7 shows the time at vertex for the same three samples as in 4.6.

The next quantity is similar but it assumes the particle is traveling into CMS, such that the parameter t_0 represents the time an incoming particle would have crossed the interaction point. This can be an interesting property because tracks can be found in the inner tracker within a small time window so an incoming cosmic reconstructed in the inner tracker would likely have a t_0 from this measurement near zero. The measurement assumes $\beta^{-1} = -1$ reducing 4.2 to $t = -2(d/c) + t_0$ which can be written to $t_0 = -2(d/c) + t$ which makes it clear that t_0 can be found as the average of this quantity with weights like the previous

24
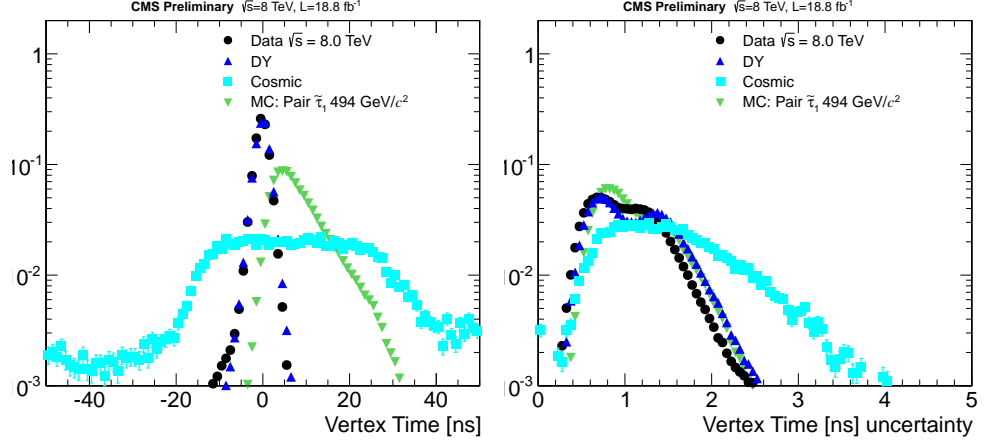
Figure 4.7: Left column: Distribution of cathode time of hits. Right column: Distribution of anode time of hits. Top row: Linear scale. Bottom row: Log scale.

measurement. Figure 4.8 shows the distribution of this time for the same three samples as above.

The question may be asked why not to make a measurement with making any assumptions on t_0 or β^{-1}. This was checked but it was found to have resolution worse by more than an order of magnitude and very little discrimanatory power. This is because the assumptions in the previous measurements allowed all of them to use information related to the beam spot, which is approximately three times as far away from the innermost part of the muon system as the outermost part is to the innermost part. The first two measurements both assumed an error free propagation of the time in the muon system to the interaction point while the β^{-1} measurement added a new point at the interaction point with t = 0. This assumption free measurement is not used for any purpose in CMS.

4.5 Conclusion
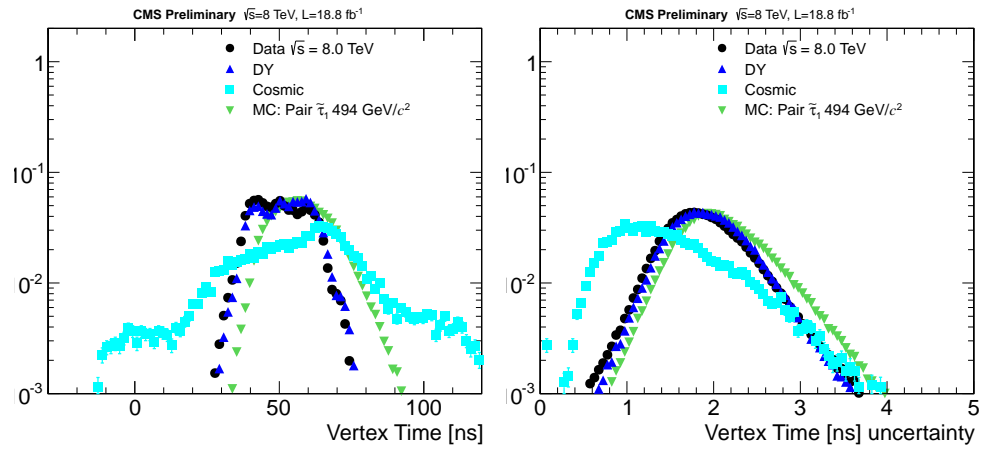
Figure 4.8: Left column: Distribution of cathode time of hits. Right column: Distribution of anode time of hits. Top row: Linear scale. Bottom row: Log scale.

CHAPTER 5

Search for Heavy Stable Charged Particles

5.1   Foreword

The contents of this chapter are included in the paper (cite my own paper) authored by the CMS collaboration. The paper includes five searches for HSCPs in data collected by CMS during 2011 and 2012 running each designed to have sensitivity for various different signatures of HSCP. The work was done in a small group within the CMS collaboration with myself being one of the central researchers. The five searches are all done in the same framework so most of my work was applied to all five analyses. The five searches are labelled *muon only*, *muon+track*, *track only*, *multiple charge*, and *fractional charge*.

For parts of the searches that were different for the five searches I was essentially the only person to work on the *muon only* analysis and contributed largely to the *muon+track*. I worked on the *track only* and *multiple charge* searches to a slightly smaller degree. My work on the *fractional charge* search was mostly limited to work that was applied across all five searches. Therefore this chapter focuses on the *muon only* and *muon+track* searches and with highlighting of the specific parts of the other three searches I worked on.

While the paper included both the 2011 and 2012 data taking periods, the *muon only* analysis only uses the 2012 data. Due to this the 2012 data is the focus of this paper with a statistical combination of the 2011 and 2012 data for

the other four analyses is preseneted at the end of the chapter. The procedure for analyzing the 2011 data is the same as for the 2012 data.

5.2 Introduction

As discussed in section 2.3 new heavy long-lived charged particles are predicted in many extensions to the SM. HSCP with lifetime $\gtrsim$ 40ns are likely to traverse the entire CMS detector before decaying and will thus be directly detectable. A majority of HSCPs with mass $\gtrsim$ 100 GeV/c^2 will have a velocity, $\beta \equiv v/c$, less than 0.9. As no heavy long-lived particles are present in the SM, HSCPs would be the only high momentum particles produced at the LHC with β not very close to one. Detector signatures unique to slow moving particles are exploited to search for HSCP. The backgrounds to the search are SM particles with detector mismeasurement and in some cases muons coming from cosmic rays.

Five different searches are presented, one requires only that a track be found in the muon system, this is referred to as the *muon only* analysis. This analysis is expected to still have sensitivity when all HSCP are produced electrically neutral. The second requires that the stand alone track be matched to a track in the inner tracker, referred to as the *muon+track* analysis. This analysis is especially powerful for lepton like HSCP. The third is the *track only* analysis that only requires the HSCP be found in the inner tracker so that it can be sensitive to HSCP becoming neutral in the calorimeter and leaving no hits in the muon system. The last two analyses look for particles with $Q \neq 1e$. The *multiple charge* analysis looks high charge HSCP with a reconstruction like the *muon+track* analysis and the *fractional charge* analysis which looks for fractionally charged analysis with a reconstruction signature like the *track only* analysis.

5.3 Samples

Data collected with the CMS detector during 2012 running at an energy of $\sqrt{s} = 8$ TeV are searched. The data collection was split into four periods labeled A, B, C, and D. All data collected by CMS unundergo a prompt reconstruction as described in section **??**. The first two run periods, A and B, underwent an additional rereconstruction so as to have the latest reconstruction improvements and calibration constants. The rereconstructed samples are used for the A and B periods while the promptly reconstructed samples are used for the C and D periods.

CMS has a Data Certification team which checks all data collected and certifies the data as good for analysis. The certification requires all detector subsystems to be operating at full ability, or at least close enough to full ability to not have a detrimental effect on offline analyses. Additionally higher level objects such as muons and electrons are checked to make sure the data are good for physics analyses. For this particular analysis the RPC trigger plays an important role, as discussed in section 5.4, and so the RPC is required to be included in the L1 trigger for all data searched. This leads to this search using slightly less data than most other CMS analyses on 2012 data. The data sample used by this analysis corresponds to $18.8 fb^{-1}$.

Multiple different signal MC samples are produced to account for the multiple different signatures a HSCP could have. Pair production of gluino and stop samples with masses in the range 300–1500 GeV and 100–1000 GeV, respectively, are generated in the split SUSY scenario [9, 10]. The gluino samples are produced with the assumption of a high squark mass of 10 TeV. The samples are generated using PYTHIAv8.153.

Gluinos and stops have color charge and as such will form composite hadrons with SM quarks and gluons after production, referred to as $R - hadrons$. These $R - hadrons$ can be electrically neutral or have charge Q, taken here and everywhere else in this paper unless otherwise stated as the absolute value of the charge, of 1e or 2e. One particularly interesting case is gluino-gluon balls which will be electrically neutral. The fraction of gluinos forming these balls is a free parameter in the theory and samples are used with the fraction, f, set to f=1.0, 0.5, 0.1, a value of 1.0 should be assumed in this paper unless otherwise stated. If f=1.0 then all gluino $R - hadrons$ will be produced electrically neutral.

After the $R - hadrons$ are produced, they will propagate out to and interact with the CMS detector. In the interactions with the CMS detector it is possible for the $R - hadrons$ to undergo charge exchange where the electrical charge of the $R - hadron$ can change, possibly going from neutral to charged or from charged to neutral. The process occurs through an exchange of quarks with the detector material in nuclear interactions [1]. The modelling of these interactions has some uncertainty and two different scenarios are studied, the first is the model presented in [19, 20] which is referred to as the cloud model, the second model results in all $R - hadrons$ becoming neutral after a nuclear interaction as described in **??**. Most HSCP will not have a nuclear interaction while passing through the CMS tracker however a very large majority will have one in the calorimeter system.

The above effects can lead to many interesting signatures in the CMS detector. R-hadrons neutral after hadronization will generally remain neutral through the tracker but may gain charge in the calorimeter under the cloud model and leave hits in the muon system. If the gluino-gluon ball fraction is 1.0 then this would be the only way to detect gluino HSCP, the *muon only* analysis is designed

to have sensitivity to HSCP of this type. On the other hand HSCP produced charged under the charge suppression model will likely be charged in the tracker but always neutral in the muon system. The *track only* analysis is designed to be sensitive to HSCP of this type. HSCP produced neutral under the charge suppression model would never be charged during their passage through CMS and thus are outside the scope of a HSCP search, they would fall into searches for dark matter.

Pair production of stau samples are produced under the minimal gauge mediated symmetry breaking (mGMSB) scenario [11] using the SPS7 slope [12]. The ISASUGRA version 7.69 program is used to set the particle mass scale and decay table. The program fixes a number of mGMSB parameters. The number of messenger particles is set to to three, $tan\beta = 10$ (β used differently than for speed above), $\mu > 0$, $C_{Grav} > 10000$, and $M_{Mes}/\Lambda > 2$. The high value of C_{Grav} results in the stau being long-lived while varying Λ from 31 to 160 TeV gives staus within a mass range of 100–494 GeV. The produced mass spectrum and decay table are passed to PYTHIAv6.426 [13]. Stau production proceeds by either by direct electroweak production or from the cascade decay of other particles (usually through the pair production of gluinos and stops). Cascade decay is dominant due to the strong nature of the production mechanism. In order to give the best results while maintaining model independence two stau samples are used. One using all production mechanisms (GMSB) and one only with staus only produced through direct production (Pair prod.). The second sample is less dependent on the model parameters.

The last of the signal samples used is modified Drell-Yan production of long-lived lepton like fermions. The fermions have arbitrary electric charge and are neutral under SU(3)C and SU(2)L and thus couple only to the photon and Z
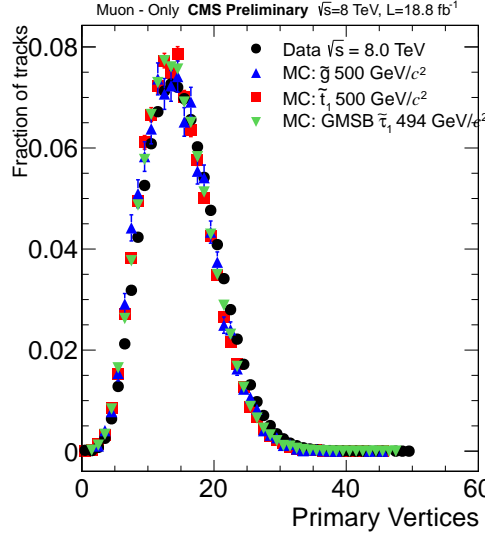
Figure 5.1: Distribution of number of vertices in Data and various MC samples

boson. As all SM particles that reach CMS have electrical charge, Q, equal to $\pm 1e$ or are neutral, the possbility of HSCPs with non-unit charge is interesting. Note for the rest of this paper Q is taken as the absolute value of the electrical charge unless specifically stated otherwise. The particles can generically be divided by whether they have Q¡1e or Q¿=1e. The production of these particles is simulated with PYTHIAv6.426 [13]. Samples are produced with charge Q = 1/3, 2/3, 1, 2, 3, 4, 5, 6, 7, and 8e for masses of 100-500 GeV for Q¡1e, 100-1000 GeV for 1e ¡= Q ¡= 5e, and 200-1000 for Q ¿ 5e. The samples can generically be divided by whether they have Q¡1e or Q¿=1e.

All MC samples are overlaid with simulated minimum bias events, see Section 3.2, to reproduce the pile up observed in data. After this reweighting there is a very good agreement between data and MC as seen in Figure 5.1.

5.4 Trigger

All events used in the search are required to be triggered by one of three algorithms. The algorithms require a track to be found and/or missing transverse energy, PFMET, as calculated by the particle flow algorithm [5].

The particle flow algorithm attempts to reconstruct all particles in an event, then calculates PFMET as the negative vector sum of the transverse momentum of the particles. As the proton-proton collision occurs at rest in the transverse plane, PFMET is meant to represent the vector sum of all particles not found by the particle flow algorithm. For most CMS analyses PFMET is created by either the limited detector response in finding all tracks in an event and determining their momentum or from neutral particles in the event which leave no signals in the detector. These neutral particles could be neutrinos from the standard model or new neutral particles created in a BSM theory such as supersymmetry.

For HSCP the PFMET often arises because of details of the particle flow algorithm. The algorithm assumes SM particles and rejects tracks that do not conform to the properties expected of a SM particle. Two types of possible HSCP tracks are rejected by the algorithm. The first is tracks reconstructed only in the muon system. The only SM particles that are expected to reach the muon system are muons and muons should have a matching track in the inner tracker. HSCP produced neutral then acquiring charge as they propagate through CMS usually would only have a track in the muon system and as such would not be included in the PFMET calculation.

The second is tracks produced charged but becoming neutral as they propagate through CMS. The particle flow algorithm rejects tracks reconstructed only in the inner tracker that have a track p_T much larger than the associated energy

deposited in the calorimeter. As an HSCP only deposits approximately 10GeV of energy in the calorimeter and normally have > 100GeV of momentum HSCP neutral in the muon system will likely be rejected.

These two effects lead to PFMET in HSCP events to be roughly equal to the vector sum of any HSCP neutral in either the muon system or the inner tracker, less however much energy they deposit in the muon system. This effect can be seen in Figures 5.2 and 5.3 which compare the di-HSCP system with online PFMET in events with at least 150 GeV of online PFMET.

One trigger issue unique to slow moving particles is the acceptance of the L1 trigger. If an HSCP arrives in the muon system too late it can trigger the readout of the wrong bunch crossing. As most of the CMS subdetectors, though not the muon system, are designed to not readout data coming from adjacent bunch crossings the data from the correct bunch crossing would be lost. To help deal with this members of the CMS L1 trigger team developed a special configuration of the RPC L1 trigger to partially recover HSCP that arrive in the muon system in the bunch crossing following the crossing they were produced in. The configuration creates a duplicate copy of all RPC hits and sends them to the muon trigger in the bunch crossing immediately preceding the arrival of the hits. This allows for HSCP that arrive in the RPCs $0.5 - 1.5$ bunch crossings later than a collision muon would to still trigger the readout of the correct event. For particles that arrive in the RPC in the correct bunch crossing a coincidence with the LHC beam crossing through the machine is required to prevent the readout of the previous event. This configuration was possible for 2012 running as the proton bunches were separated by 50ns despite having 25ns wide bunch crossing windows.

The first of the three algorithms used requires both a track to be found in the
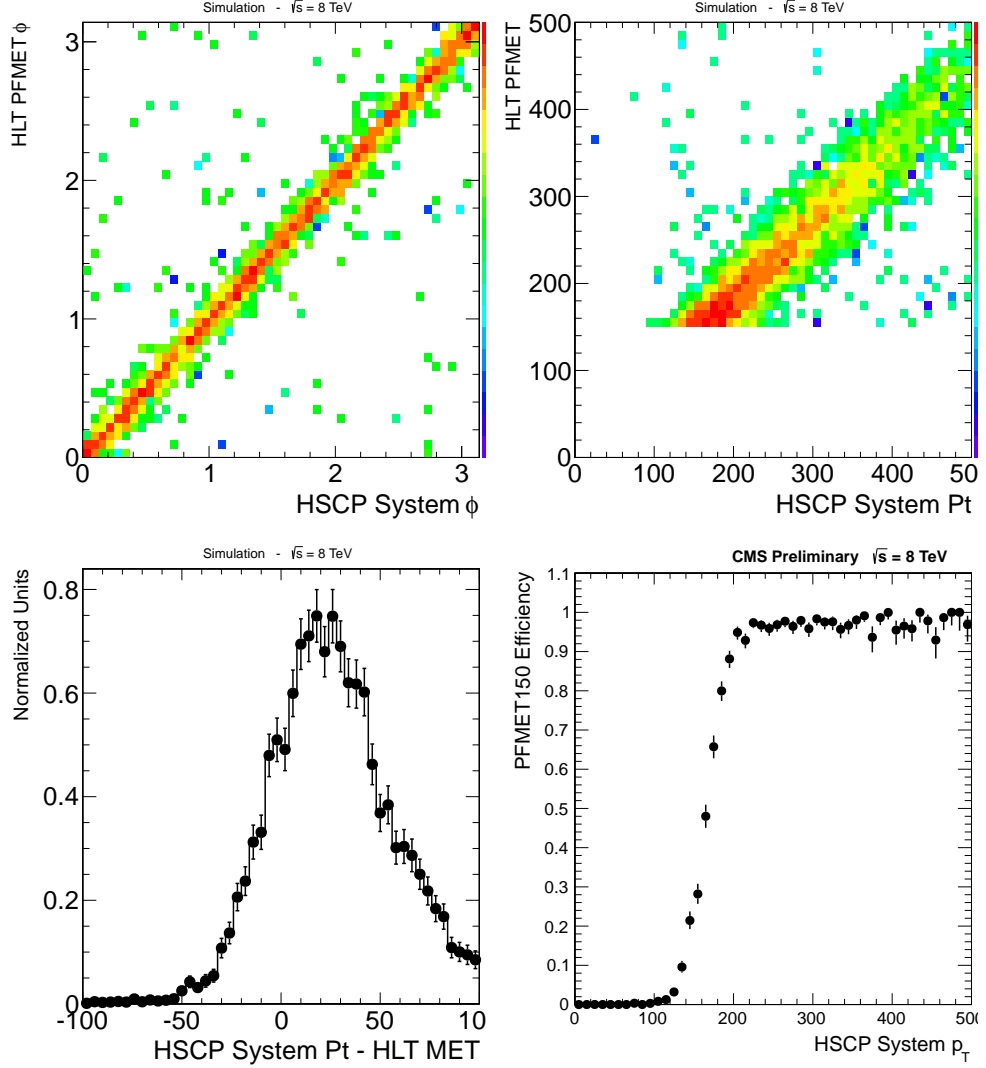
Figure 5.2: Comparison of di-HSCP system with online PFMET for a 1200 GeV Gluino $f = 1.0$ sample in events with at least 150 GeV of online PFMET. Top Left: Online PFMET ϕ versus di-HSCP system ϕ. Top Right: Online PFMET value versus di-HSCP system p_T. Bottom Left: Difference between di-HSCP system p_T and online PFMET value. Bottom Right: Probability to have online PFMET greater than 150 versus di-HSCP system p_T.
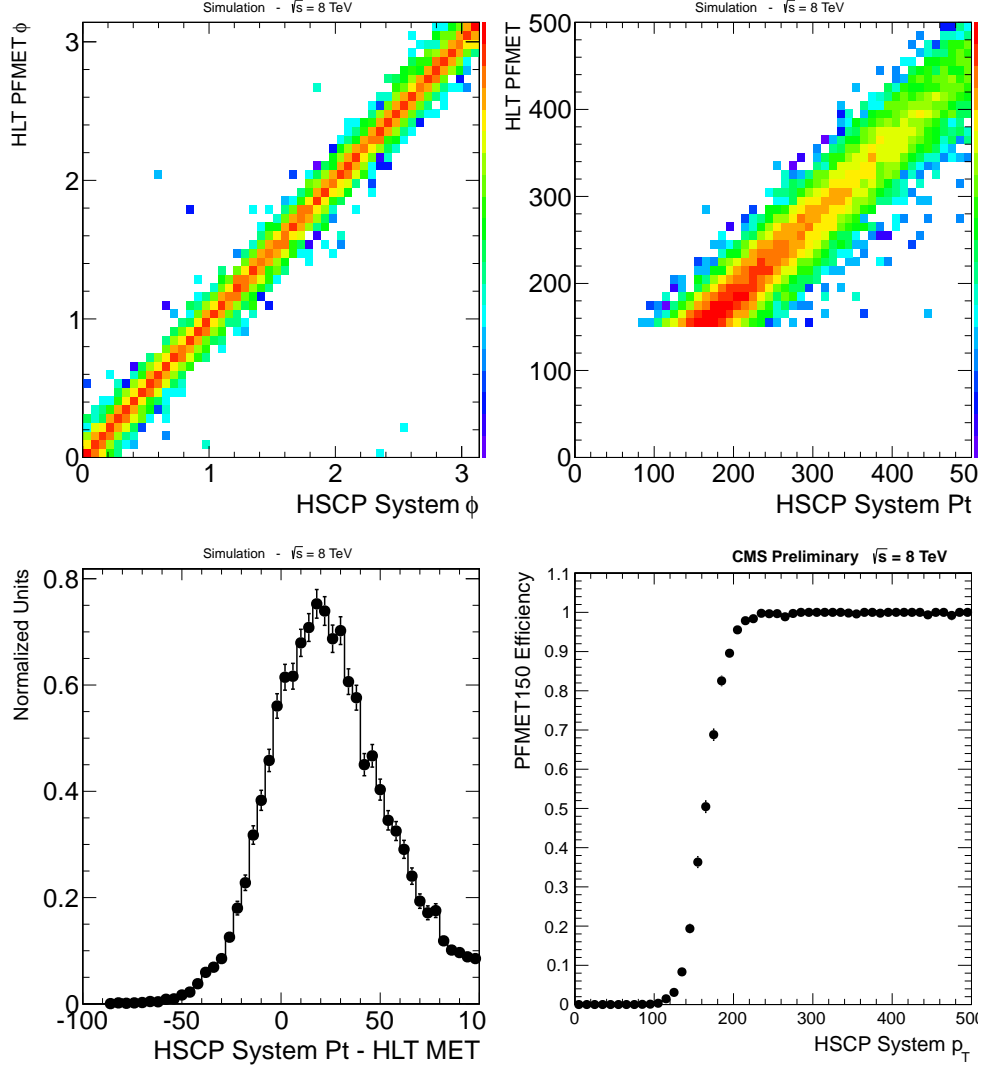
Figure 5.3: Comparison of di-HSCP system with online PFMET for a charge suppressed 1200 GeV Gluino $f = 0.1$ sample in events with at least 150 GeV of online PFMET. Top Left: Online PFMET ϕ versus di-HSCP system ϕ. Top Right: Online PFMET value versus di-HSCP system p_T. Bottom Left: Difference between di-HSCP system p_T and online PFMET value. Bottom Right: Probability to have online PFMET greater than 150 versus di-HSCP system p_T.

muon system with $p_T > 70\text{GeV}$ and $|\eta| < 2.1$ as well as MET $> 55\text{GeV}$. For the first $700pb^{-1}$ of 2012 running the threshold was at 65GeV. The signal samples are weighted to account for the amount data taken at each threshold. Events collected with this trigger are only used in the *muon only* analysis. The second algorithm requires a track matched in both the inner tracker and muon system to be found by the HLT with $p_T > 40\text{GeV}$ and $|\eta| < 2.1$. The only requirement for the third algorithm is PFMET $> 150\text{GeV}$. The second and third algorithms are used in all the analyses.

The decision to use the pure PFMET trigger even though a muon signature is required offline is prompted by the late arrival of the HSCPs in the muon system. Even with the RPC configuration described above very slow moving HSCP can trigger the readout of the wrong event but still be reconstructed offline if the event has been triggered by the pure MET trigger. This can be seen in Figure 5.4 which shows the trigger efficiency versus β with and without the pure MET trigger. Thus using the pure MET trigger allows the search to probe lower β particles.

As color charged R-hadron can be neutral while traversing CMS or arrive so late to the muon system that they are not able to be reconstructed offline an effective detector acceptance is defined that at least one HSCP be reconstructed offline. Thus Figure 5.4 shows the efficiency requiring an HSCP be reconstructed as a a stand alone track, as in the *muon only* analysis, and as a global track, as in the the *muon+track* analysis.

The efficiency for each trigger as well as the combined efficiency is listed for various signals in Tables 5.1 and 5.2 in events with at least one HSCP reconstructed as a stand alone track and global track respectively.

Muons from cosmic rays are an important background for the *muon only*
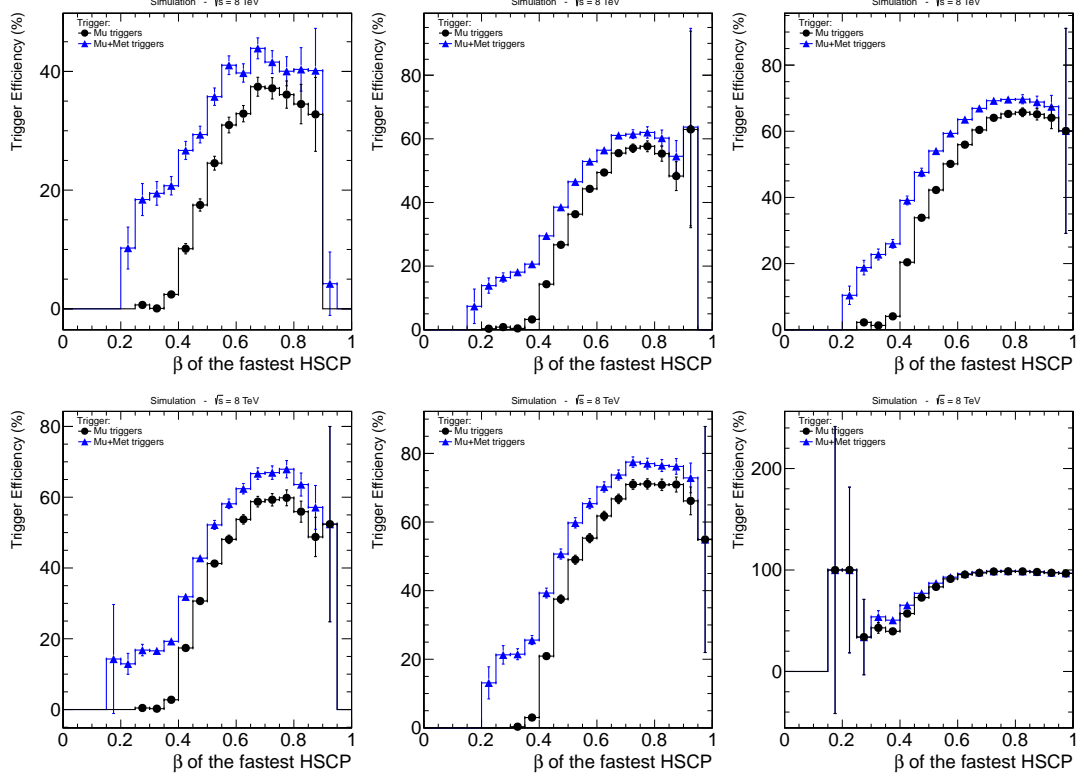
Figure 5.4: Trigger efficiency as a function of the β of the fastest HSCP reconstructed in the event. Top Row: Requiring reconstructed track be stand alone for 1200 GeV Gluino $f = 1.0$ (left), 1200 GeV Gluino $f = 0.1$ (middle), and 800 GeV Stop (right) samples. Bottom Row: Requiring reconstructed track be global for 1200 GeV Gluino $f = 0.1$ (left), 800 GeV Stop (middle), and 494 GeV GMSB Stau (right) samples.

Table 5.1: Trigger efficiency for various models considered using the SingleMu, PFMET, L2Mu+MET or a combination of the three.

Model	Mass	Mu40	PFMET150	L2Mu+MET	Total
Gluino $f = 0.1$	400	35.55	19.41	34.28	58.56
Gluino $f = 0.1$	800	31.63	22.57	31.21	54.88
Gluino $f = 0.1$	1200	26.62	20.45	24.63	47.52
Gluino $f = 1.0$	400	5.55	23.22	36.63	46.07
Gluino $f = 1.0$	800	5.01	24.50	31.88	43.41
Gluino $f = 1.0$	1200	3.69	20.62	23.62	35.45
Stop	200	42.79	11.15	27.31	58.80
Stop	500	42.07	19.79	31.13	61.21
Stop	800	41.57	21.57	30.33	60.73

analysis. To study and predict them a trigger that selects events when no beams are passing through CMS is used. The trigger requires the presence of a stand alone track with $p_T > 20\text{GeV}$, no coincidence with the LHC beams and for the event not to be flagged as beam halo. The stand alone track reconstruction used for the cosmic trigger is slightly different than for the collision trigger as it is not updated at vertex, the meaning of this is discussed in section 5.6. However offline both reconstructions are required so no bias is introduced.

5.5   Selection Variables

The low velocity of the HSCP leads to two interesting detector signatures. The first is that the particles will arrive at the detector elements later than SM particles would. The muon system, being the furthest detector element from the

Table 5.2: Trigger efficiency for various models considered using the SingleMu, PFMET, or a combination of the two.

Model	Mass	Mu40	PFMET150	Total
Gluino $f = 0.1$	400	51.87	16.06	59.09
Gluino $f = 0.1$	800	46.50	20.50	56.42
Gluino $f = 0.1$	1200	38.96	19.56	49.95
Gluino $f = 1.0$	400	41.81	19.36	51.76
Gluino $f = 1.0$	800	37.83	21.57	49.01
Gluino $f = 1.0$	1200	31.70	21.16	45.21
Stop	200	58.43	7.69	61.54
Stop	500	56.91	17.40	64.44
Stop	800	56.15	20.49	65.59
GMSB Stau	100	97.86	14.74	98.06
GMSB Stau	308	97.03	17.53	97.47
GMSB Stau	494	95.56	17.76	96.35
PP Stau	100	95.06	0.17	95.09
PP Stau	200	95.78	0.37	95.82
PP Stau	494	95.23	1.16	95.36

interaction point, has the largest timing difference. The measurement of the arrival time of particles in the muon system is discussed in section 4.

The second signature is that a slow moving HSCP will have a larger ionization energy loss in the silicon tracker than SM particles will. The dependence of the ionization energy lost on velocity is described by the Bethe-Bloch formula [2]. SM particles with momentum 10-1000 GeV all deposit roughly the same amount of energy per unit length, dE/dx, ($\approx$ 3MeV/cm) and are often referred to as minimum ionizing particles (MIPs). For particles with $0.1 < \beta < 1$ dE/dx varies as $\sim 1/\beta^2$. As in [4] three variables related to dE/dx are calculated for each track. The first is I_h which is an estimator of the dE/dx of the track. The second is I_{as} which is a discrimant that checks the probability that a MIP would produce a charge less than or equal to the charge of each of the hits along the track. The discrimant peaks at zero for MIPs and approaches one for high-ionizing particles. The last is I'_{as} which has the same form as I_{as} except the probability is that a MIP would produce a charge more than or equal to the charge of the hits, this variable is only used in the fractionally charged analysis.

An estimate of the mass, assuming Q=1e, of a particle can be made from I_h and the momentum of a track. This is done by using Eq. 5.1, also from Ref. [3],

$$I_h = K \frac{m^2}{p^2} + C.$$ (5.1)

with $K = 2.559 \pm 0.001$ MeV cm^{-1} c^2 and $C = 2.772 \pm 0.001$ MeV cm^{-1}.

As HSCP would be created by BSM theories at high energies they are likely to have high momentum. For this reason the p_T of the track is used as a third selection variable.

The *muon+track* measurement uses the p_T measurement coming from the

inner tracker while the *muon only* analysis uses the measurement from the muon system. The HSCP is likely to stay the same charge while passing through the inner tracker so the *muon+track* is relatively unaffected by this. However for the p_T measurement from the muon system it can result in the p_T of the HSCP to be overestimated.

CMS measures the curvature of a track which is function of the q/p_T of the track. A charge of $|q| = 1e$ is assumed in order to determine the p_T of the track. For HSCP that can modify their charge inside of CMS it can be the case that the average value of q during its passage through the muon system does not equal one. This effect has different consequences for the stop and gluino samples. A stop particle, specifically not an anti-stop, has a charge of $+(2/3)e$ and forms a R-hadron with either an anti-quark ($\tilde{t}\bar{q}$) or two quarks ($\tilde{t}qq$). Anti-quarks have a charge of $-(2/3)e$ or $+(1/3)e$ leading to R-hadrons with a charge of either 0 or $+1e$. Quarks have a charge of either $+(2/3)e$ or $-(1/3)e$ which allows for the creation of R-hadrons with a charge of 0, $+1e$, or $+2e$. Thus a stop R-hadron will always have a positive charge or be neutral. For an anti-stop, the effect is reversed and the R-hadron will always have a negative charge or be neutral.

For gluino particles this statement does not hold true. Gluinos can hadronize in gluon balls ($\tilde{g}g$), R-mesons ($\tilde{g}q\bar{q}$), or R-baryons ($\tilde{g}qqq$ or $\tilde{g}\bar{q}\bar{q}\bar{q}$), with either quarks or anti-quarks allowing the charge of the R-hadron to range from $-2e$ to $+2e$. This leads to the average charge of the R-hadron as it traverses the muon system to be less than $1e$ and the p_T value to be overestimated.

To observe this effect the function $\Delta(q/p_T)$ is defined in Equation 5.2

$$\Delta(q/p_T) = ((q/p_T)_{SA} - (q/p_T)_{Inner})/(q/p_T)_{Inner} \tag{5.2}$$

where SA refers to stand alone track qualities and Inner refers to inner track
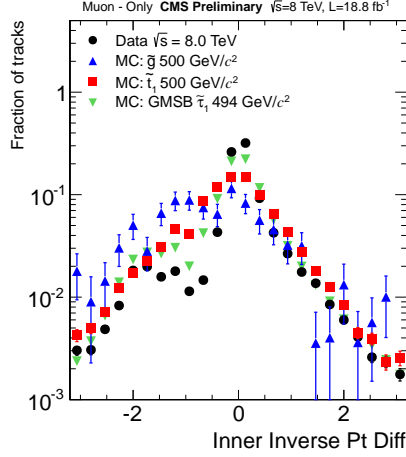
Figure 5.5: Distribution of $\Delta(q/p_T)$ for data, 500 GeV gluino, 500 GeV stop, and 494 GeV GMSB stau.

qualities. Figure 5.5 shows the distribution of $\Delta(q/p_T)$ for tracks with inner track $p_T > 200$ GeV for data and various HSCP signal samples. A value of zero in this plot indicates the p_T was reconstructed correctly while negative one indicates the reconstructed p_T approaches infinity. The GMSB stau sample, which does not change charge, has a distribution similar to data, though slightly wider. The stop sample, which are not able to flip charge but merely to switch between one sign and zero, is centered at zero but with a slightly wider width than data or GMSB stau. The gluino samples, which can flip charge, are centered at negative one meaning that their reconstructed p_T is normally larger than what is generated, sometimes to a very large degree. This effect causes further discrimination of gluino HSCP from background Standard Model particles.

For the lepton like samples with non-unit charge the p_T will be mismeasured by a factor of $1/Q$, meaning fractionally charged particles will have their p_T overestimated while multiply charged particles will be underestimated. This effect can be seen in Figure 5.6.
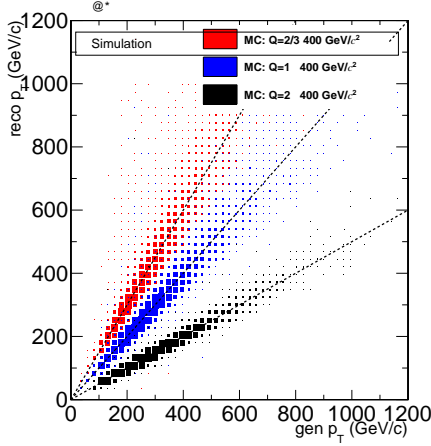
Figure 5.6: Distribution of reconstructed p_T versus generator p_T for Q=2e/3, 1e, and 2e samples.

5.6   Preselection

Candidates for the *muon only* analysis are tracks reconstructed in the muon system. Candidates for the *muon+track* and *multiple charge* analysis are tracks found in both the muon system and the inner tracker. The *track only* and fract analyses require only that the tracks be found in the inner tracker. Various requirements are applied to the candidate in order to reduce tracks from background process while maintaining good efficiency for HSCP.

The *muon only* analysis requires the candidates to have $p_T > 80$, $|\eta| < 2.1$, and valid DT or CSC hits in at least two muon stations to reinforce the requirements applied at trigger level. Quality cuts on the β^{-1} measurement are applied. The measurement must have at least eight degrees of freedom and the error must be less than 0.07. A potential background source is muons coming from out of time bunch crossings. Candidates are required to have a measured time leaving the vertex not be within 5ns of an out of time bunch crossing. Figure 5.7 shows

the distribution of these quantities for data, cosmic control sample, and signal MC. Additional cuts are used to control the background from cosmic rays. The displacement of the track with respect to the beam spot is required to be less than 15cm in both the longitudinal and transverse direction relative to the beam line. The candidate $|\phi|$ must not be within 1.2–1.9, this region represents tracks pointing in the vertical direction, as is expected of cosmic rays. Cosmic rays travel through the top and bottom halves of the detector leaving hits in the muon system opposite of the candidate. It is required that there be no muon segments with η within 0.1 of $-\eta_{candidate}$. Only segments separated from the candidate by at least 0.5 in ϕ are used to prevent candidates in the central portion of the detector to match to their own segments. Figure 5.8 shows the distribution of these quantities.

The *muon+track* analysis applies cuts on the inner tracker track which has a much better p_T and impact parameter resolution than the muon system track. The candidate is required to have $p_T > 45$ and $|\eta| < 2.1$ to match the trigger level requirements. Quality cuts are applied as low quality background tracks can have mismeasured moment and potentially high fluctuations in dE/dx. The inner track is required to have at least eight hits in the inner tracker with at least two coming from the pixel detector. At least 80% of the hits associated with the track must be considered valid. A cleaning procedure is applied to the hits before calculating dE/dx and there must be at least six measurements passing this cleaning. Figure 5.9 shows these variables for data and signal MC.

The relative error on the candidate p_T (σ_{p_T}/p_T) must be less than 0.25 and the χ^2 per degree of freedom must be less than five. While cosmics are expected to be a negligible background in the *muon+track* analysis loose cuts are placed on the impact parameter of the track, these cuts are nearly 100% efficient for signal
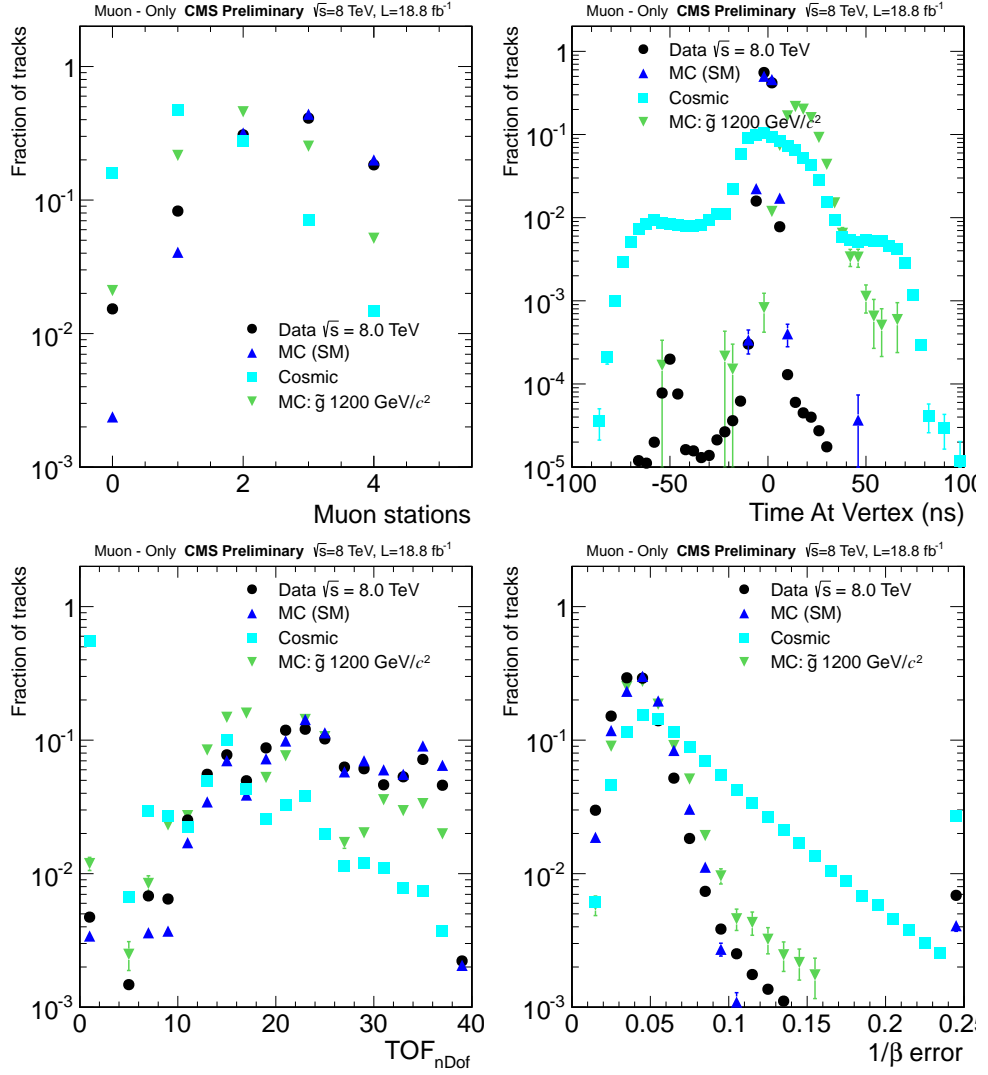
Figure 5.7: Distribution of various prelection variables for data, cosmic control sample, and signal MC. Top row: Disitribution of number of matched stations (left) and time at vertex (right). Bottom row:Number of degrees of freedom (left) and error (right) on β^{-1} measurement.
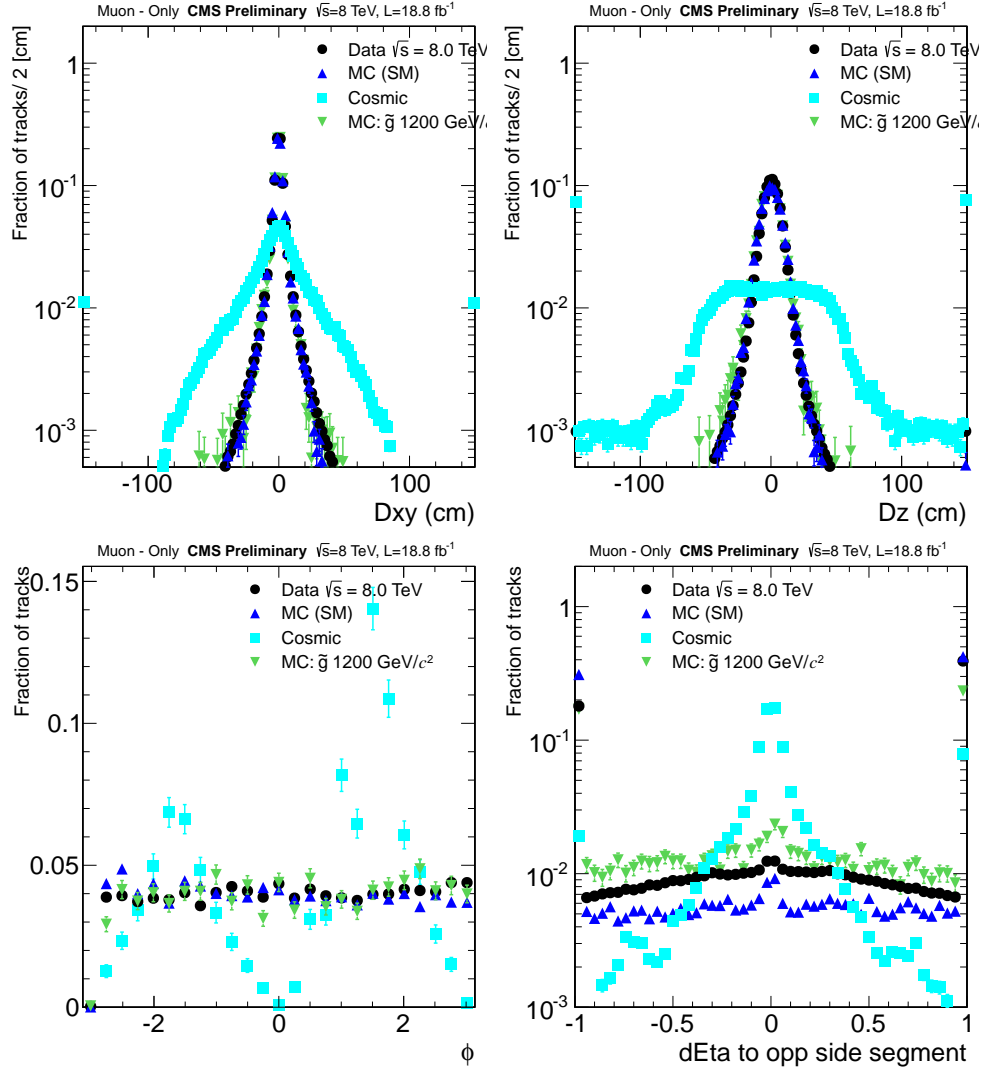
Figure 5.8: Distribution of various prelection variables for data, cosmic control sample, and signal MC. Top row: Disitribution of transverse (left) and longitudinal displacement (right). Bottom row: Distribution of ϕ (left) and η separation to muon segments (right).
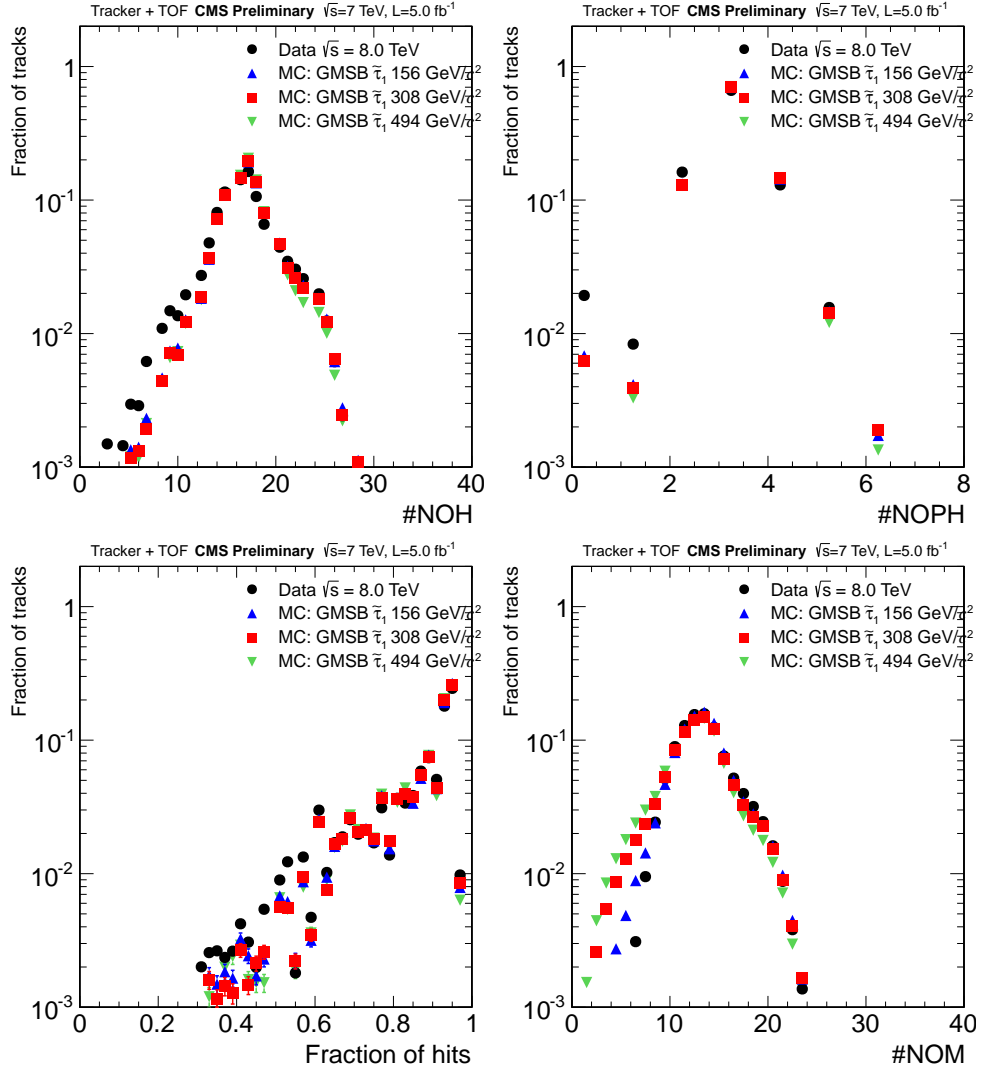
Figure 5.9: Distribution of various prelection variables for data and signal MC. Top row: Number of tracker (left) and pixel (right) hits. Bottom row: Fraction of valid tracker hits (left) and number of measurements used for dE/dx calculation (right).

particles. The displacement of the track with respect to the primary vertex with the smallest longitudinal displament must be less than 0.5 in both the transverse and longitudinal directions. Figure 5.10 shows p_T error, χ^2 per degree of freedom, and the d_z and d_{xy} displacement for data and signal MC.

The candidates for the *muon+track* analysis are also required to be isolated to reduce QCD production of jets where overlapping tracks could give anomolously high dE/dx values. The isolation cuts are kept very loose as slow moving HSCP will deposit more energy in the calorimeter than a SM particle. The sum of the momentum of the tracks within 0.3 of the candidate (excluding the candidate itself) is required to be less than 50 GeV. Additionally the total amount of energy measured in the calorimeter within a radius of 0.3 to the candidate divided by the candidate momentum must be less than 0.3.

Additionally, the *muon+track* analysis uses the same cuts on the β^{-1} error and number of measurements as the *muon only* analysis. Figure 5.12 shows the isolation and β^{-1} variables for data and signal MC.

The *track only* analysis applies the same preselection as the *muon+track* analysis except the cuts on the timing measurement are not applied as the candidates are not required to be reconstructed in the muon system. The *fractional charge* analysis uses preselection like *track only* but inverting the I_h requirement to be less than 2.8 and requiring no tracks with p_T greater than 45 GeV to have an opening angle with the candidate greater than 2.8 radians.

The *multiple charge* analysis applies the same selection criteria as the *muon+track* analysis except the cut relative isolation less than 0.3 and the cleaning of the hits used for the dE/dx calculation is not done. The cleaning procedure is not applied because the amount of charge deposited is proportionalt Q^2 meaning that even a $Q = 2e$ HSCP will deposit four times as much charge as a $Q = 1e$ HSCP. As the
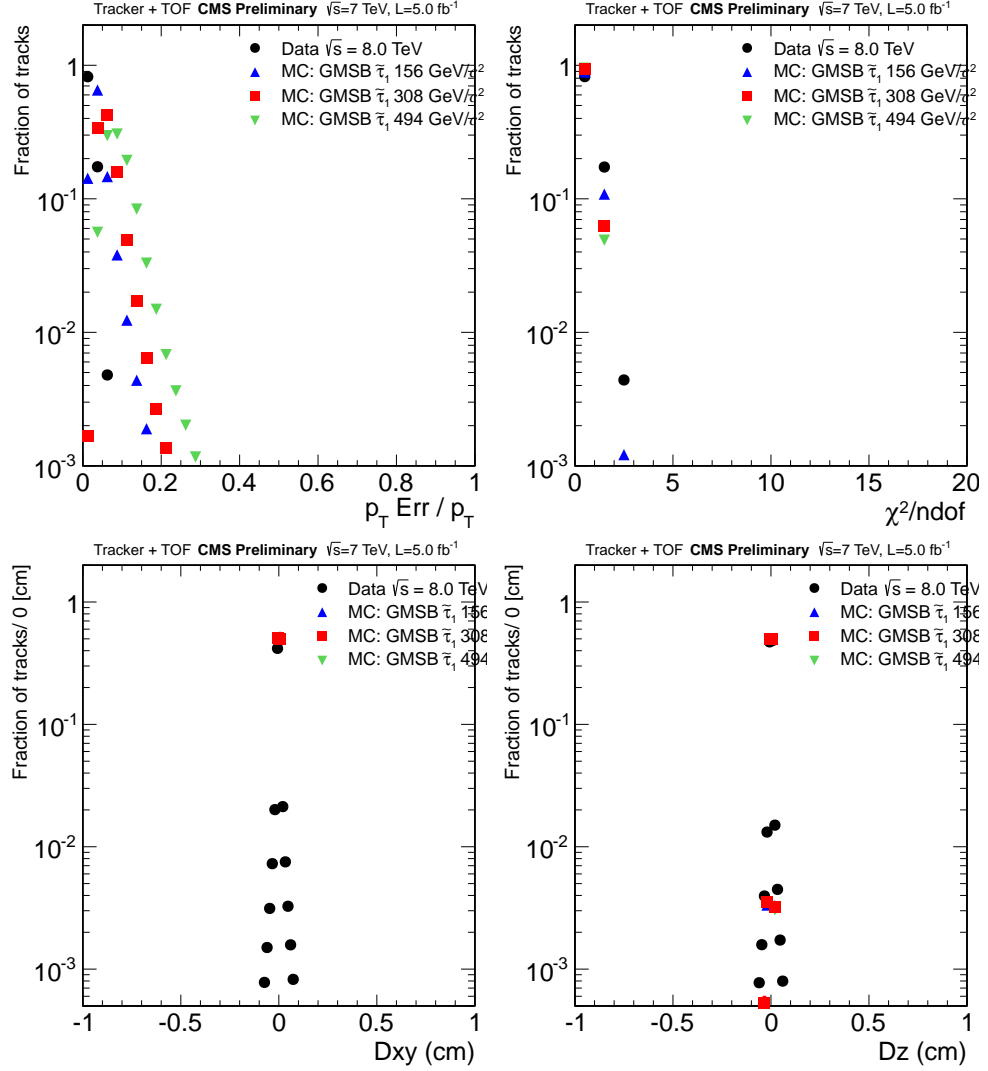
Figure 5.10: Distribution of various prelection variables for data and signal MC. Top row: Relative p_T error (left) and χ^2 per degree of freedom (right). Bottom row: Displacement in the transverse (left) and longitudinal (right) directions.
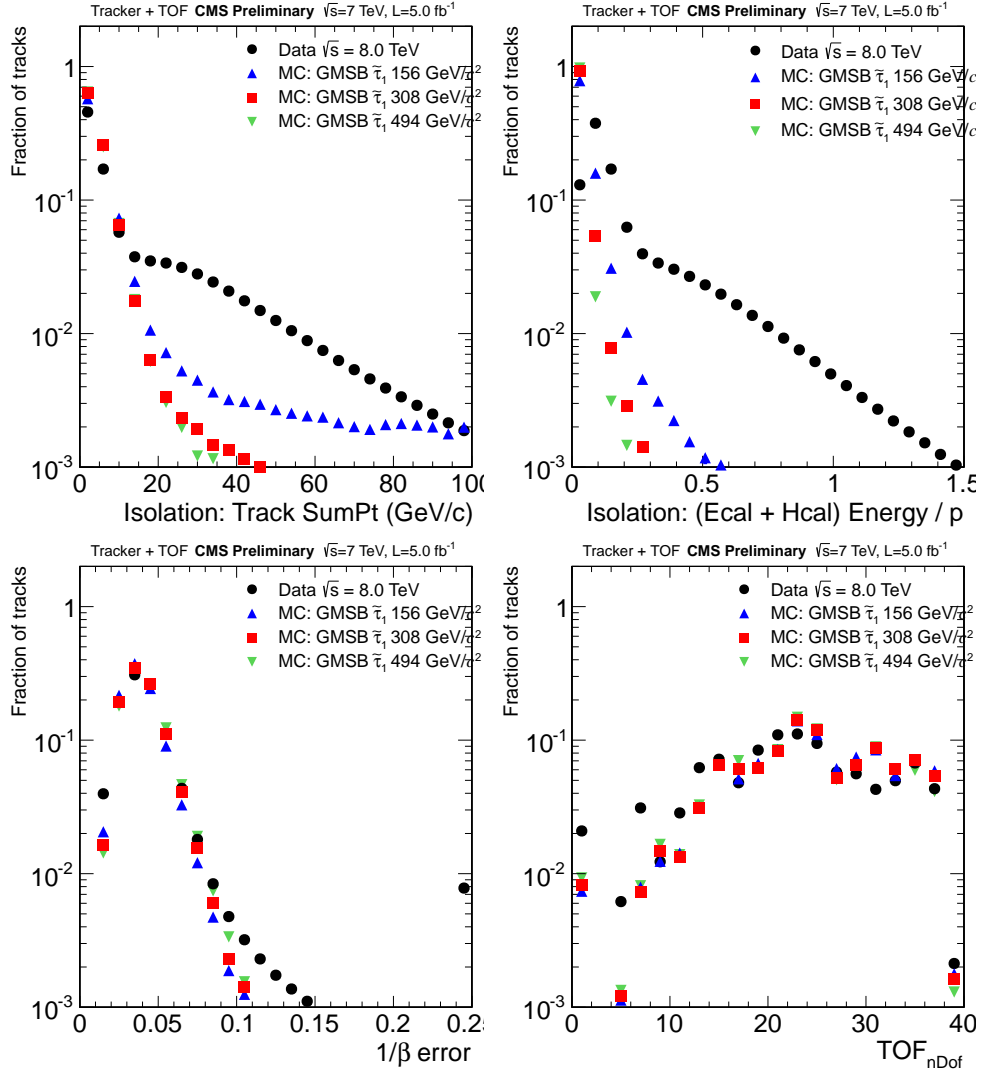
Figure 5.11: Distribution of various prelection variables for data and signal MC. Top row: Sum momentum of tracks within 0.3 (left) and calorimeter energy within 0.3 divided by track momentum. Bottom row: Distribution of the β^{-1} measurement error (left) and the number of degrees of freedom (right).
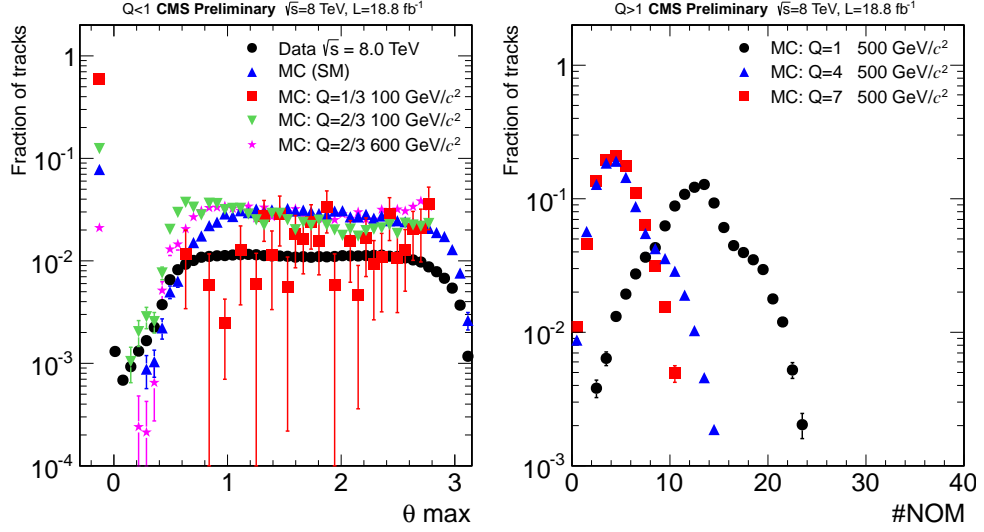
Figure 5.12: Distribution of number of measurements passing cleaning for samples of three different charges

tracker saturates for a charge 3 times that expected for a MIP many of the hits from $Q > 1e$ HSCP will be saturated and this can confuse the cleaning procedure. Additionally, as the high charge samples deposit so much charge containing the tails of the dE/dx distribution is not as important. Figure 5.12 shows the number of measurements passing the cleaning for multiply charged samples and the opening angle described above for fractionally charged samples.

The total preselection efficiency is shown in Table 5.4. The efficiencies are presented with respect to HSCP reconstructed as a track in CMS. The efficiencies decrease at high mass for color charged HSCP as the HSCP track does not behave like SM particles the reconstruction assumes it to be so many of its track qualities become low quality. The cuts are set trying to take this into account but also not allowing poorly reconstructed background tracks to enter into the signal region.

The distributions of p_T and β^{-1} for the *muon only* analysis for data, cosmic control sample, various signal models is shown in Figure 5.13 after applying the

Table 5.3: Preselection efficiency for a few benchmark samples in each analysis. This efficiency is with respect to the reconstructed HSCP candidate (i.e. Stand alone muon for the *track only* analysis and global muon for the *muon+track* analysis).

Model	muon only	track +muon	track only	*fractional charge*	*multiple charge*
Gluino 500 GeV (1.0)	44%	-	-	-	-
Guino 1000 GeV (1.0)	40%	-	-	-	-
Gluino 500 GeV (0.1)	44%	-	70%	-	-
Gluino 1000 GeV (0.1)	43%	42%	51%	-	-
Gluino(CS) 500 GeV (0.1)	-	-	64%	-	-
Gluino(CS) 1000 GeV(0.1)	-	-	47%	-	-
Stop 600 GeV	48%	53%	61%	-	-
Stop (CS) 600 GeV	56%	-	56%	-	-
GMSB Stau 370 GeV	-	76%	78%	-	-

Table 5.4: Preselection efficiency for a few benchmark samples in each analysis. This efficiency is with respect to the reconstructed HSCP candidate (i.e. Stand alone muon for the *track only* analysis and global muon for the *muon+track* analysis).

Model	muon only	track +muon	track only	*fractional charge*	*multiple charge*
DY Q1o3 400 GeV	-	-	-	30%	-
DY Q2o3 400 GeV	-	15%	17%	49%	-
DY Q1 600 GeV	-	72%	76%	-	75%
DY Q3 600 GeV	-	27%	-	-	71%
DY Q5 600 GeV	-	2%	-	-	50%
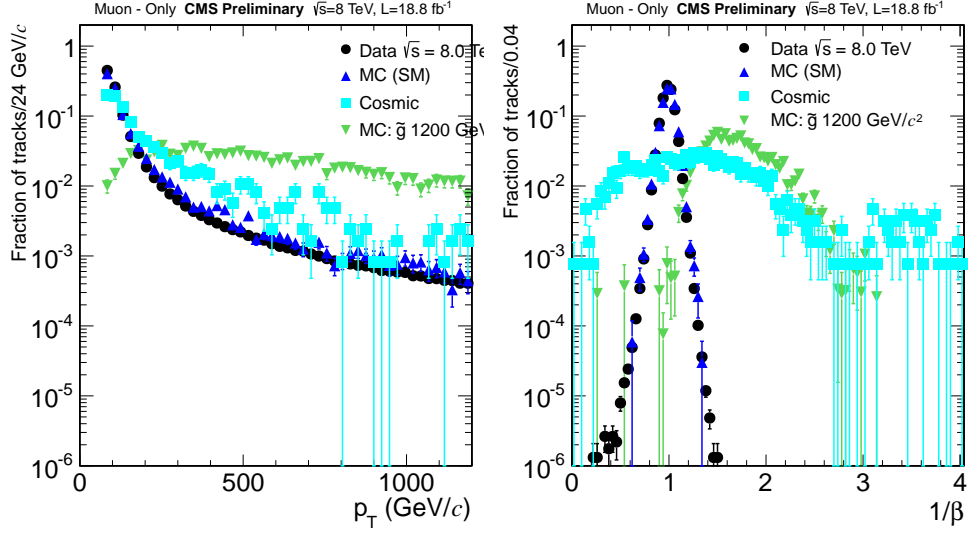
Figure 5.13: Distribution of selection variables for data, cosmic control sample, and signal MC. Left: Distribution of p_T. Right: Distribution of β^{-1}.

preselection requirements. Figure 5.14 shows the p_T, β^{-1}, and dE/dx distributions after applying the *muon+track* preselection cuts for data and various signal models.

5.6.1 Tag and Probe Studies

The study of the agreement between data and MC for numerous muon qualities is done by the Muon Physics Object Group (POG) inside of CMS. For all of the analyses except for *muon only* it is sufficient to use results obtained from this group for possible scale factors between data and MC and relevant systematic uncertainties as the variables it selects on are used frequently within CMS. However, as the *muon only* analysis uses numerous variables which are unique to the analysis so the values from the muon POG are not applicable.

For this reason additional studies were performed to test the agreement of MC with data. The efficiency of the selections was checked with a tag and probe
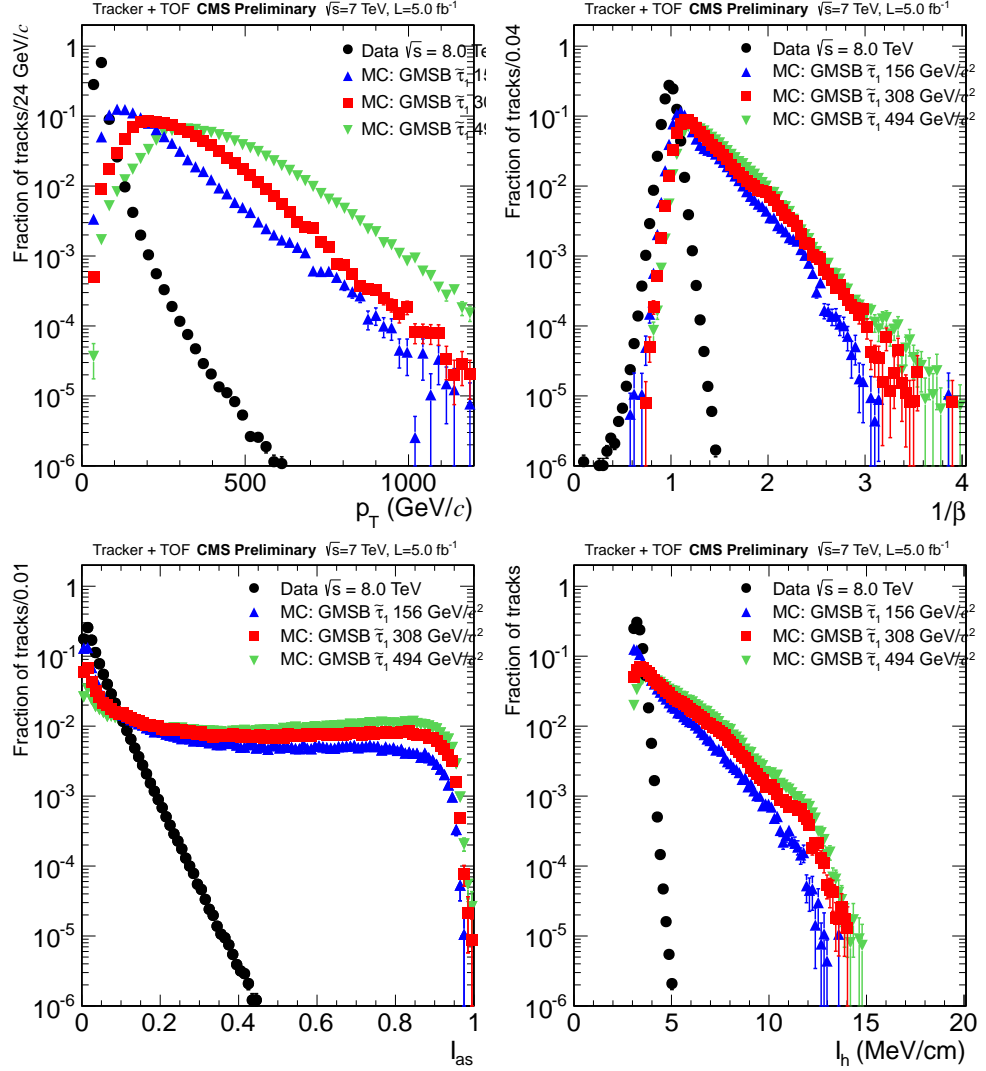
Figure 5.14: Distribution of section variables for data and signal MC. Top row: Distribution of p_T (left) and β^{-1} (right). Bottom row: Distribution of I_{as} (left) and I_h (right).

procedure (from the Muon POG) using muons from the decay of the Z boson. Z bosons decay to a particle and its anti-particle with the invariant mass of the particle–anti-particle pair equal to the mass of the Z boson they were created from, for the purpose of this study the particles are taken as muons.

The tag and probe procedure proceeds by requiring one muon, the tag muon, be found with a very stringent selection trying to assure that this is a good muon. The tag muon is required to pass a tight selection recommended by the Muon POG and to match to an object that triggered the readout of CMS. The last requirement assures that no bias is introduced by the need for the event to readout. Additionally the tag must pass the requirements of a skim that was used to reduce the data size to a level making processing reasonable. The skim requirements were at least three dE/dx measurements and $I_h > 3.0$ or $I_h < 2.8$.

Then a set of probe candidates are defined as tracks reconstructed in the inner tracker with no requirement on muon system activity. The probes are required to have $p_T > 40 GeV$, $|\eta| < 2.1$, and the opposite charge of the tag muon. The invariant mass of the tag and probe is then required to be within 10 GeV of the mass of the Z boson, 91 GeV.

There are a few processes other than Z boson decay that will lead to tag probe pairs having an invariant mass around the mass of the Z boson. Thus it is likely that the probe is a muon. This allows to find the efficiency that a muon will pass the preselection in the *muon only* analysis by looking at the efficiency that the probe passes the preselection. The efficiencies in data and MC can be compared and any discrepancies accounted for. The residual background from non Z boson decay in the mass window is accounted for by a fit described below. The MC sample used only contains the creation of Z bosons, background processes are not included.
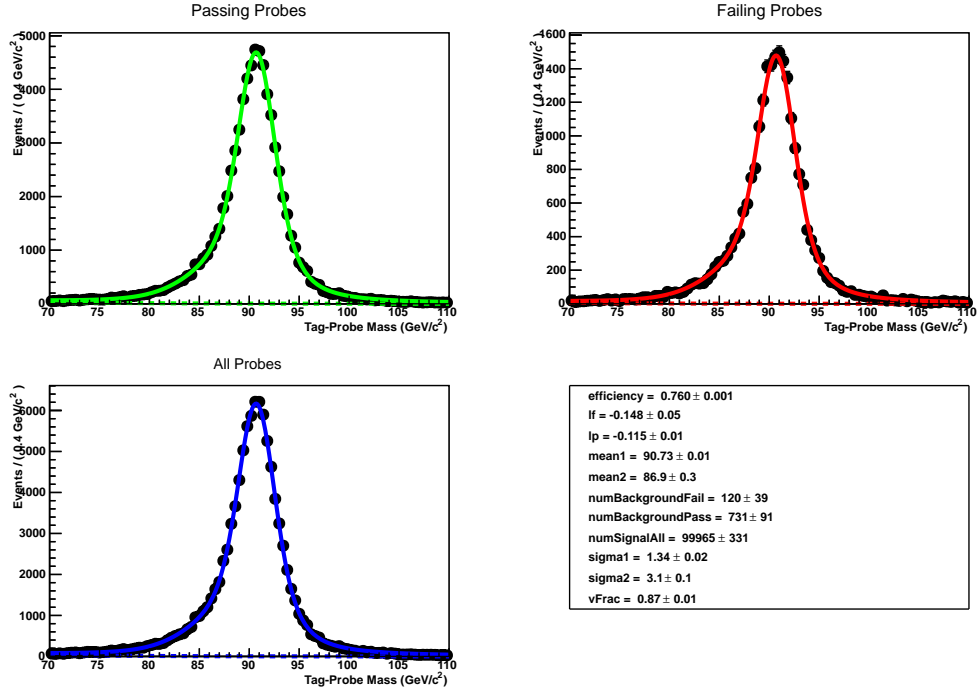
Figure 5.15: Example fit canvas of fit to invariant mass distribution for the muon efficiency tag and probe measurement for the *muon only* analysis for data.

A simultaneous fit to pairs originating from Z bosons and pairs from background is performed using the sum of two Voigtians to represent Z bosons and an exponential for the background. Figure 5.16 shows sample fits of both Data and MC. It can be seen that the fit matches well. The efficiency is extracted from these fits using a procedure from the muon POG.

Figure 5.17 shows the efficiency for the probes to pass the preselection, except for the selection on p_T, against the probe p_T, η, and the number of vertices in the event. Overall the efficiency is approximately 75% in data and 80% in MC. The efficiency is mostly flat versus p_T and number of vertices but does depend on η. MC is scaled by an η dependent amount to correct for the discrepancy.
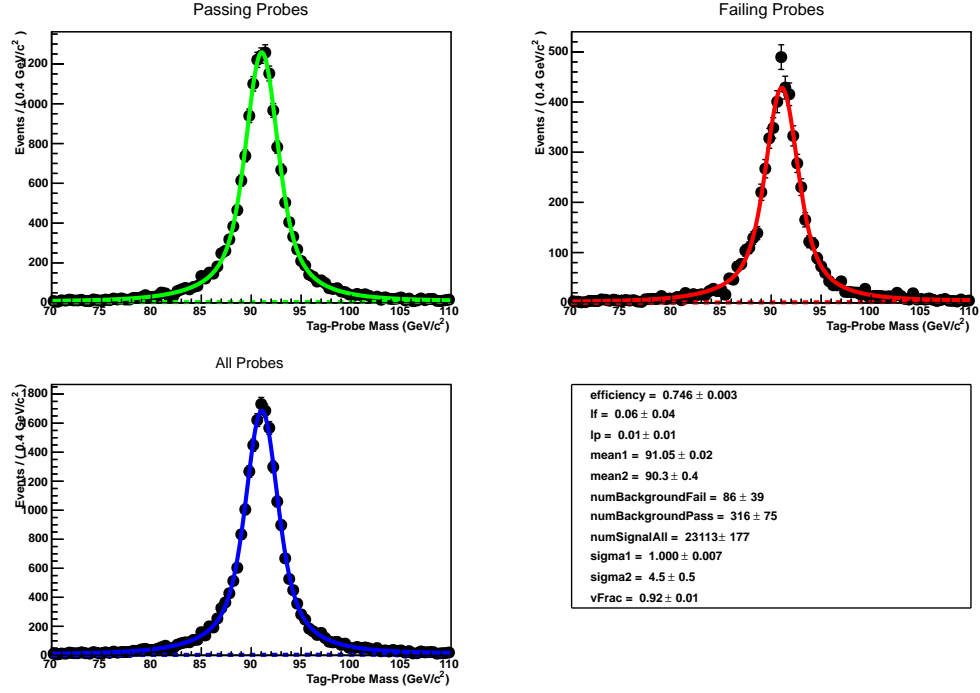
Figure 5.16: Example fit canvas of fit to invariant mass distribution for the muon efficiency tag and probe measurement for the *muon only* analysis for MC.
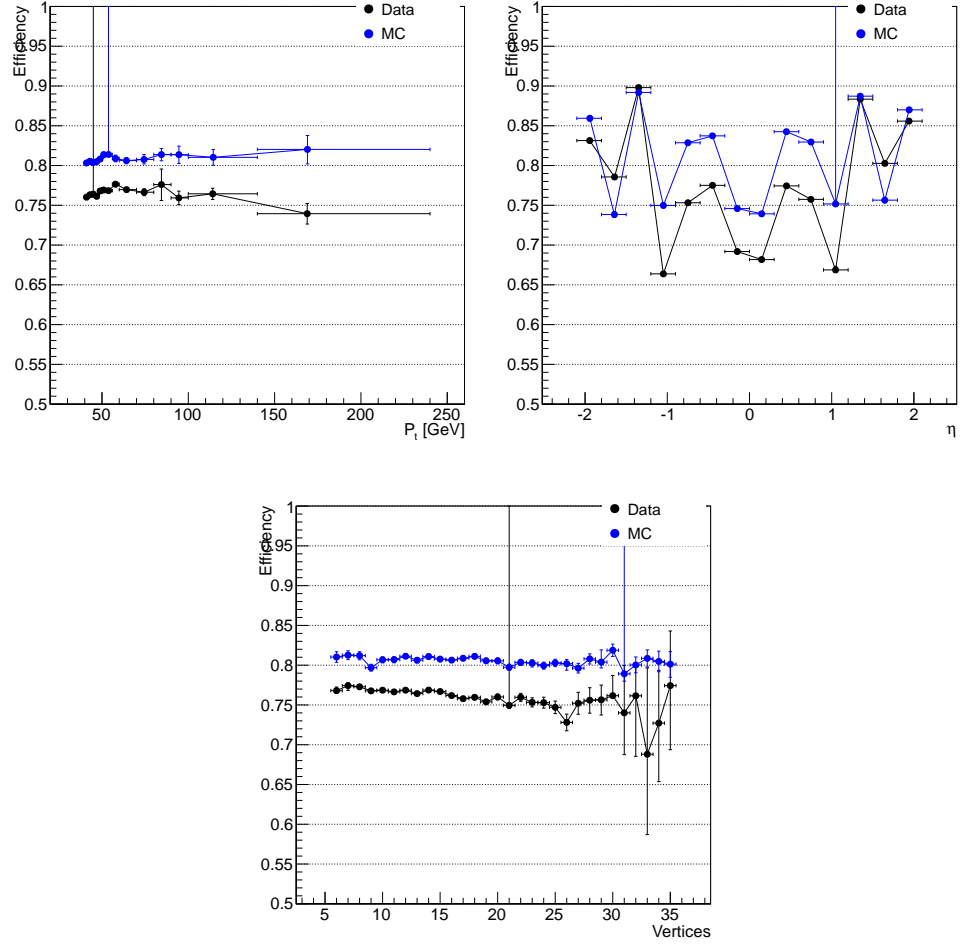
Figure 5.17: Efficiency to pass preselection cuts for the *muon only* analysis for p_T (left), η (center), and number of primary vertices (right).

5.7 Background Prediction

All of the analyses perform a counting experiment on the number of events with a track passing threshold values on some grouping of the p_T, β^{-1}, and dE/dx variables. The *muon+track* and *track only* analysis also place a cut on the mass of the candidate as described below. There are two sources of background considered in the analyses.

The first is muons from the collisions in the LHC. While these muons will all be travelling at very nearly the speed of light and thus arriving at the muon system at approximately the same time, detector resolution effects result in a smearing of the measured speed of the particle. Additionally, collision muons can have large reconstructed momentum either due to true high momentum or detector mismeasurement resulting in a promotion of a low momentum muon to a high reconstructed momentum. While muons in the momentum region of interest all deposit approximately the same amount of energy in the tracker on average, the amount deposited in each interaction is subject to large variations. This can lead to background tracks with a high or low dE/dx value. Detector resolution can also contribute to tracks with high or low dE/dx. Collision muons are predicted exploiting the lack of correlation between the selection variables.

The second source of background, important only for the *muon only* and *fractional charge* analyses, is muons from cosmic rays. As discussed in Section 2.2.1 muons from cosmic rays (referred to as cosmics) are constantly passing through CMS. Cosmics will arrive to the muon system asynchronously with collisions from the LHC. Depending on exactly when the cosmic arrives in the muon system relative to collisions from the LHC this can give rise to a particle with a large β^{-1} measurement. Out of time particles are not centered in the tracker's charge collection window giving them lower dE/dx.. This combined with the impact

parameter cuts applied at preselection makes cosmics negligible for the analyses looking for high dE/dx in the tracker. The distribution of p_T for cosmics falls off at high momentum slower than for collision muons, as evidenced in Figure 5.13 (left). As cosmics have different p_T, β^{-1}, and dE/dx distributions than collision muons they will not be accurately predicted with the same method used to predict the collision muon background. Dedicated methods using the cosmic control sample and impact parameter sidebands are described below.

For all the analyses the systematic uncertainty on the expected background in the signal region is estimated from the spread of various background estimations.

The following variables are defined:

$$V_N^{syst+stat} = \sqrt{\sum_i \left(x_i - <x>\right)^2 / (N-1)}$$

$$V_N^{stat} = \sqrt{\sum_i \left(\sigma_i\right)^2 / N} \tag{5.3}$$

$$V^{syst} = \sqrt{V_{syst+stat}^2 - V_{stat}^2}$$

where N is the number of estimates considered, the sum is over N, x_i is the value of the ith background estimate, and σ_i is the statistical uncertainty on the ith background estimate. The first quantity is an estimator of the variance of the background estimates, which takes both statistical and systematic contributions. The second quantity is adopted as an estimator of the contribution of the statistical uncertainties to the variance. Finally, the contribution of the systematic uncertainty to the background estimates is taken assuming that the latter adds in quadrature to the statistical uncertainty and is therefore obtained from the last expression.

5.7.1 Prediction for *muon only* analysis

The collision muon background is predicted by exploiting the lack of correlation between the selection variables for background particles. The *muon only* analysis uses the selection criteria of p_T and β^{-1}. Candidates are divided into four groups based on whether they have p_T and β^{-1} values greater than the thresholds placed on these selection criteria. The four groups are referred to as A,B,C, and D. The A group contains candidates that have p_T and β^{-1} values lower than both selection thresholds while the $B(C)$ group contains candidates that have only the p_T (β^{-1}) below its threshold. The groups containing the candidates with β^{-1} below the its threshold only contains candidates with $1 < \beta^{-1} <$ threshold. Candidates with $\beta^{-1} < 1$ are used to evaluate how well the prediction performs. The D group contains candidates passing both thresholds and is considered the signal region.

The predicted number of collision muons in the signal region is found via the relation $B \times C/A$. This relation is accurate so long as the ratio of candidates passing the β^{-1} cut is the same regardless of whether the p_T cut is passed, the statement is also true reversing the roles of β^{-1} and p_T. It has been observed that a correlation exists between the p_T and β^{-1} measurements based on whether the candidate is in the central or forward region of the detector as well as the number of DT or CSC stations containing valid hits. This can be seen in Figure 5.18 which the shows the p_T and β^{-1} distributions in the six regions. The split between the central and forward regions is done at an $|\eta|$ value of 0.9. The predicted number of events in each region is predicted separately and the total number of predicted background events is the sum of the six predictions.

After the binning the correlation is small enough not to bias the background prediction as can be seen in Figs. 5.19 and 5.20
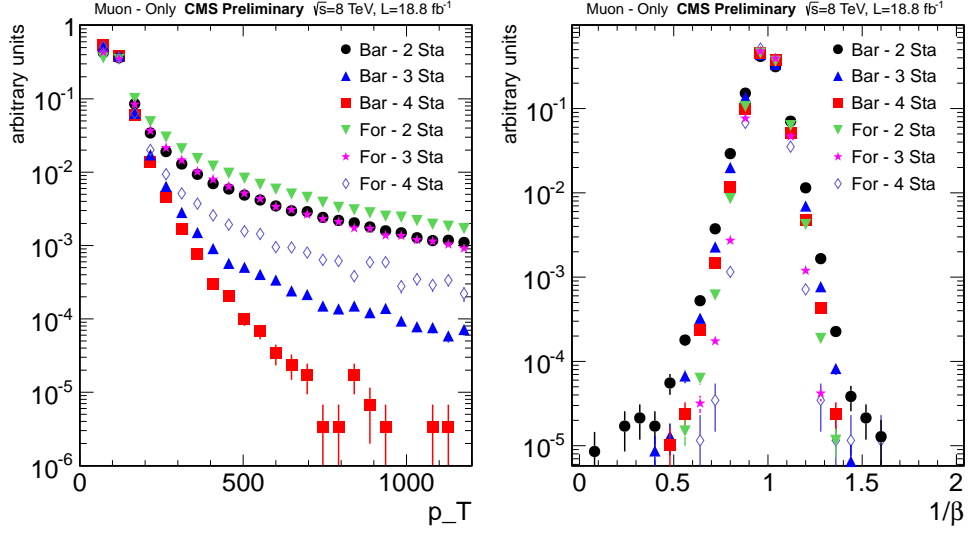
Figure 5.18: Distribution of p_T and β^{-1} for data for six different regions.

To predict the cosmic background sidebaneds in the $|\delta_z|$ distribution and the pure cosmic sample are used. The number of candidates, N, in a sideband region of $\delta_z|$ are counted. The candidates are required to pass the full selection except the $|\delta_z|$ cut is changed to $70 < |\delta_z < 120$cm and the cuts on $|\delta_{xy}|$, ϕ, segment η separation, and p_T are removed to increase the number of cosmics in the sideband region. Additionally the candidates are required not to be reconstructed as global tracks to decrease the contamination from collision muons. The ratio of candidates in the $|\delta_z|$ sideband region relative to the signal region, R, is calculated using the pure cosmic sample with the same offline requirements as in the main data sample. The number of cosmic tracks passing the final selection is then predicted as $P_{Cosmic} = N \times R$.

Numerous effects cancel in this ratio making the prediction robust. The number of cosmic tracks in any of the regions can be expressed as $C = F \times T \times \epsilon$, where C is the number of cosmics observed, F is the flux of cosmics per second, T is the amount of time that CMS was collecting data, and ϵ is the efficiency of the
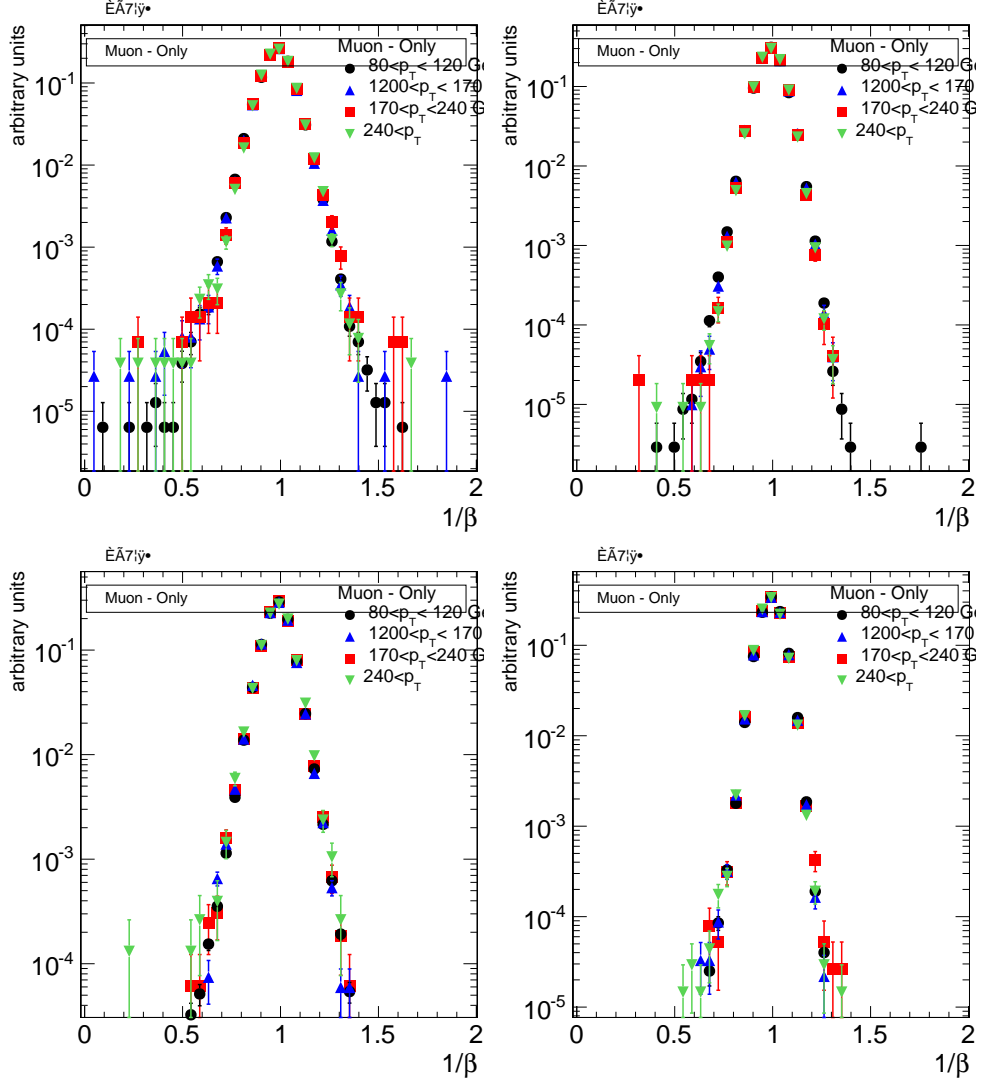
Figure 5.19: Distribution of β^{-1} for different momentum regions for four of the six different bins of number of stations that are used to make the prediction. The left column shows the central region while the right column shows the forward region. The top (bottom) columns are for 2 (3) stations.
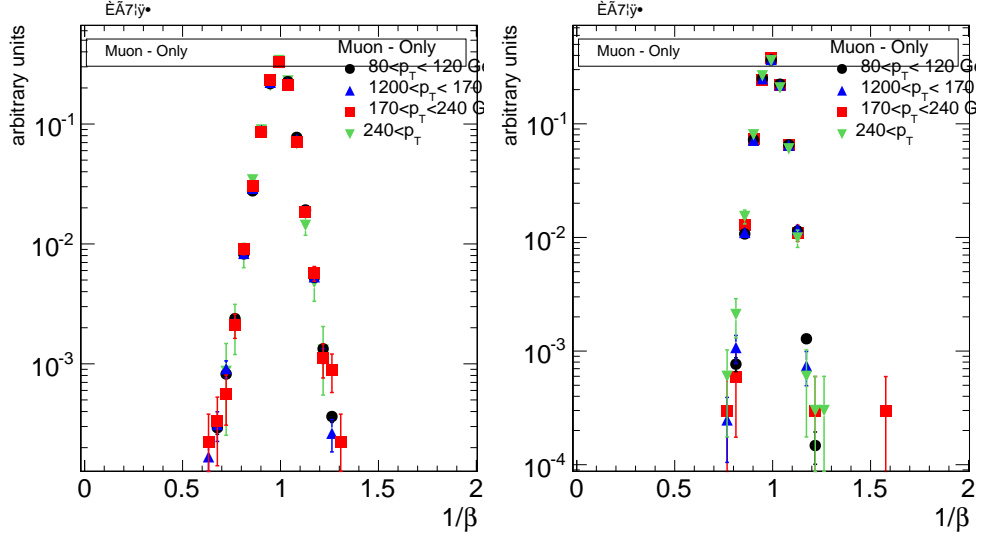
Figure 5.20: Distribution of β^{-1} for different momentum regions for four station tracks. The left column shows the central region while the right column shows the forward region.

detector to reconstruct and select cosmic tracks in the region including fiducial effects. The prediction of the number of cosmic tracks in the signal region can then be stated as

$$F \times T_{Main} \times \epsilon_{Main}^{Signal} = F \times T_{Main} \times \epsilon_{Main}^{Sideband} \times$$
$$F \times T_{Control} \times \epsilon_{Control}^{Signal} / (F \times T_{Control} \times \epsilon_{Control}^{Sideband}) \tag{5.4}$$

where Main and Control differentiate between the main triggers used in the analysis from the cosmic control trigger, respectively, and signal and sideband represent the signal region and $|d_z|$ sideband, respectively. After the cancellation of numerous factors this equation reduces to

$$\epsilon_{Main}^{Signal} = \epsilon_{Main}^{Sideband} \times \epsilon_{Control}^{Signal} / \epsilon_{Control}^{Sideband} \tag{5.5}$$

It is clear that as long as the relationship

$$\epsilon_{Main}^{Signal}/\epsilon_{Main}^{Sideband} = \epsilon_{Control}^{Signal}/\epsilon_{Control}^{Sideband} \qquad (5.6)$$

holds the prediction will be accurate. The only difference between the two ratios is that one is using events collected with the main triggers while the other is using the cosmic control triggers. As the two triggers are essentially the and same were collected during the same run period it is very likely the relationship holds so as to give a good prediction of the number of cosmic tracks in the signal region. Note that the relationship does not require the efficiency in the cosmic control sample to be the same as in the main sample. Only that the ratio of the efficiencies in the signal and sideband regions be the same in the two samples.

As previously mentioned, the background prediction is checked using candidates with β^{-1} less than one. The β^{-1} distribution is roughly symmetrical about one. Additionally the contribution from signal candidates is very small, becoming completely negligible for lower β^{-1} values. This means that this region is good for comparing the predicted number of events with what is observed. This is done by defining four new groups similar to the $ABCD$ above but changing the requirement on β^{-1} to be having a value lower than some threshold. The names are the same as $ABCD$ but with a prime added. Meaning that the D' group contains candidates with p_T above the threshold and β^{-1} below a threshold. Using the same formula as above the predicted number of candidates in the D' group can be predicted as $C' \times B'/A'$. Figure 5.21 shows the number of predicted and observed number of candidates in D' for different p_T and β^{-1} cuts. Good agreement is seen between observed and predicted.

To determine the systematic uncertainty on the predicted collision background the β^{-1} less than one region is used once again. The predicted number of events
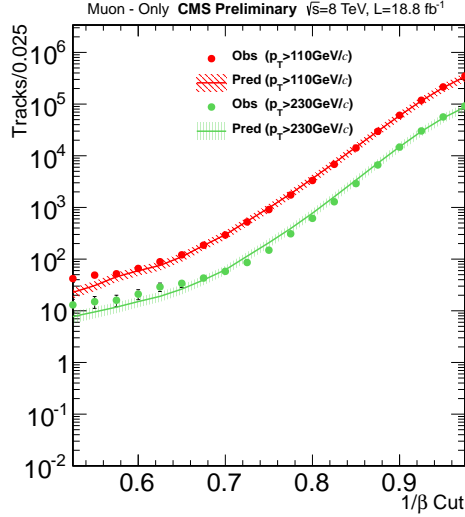
Figure 5.21: Number of predicted and observed events in $\beta^{-1} < 1$ region for two different p_T thresholds. Threshold for β^{-1} set by X-axis.

in the signal region D can be predicted by three different formulae, the main one of $C \times B/A$ as well as $C' \times B/A'$ and $D' \times B/B'$. The first of these additional predictions would be sensitive to any shift in the β^{-1} distribution due to the p_T requirement while the second would be sensitive to any effect on the resolution due to the p_T requirement. Figure 5.22 shows the number of predicted events from the three predictions for different β^{-1} and p_T cuts.

The systematic error is extracted from the three predictions through Eq. 5.3 with N=3. Fig. 5.23 shows the variation of $V_{syst+stat}/ < x >$, $V_{stat}/ < x >$ and $V_{syst}/ < x >$ as a function of the p_T threshold. The statistical uncertainty due to the number of candidates in the B group is not subtracted as it is completely correlated between the three predictions. From the last plot the systematic uncertainty on the expected background in the signal region is estimated to be 20%.

The systematic uncertainty on the cosmic background is determined by mod-
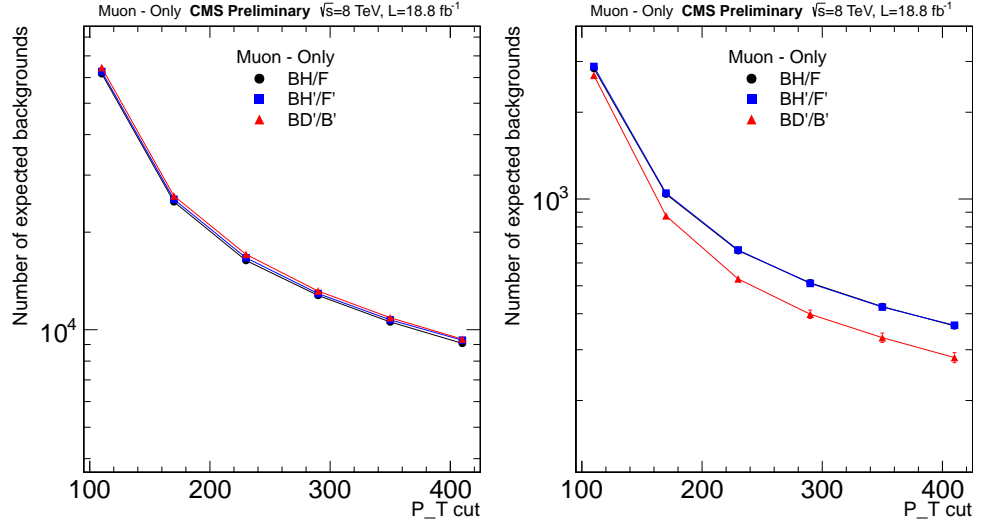
Figure 5.22: Distribution of the number of predicted events and their statistical error computed for the *muon only* analysis with different predictions for different set of cuts. The p_T threshold is defined by the x-axis. Left column: $1/\beta > 1.1$ (< 0.9 for low $1/\beta$ regions). Right column: $1/\beta > 1.2$ (< 0.8 for low $1/\beta$ regions).
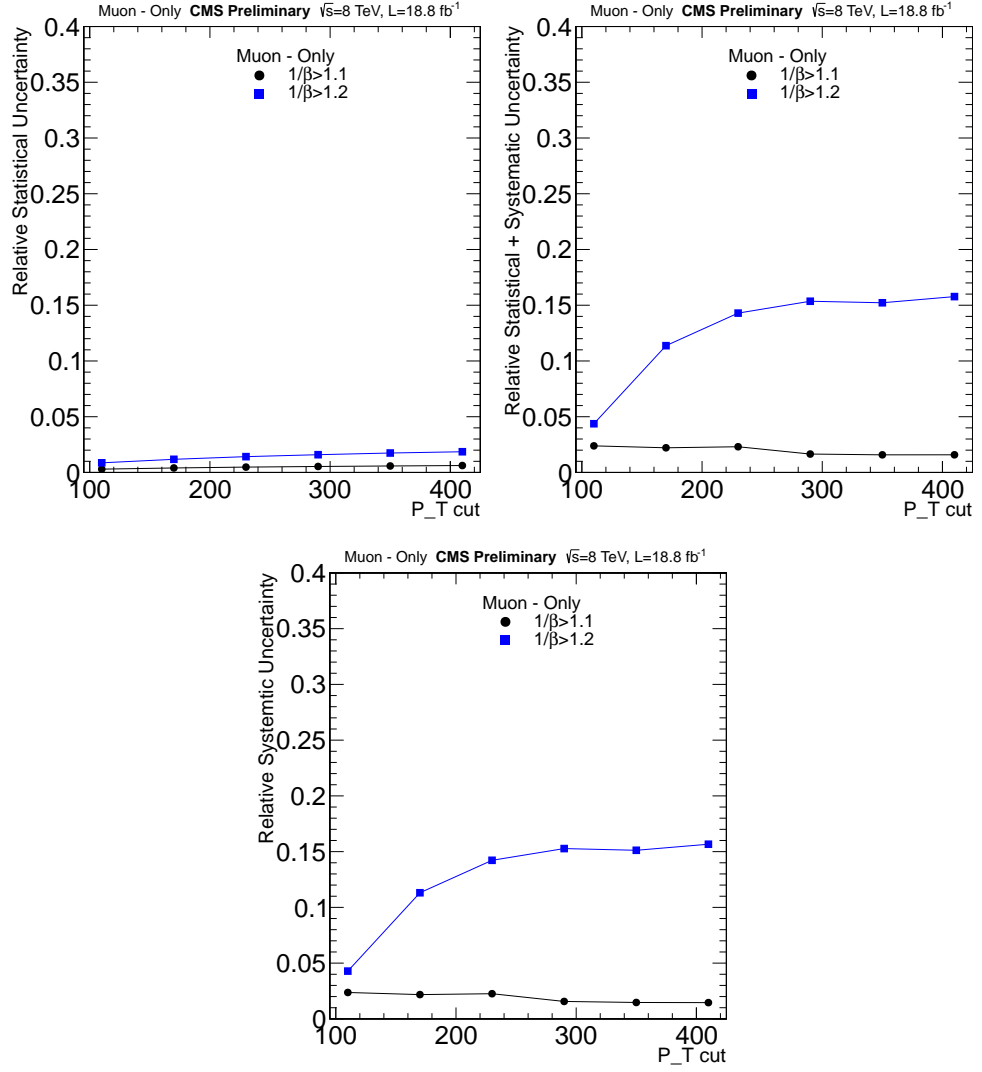
Figure 5.23: Left: Ratio of the quadratic mean of the statistical uncertainties of the three possible background estimations to the mean of these estimations vs the p_T threshold. Middle: Ratio of the variance to the mean of the three background estimations vs p_T. Right: Ratio of the square root of the difference between the variance and the quadratic mean of the statistical uncertainties of the three possible background estimations and the mean vs p_T.

Table 5.5: Predicted numbers of cosmic events for the *muon only* analysis.

Dz Region	Prediction
$30 < |dz| < 50$ cm	3.1 ± 0.5
$50 < |dz| < 70$ cm	2.6 ± 0.7
$70 < |dz| < 120$ cm	3.2 ± 1.0
120 cm $< |dz|$	3.8 ± 0.7

ifying the d_z range used to define the control sample. Predictions can also be made from candidates with $30 < |d_z| < 50$ cm, $50 < |d_z| < 70$ cm, and 120 cm $< |d_z|$. Table 5.5 shows the number of predicted cosmic tracks for each $|d_z|$ region using the final selection defined in Section 5.9 The statistical uncertainty from the number of candidates in the signal region in the pure cosmic sample is not included in the uncertainties as it is correlated between the three predictions. Equation 5.3 with N=4 is used to calculate the systematic uncertainty. The relative systematic uncertainty is found to be 80%.

5.7.2   Prediction for *muon+track* analysis

The *muon+track* analysis uses three selection variables, p_T, β^{-1}, and dE/dx. With three selection variables an extended three dimensional version of the $ABCD$ method described in Subsection 5.7.1 is used to predict the collision muon background. An additional cut on the estimated mass of the candidate is also applied and the prediction of the background mass prediction is described below. As discussed above the cosmic background is negligible for the *muon+track* analysis. The variables have been found ot be uncorrelated to a sufficient degree as can be seen in Fig. 5.24.

Four new groups are defined, E, F, G, and H. The D region still represents
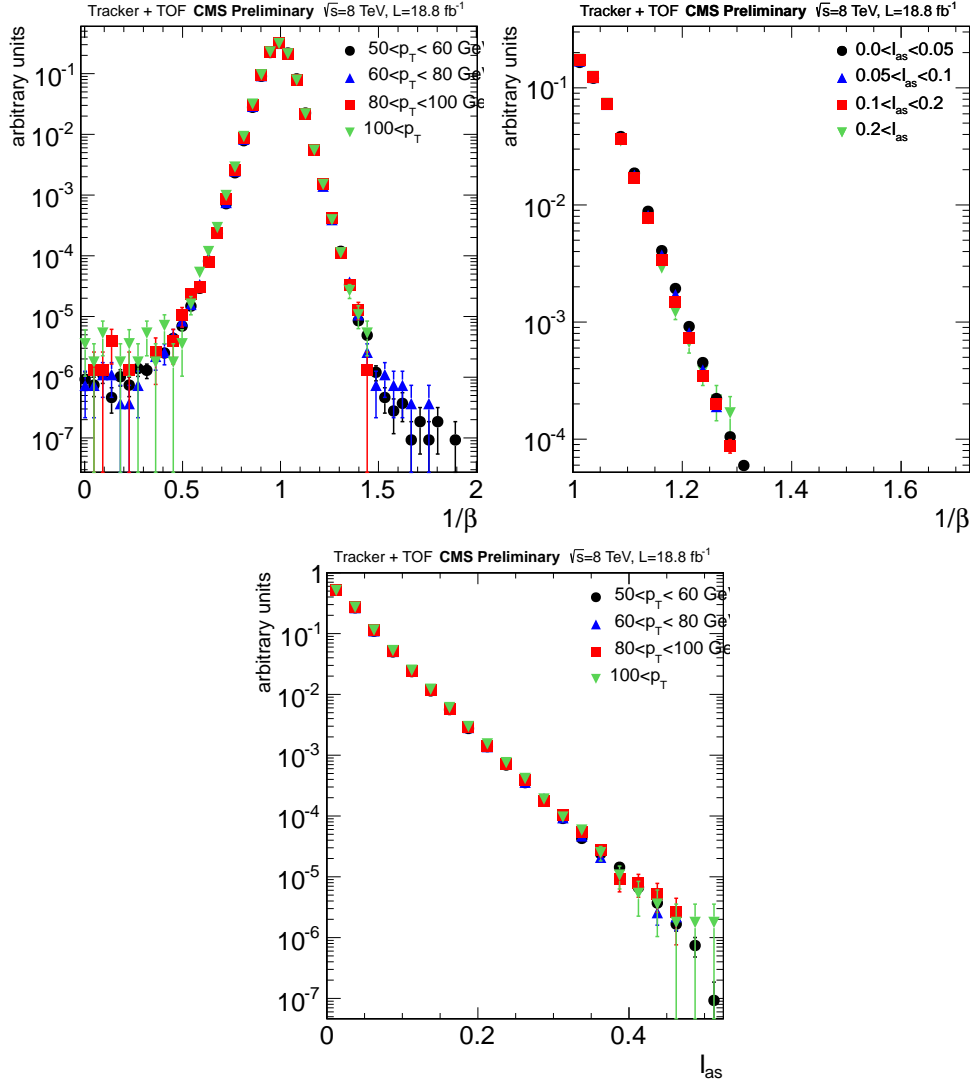
Figure 5.24: Left column: Measured I_{as} distributions for several momentum ranges. Middle column: Measured $1/\beta$ distributions for several momentum ranges. Right column: Measured $1/\beta$ distributions for several I_{as} ranges. Results are for the *muon+track* selection. The first row is for a center of mass energy of 7 TeV while the second row shows the results at 8 TeV.

the signal region where the candidate passes the thresholds on all three selection variables. The B, C, and H regions pass two of the thresholds and fail β^{-1}, p_T, and dE/dx, respectively. The A, F, and G groups contain candidates passing only the dE/dx, β^{-1}, and p_T thresholds, respectively. The number of predicted events in the signal region, D, can be found via seven different equations utilizing the various groups. The one with the smallest statisitical uncertainty, $A \times F \times G/E^2$, is chosen. The other equations are used to determine the systematic uncertainty on the prediction.

It has been found that the probability for background candidates to pass the threshold on I_{as} is strongly dependent on the η of the candidate. This could bias the prediction if the probability to pass the threshold for the other selection variables also has a large η dependence. The probability to pass the β^{-1} threshold has a small η dependence while the probability to pass the p_T cut has almost no η dependence. These effects can be seen in Figure 5.25 that shows the η distribution of candidates which pass or fail the various thresholds. The effect is found to have a small effect on the total number of predicted events and is covered by the systematic uncertainty defined below.

As with the *muon only* analysis the prediction is checked with candidates in the β^{-1} less than on region. Again the predicted number of events in D' is predicted following the same procedure as for the signal region except changing the β^{-1} requirement to be lower than some threshold. Figure 5.26 shows the predicted and observed number of candidates in the D' region for various cuts. Good agreement is seen even with a tight selection.

In addition to the cut on the selection variables, the *muon+track* analysis also applies a cut on the estimated mass of the candidate as determined from Equation 5.1. In order to do this the mass spectrum of background candidates in
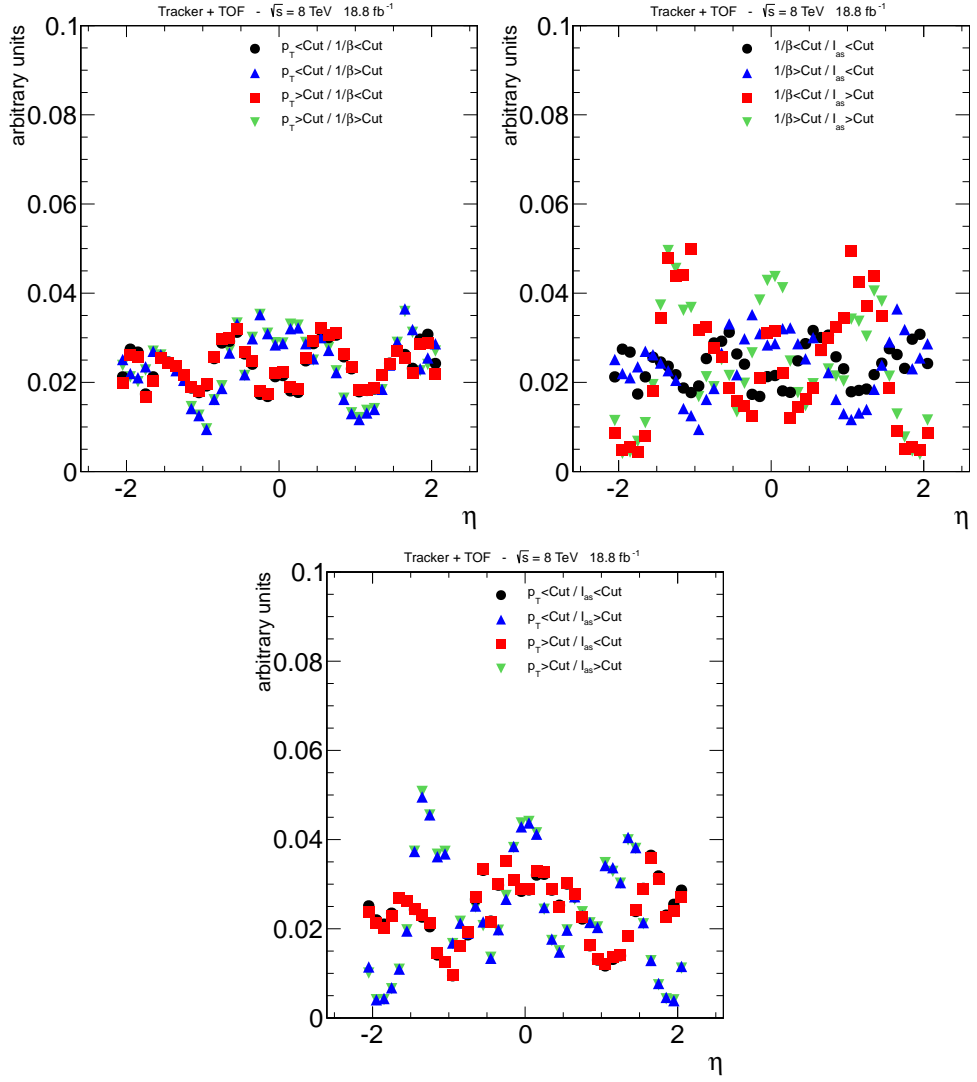
Figure 5.25: Distribution for data of the candidate η for various combinations of being above or below selection thresholds of 50 GeV for p_T, 1.05 for β^{-1}, and 0.05 for I_{as}. Top left: Combinations of flipping p_T and β^{-1} cuts. Top Right: Combinations of flipping β^{-1} and I_{as} cuts. Bottom: Combinations of flipping p_T and I_{as} cuts. For all plots the variable not flipped is required to be below the threshold.
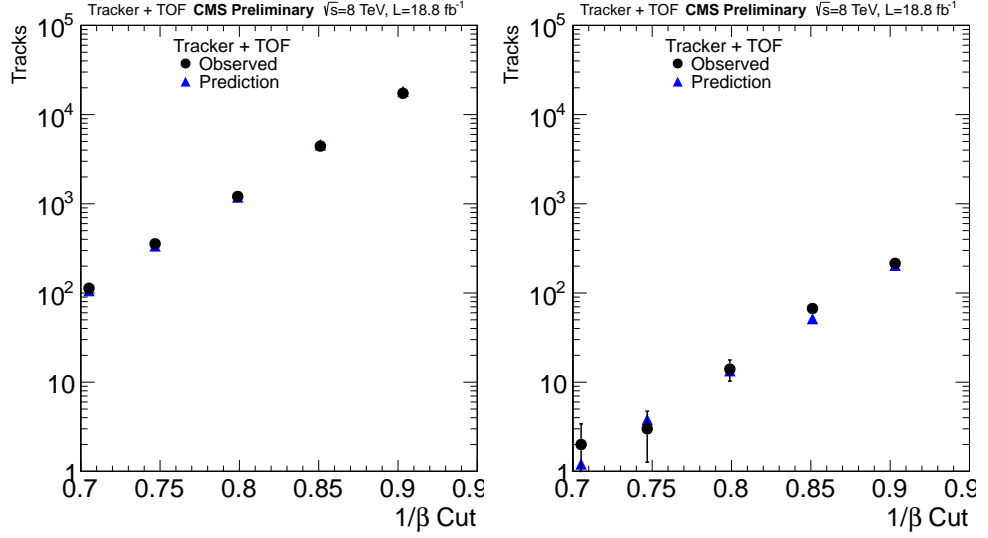
Figure 5.26: Number of observed and predicted events and their statistical error in the D' region for $p_T > 55, I_{as} > 0.1$ (left) and $p_T > 85, I_{as} > 0.2$ (right). Threshold on $1/\beta$ defined by the x-axis in the *muon+track* analysis.

the signal region must be predicted. The background mass spectrum is predicted using the dE/dx and momentum distributions taken from control regions. While the signal region is defined by cuts on I_{as} and p_T (as well as β^{-1}), the mass prediction uses I_h and p so it is these distributions that must be taken from the control regions. As discussed above the dE/dx variables have a strong η dependence. While this issue does not have a large effect on the total number of predicted events is does affect the mass distribution. The p_T distribution of background candidates is roughly the same versus η however this implies that the p distribution does vary as momentum can be written as a function of only p_T and η. To correct for this a reweighting procedure is done such that the candidates used to determine the p distribution match the η distribution of candidates used to obtain the I_h distribution.

The p, I_h, distribution is taken from G, A, where only the p_T, I_{as}, value is above threshold and the other two are below. The mass distribution is then predicted by performing approxiamtely 100 pseudo-experiments. The ith pseudo-experiment is done through multiple steps. First a value of E_i, F_i, is drawn from a poisson distribution with a mean equal to the observed number of candidates in the E, F, regions in data. Next, a binned distribution of the p of candidates in the G region is employed. A value of n_{ij}, where j represents the bin of the p distribution, is drawn for each p bin from a poisson distribution with mean equal to the number of candidates observed in that bin in data. A value of G_i is then found as the sum over j of the n_{ij}. A similar procedure is done in the A region for determining the I_h distribution. Before the distribution is found, weight factors are attached to all of the candidates in the A region so that the η distribution of candidates in the A region matches that observed in the G region as necessitated by the conversation above. Next, a value of m_{ik} is found for each bin of the reweighted I_h distribution. A value of A_i is then found by summing over m_{ik} over k. The predicted number of background candidates in the signal region for a given i–j bin in the $p - dE/dx$ plane, D_{ijk}, is then found via the relation

$$D_{ijk} = (A_i \times F_i \times G_i/E_i^2) \times (n_{ij}/G_i) \times (m_{ik}/A_i) = F_i \times n_{ij} \times m_{ik}/E_i^2 \quad (5.7)$$

The predicted candidates in D_{ijk} are taken to have a mass equal to the mass coming from Equation 5.1 with the p and I_h values determined by the bin that j and k represent in the p and I_h distributions, respectively. The mass distribution for the ith pseudo-experiment is then found by summing over the j and k of all the D_{ijk} and their representative masses.

The value in each mass bin is then found as the average of the value in all the pseudo-experiments. The statistical error is taken as the standard deviation
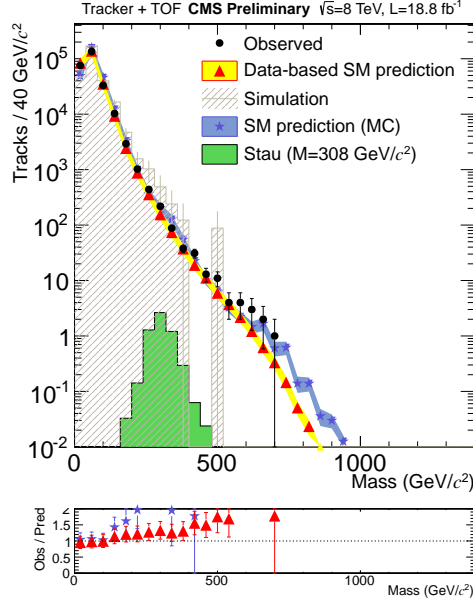
Figure 5.27: Observed and predicted mass spectrum for candidates in the D' region in the *muon+track* subanalysis. Left: $p_T^{cut} > 55$ GeV, $I_{as} > 0.1$ and $1/\beta < 0.95$. Right: $p_T^{cut} > 85$ GeV, $I_{as} > 0.1$ and $1/\beta < 0.8$. The error bands are only statistical.

of the values from the pseudo-experiments. The prescription for determining the predicted background mass shape was done by another scientist working on CMS and is simply reproduced here.

The mass distribution with loose thresholds on the selection variables is shown in Fig. /reffig:MassDistribution.

As the β^{-1} value of candidates is not currently used in the mass estimation the predicted and observed mass spectrums in the $\beta^{-1} < 1$ region can be found by only changing the groups that the candidates be drawn from be the regions with a prime (e.g. A'). Using the $\beta^{-1} < 1$ region allows for checking the predicted
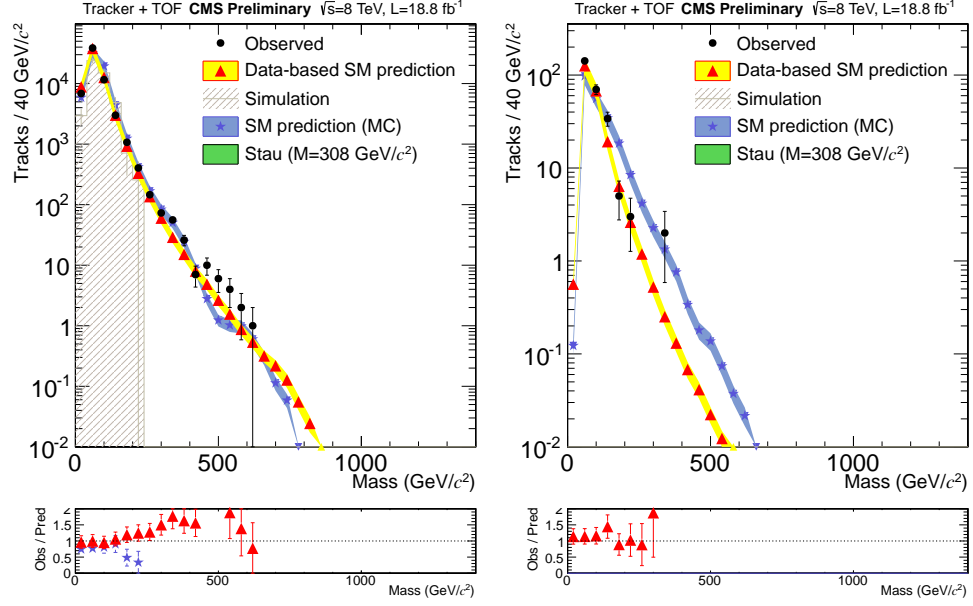
Figure 5.28: Observed and predicted mass spectrum for candidates in the D' region in the *muon+track* subanalysis. Left: $p_T^{cut} > 55$ GeV, $I_{as} > 0.1$ and $1/\beta < 0.95$. Right: $p_T^{cut} > 85$ GeV, $I_{as} > 0.1$ and $1/\beta < 0.8$. The error bands are only statistical.

mass distribution in a background dominated region even when applying tight cuts. The predicted and observed mass distributions are shown in Figure 5.28 with both loose and tight thresholds on the selection variables.

The systematic uncertainty on the background prediction for the *muon+track* analysis is evaluated by using the multiple different possible when using the three dimensional variation of the $ABCD$ method. As mentioned above, in addition to the chosen prediction of $A \times F \times G/E^2$, there are six more equations that can be used to predict the amount of background in the signal region. Of the six, three have small statistical uncertainty. Those three are $A \times H/E$, $B \times G/E$, and $F \times C/E$. The chosen prediction includes the group where all the variables are

below the threshold and the three where exactly one threshold is passed. The three additional prediction include the group where all the thresholds are failed, one of the regions where exactly one threshold is passed, and one of the regions where exactly two of the thresholds are passed.

The three additional background predictions each test the correlation between two of the three selection variables. Using $A \times H/E$ as an example but the argument is the same for the other predictions. Comparing $A \times H/E$ with the chosen background prediction of $A \times F \times G/E^2$ it can be seen that the difference is replacing $F \times G/E$ with H. The E group fails all three thresholds, the F and G groups pass only the β^{-1} and p_T thresholds, respectively, and the H group passes the β^{-1} and p_T thresholds but not dE/dx. If β^{-1} and p_T are uncorrelated then the equation $F \times G/E$ should predict the number of candidates in the H region. So a comparison of the two predictions will test how well the assumption that the variables are uncorrelated works. Likewise, the predictions $B \times G/E$, and $F \times C/E$ test for possible correlation between p_T and dE/dx as well as β^{-1} and dE/dx, respectively.

The number of predicted events coming from the four predictions is shown in Figure 5.29. The spread of the four predictions is used to extract the systematic through the Equation 5.3 with N=4. The statistical and systematic uncertainties are shown in Figure 5.30. From the last plot the systematic uncertainty is taken to be 20%.

5.7.3   Prediction for *track only* analysis

The prediction for the *track only* is done in the same manner as the *muon+track* analysis except only the variables p_T and I_{as} are used in a traditional two dimensional ABCD method. The predicted and observed number of events and
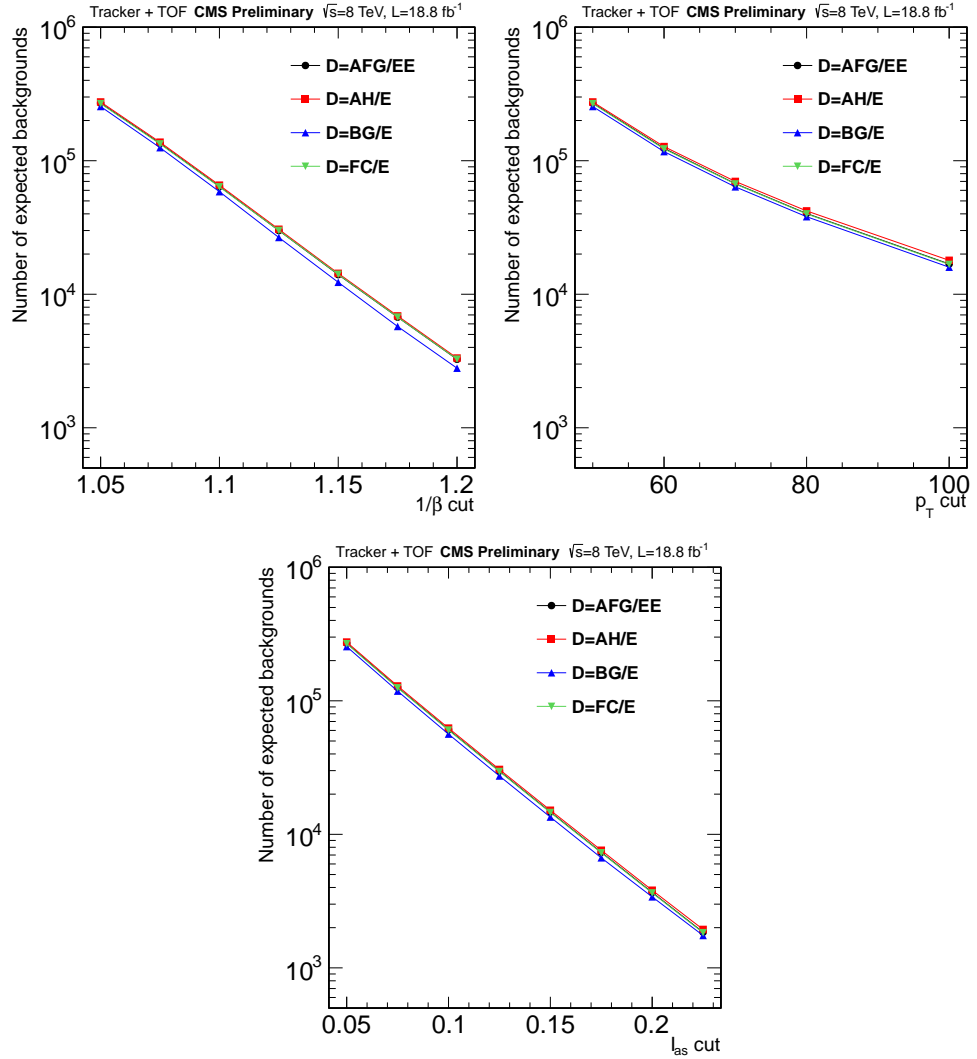
Figure 5.29: Number of predicted candidates from four different background predictions. Top Left: p_T and I_{as} threshold of 50 GeV and 0.05, respectively. Threshold on β^{-1} set by X-axis. Top Right: Threshold on β^{-1} and I_{as} of 1.05 and 0.05, respectively. Threshold on p_T set by X-axis. Bottom: Threshold on β^{-1} and p_T of 1.05 and 50 GeV, respectively. Threshold on I_{as} set by X-axis.
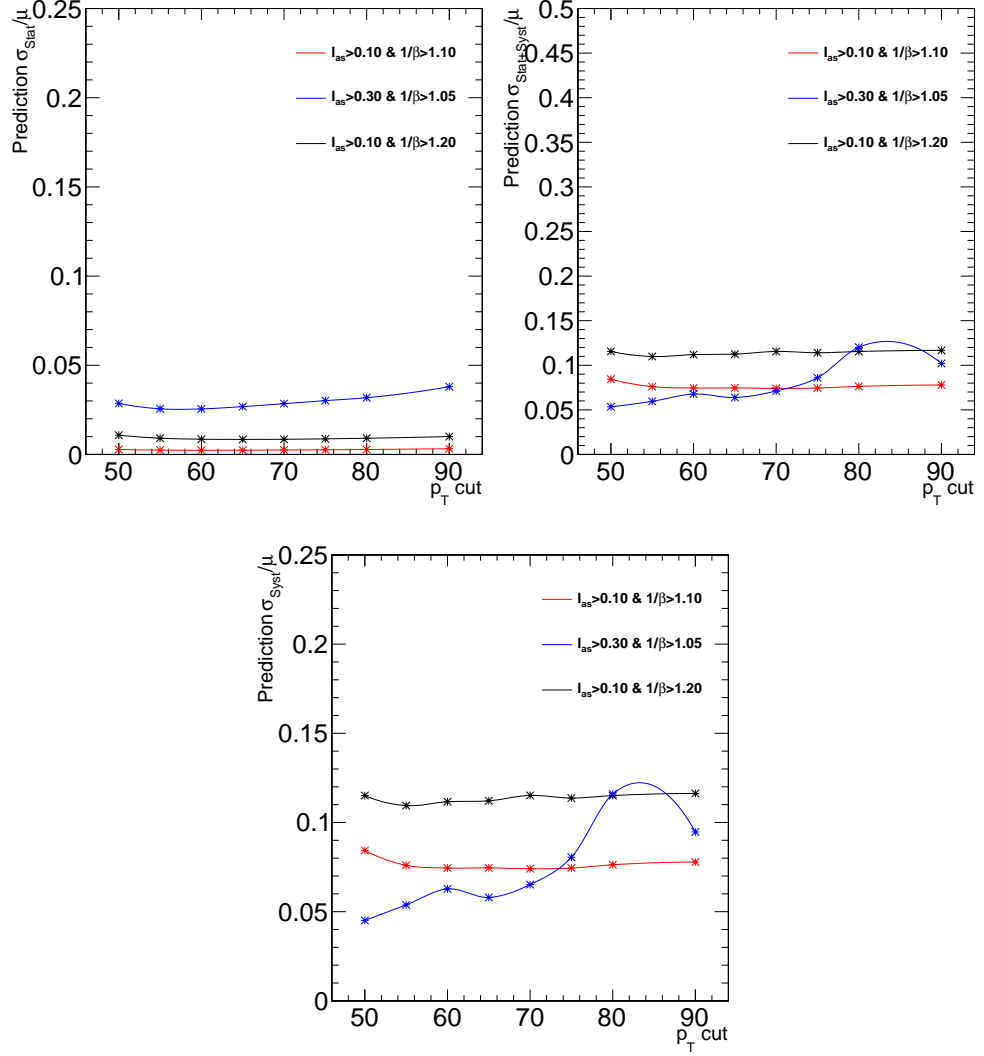
Figure 5.30: Left: Ratio of the quadratic mean of the statistical uncertainties of the four background estimations to the mean of these estimations vs the p_T threshold. Middle: ratio of the variance to the mean of the three background estimations vs p_T. Right: ratio of the square root of the difference between the variance and the quadratic mean of the statistical uncertainties of the three possible background estimations and the mean vs p_T.
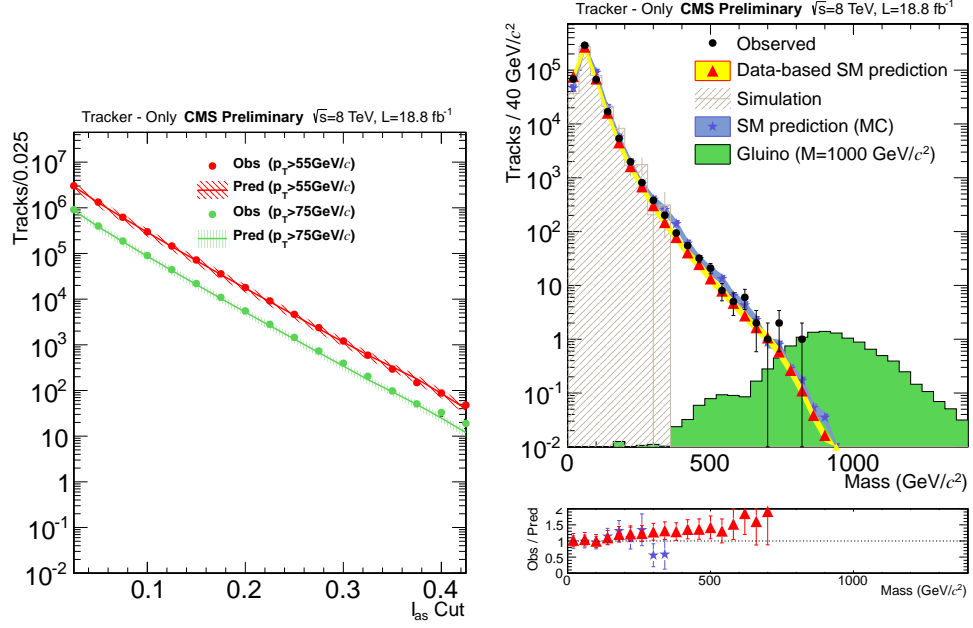
Figure 5.31: Left: Number of predicted and observed tracks for various p_T and I_{as} thresholds. Right: Observed and predicted mass spectrum for candidates in the D region in the *track only* analysis. Loose selection thresholds of $p_T >?$ and $I_{as} >?$ are used.

mass spectrums with various selection thresholds are shown in Fig. 5.31, good agreement is seen. The systematic uncertainty on the background prediction for the*track only* analysis is taken as the same as in the *muon+track* analysis.

5.7.4 Prediction for *multiple charge* analysis

The *multiple charge* analysis employs a two dimensional ABCD method using the variables β^{-1} and I_{as} without a mass cut. The mass cut cannot be used as the mass estimation assumes Q=1e and the large amount of saturation of the tracker readout. The background prediction is checked both by using the control region
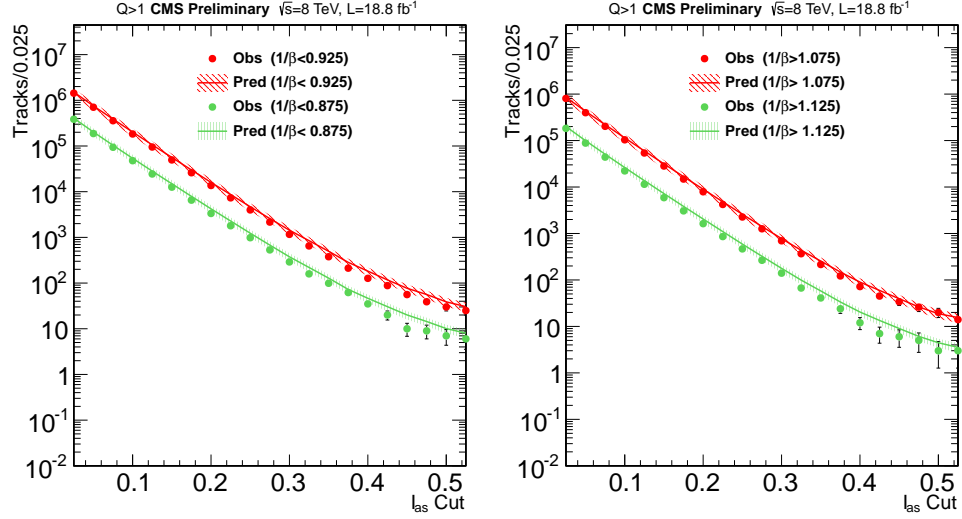
Figure 5.32:

with $\beta^{-1} \lt 1$ as was done for the *muon only* analysis and with loose thresholds on the selection variables. Figure **??** shows the number predicted and observed number of tracks for various β^{-1} and I_{as} thresholds in both the β^{-1} less than one and greater than one regions, good agreement is observed.

5.8 Statistical Technique

CMS has a Statistics Committee which provides advice on statistics issues as well tools which can be used to perform statistical calculations. The tools were used in this analysis to get the significance of any observed excess and if no excess is observed to place bounds on the signal cross-section.

One of the tools takes in the predicted background with its uncertainty and the observed data. It then calculates the probability that the observed data come from background only. The probability is returned in the form of a one-sided Gaussian sigma. For a given sigma, x, the probability, p, is found from

Equation 5.8,

$$p = \int_x^\infty \frac{1}{\sqrt{2\pi}} e^{\frac{-x^2}{2}} \, \mathrm{dx}. \tag{5.8}$$

the function being integrated over is a normalized gaussian with unit variance. Particle physics has a convention that one claims a discovery when the significance is greater than five sigma and evidence when it is greater than three. A five sigma discovers means that there is a one in 3.5 million probability that observed data comes from background only.

Another tool returns the expected and observed cross-section limit on signal cross-section. The tool is passed the different sources of background with their uncertainties, the signal efficiency with its uncertainty, and finally the integrated luminosity with its uncertainty. The tool then proceeds to calculate the cross section limits with a hybrid CLs approach [16] using a profile likelihood technique with the predicted background, signal efficieny, and integrated luminosity as nuisance parameters using lognomal pdfs [17, 18].

A combination of the above two tools can also be used find the expected reach of the analysis. The expected reach of the analysis is defined as the signal cross section for which there is a 50% chance of being able to claim a discovery. This is of particular experience when designing the analysis to determine optimum thresholds on the selection variables.

5.9   Cut Optimization

Both the *muon only* and *muon+track* analyses calculate the amount predicted and observed for numerous different sets of thresholds. The *muon only* analysis evaluates thresholds with the β^{-1} threshold ranging from 1.025 to 1.475 and the
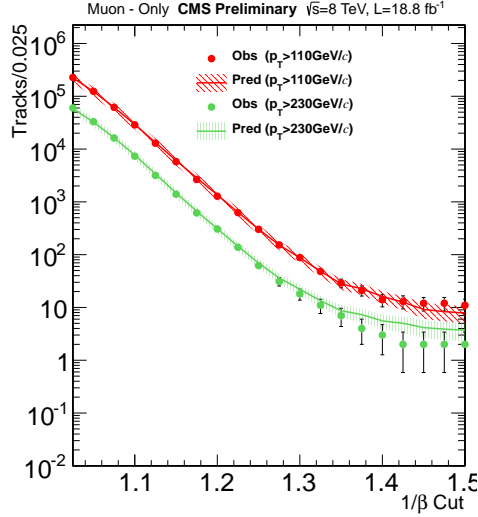
Figure 5.33: Number of predicted and observed events for two different p_T thresholds. Threshold for β^{-1} set by X-axis.

p_T threshold ranging from 110 GeV to 450 GeV for a total of 240 different sets. The *muon+track* analysis varies the β^{-1} threshold from 1.025 to 1.325, the p_T threshold from 50 GeV to 115 GeV, and the I_{as} threshold from 0.025 to 0.375 for a total of 2,101 different sets. The number of predicted and observed events for a few sets of thresholds for the *muon only* analysis is shown in Figure 5.33. A similar plot is shown for the *muon+track* analysis in Figure 5.34. The observed and predicted mass spectrum is shown in Figure 5.35.

The thresholds on the selection variables are set trying to optimize two quantities, the expected reach and cross-section limit. The two variables give the power of the analysis for two different hypotheses. Expected reach is concerned with the likelihood of finding a signal if it does exist while the expected limit is concerned with excluding the signal if it does not exist.

When optimizing the expected reach it is necessary to be careful not to optimize to a region with very small predicted background at the expense of signal

Figure 5.34: Number of observed and predicted events and their statistical error in the D region for $p_T > 55, I_{as} > 0.1$ (left) and $p_T > 80, I_{as} > 0.2$ (right). Threshold on $1/\beta$ defined by the x-axis

efficiency. The reason is that for very small predicted background it is possible to have a five sigma significance with other one or two events. For example, one observed event will give a five sigma significance for a predicted background of 2.87×10^{-7}. However, a single event is not enough to claim discovery of new physics. To protect against this, the definition of the expected reach is modified to be at least as large as the cross-section which is expected to give at least five events.

Most of the time, the two variables agree which of two sets of thresholds is better however in some conditions the variables will disagree. One such case is analyses that have little predicted background and high efficieny for the signal to pass the thresholds on the selection variables. This is the case for high mass samples in the *muon+track* analysis.
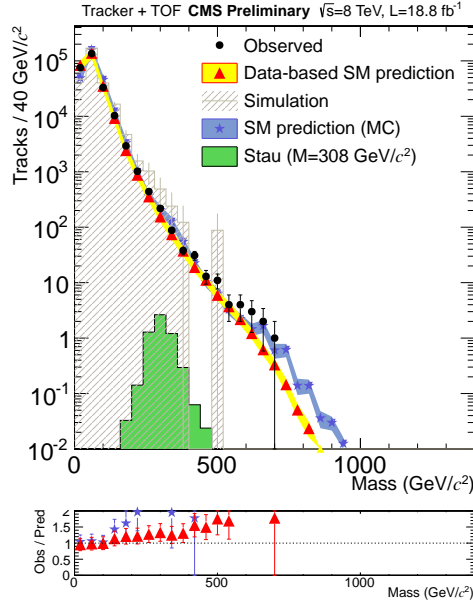
Figure 5.35: Observed and predicted mass spectrum for candidates in the D region in the *muon+track* analysis with loose thresholds of $p_T^{cut} > 55$ GeV, $I_{as} > 0.05$ and $1/\beta > 1.05$. The error bands are only statistical.

Once the expected cross-section limit falls below the point where more than 50% of the time zero events would be observed the expected cross-section limit no longer improves by decreasing the expected background. Any loss of efficiency caused by raising the threshold on the selection variables will cause the expected cross limit to be optimized at this cross over point. The cross over occurs at approximately 0.6 predicted events with the uncertainties used in the *muon+track* analysis.

The expected reach continues to improve by making the predicted background smaller until the requirement that the expected reach be large enough to give five expected events. This occurs at approximately 0.1 predicted events.

Thus the two cut off how low the predicted background can be at different points. When the optimization for the best expected reach is used for these cases the effect on the expected cross-section limit is usually small as generally the signal efficiency does not decrease much when raising the thresholds. However when the optimization from the expected limit is used the expected reach does get noticably worse as twice? as many events are needed. This can be seen in Figs. 5.36 and 5.37 which show the ratio of the expected cross-section limit when optimizing for the best best expected reach relative to when optimizing for the best expected cross-section limit and the ratio of the expected reach when optimizing for the best expected cross-section limit relative to when optimizing for the best expected reach. This reason combined with the fact that the main goal of this analysis is to discover new physics priority is given to the expected reach when trying to optimize the threshold values.

The thresholds are optimized in a two step process. First the set of thresholds which give the best expected reach for each mass/model point is determined. However, this leads to numerous different selections being used which are often
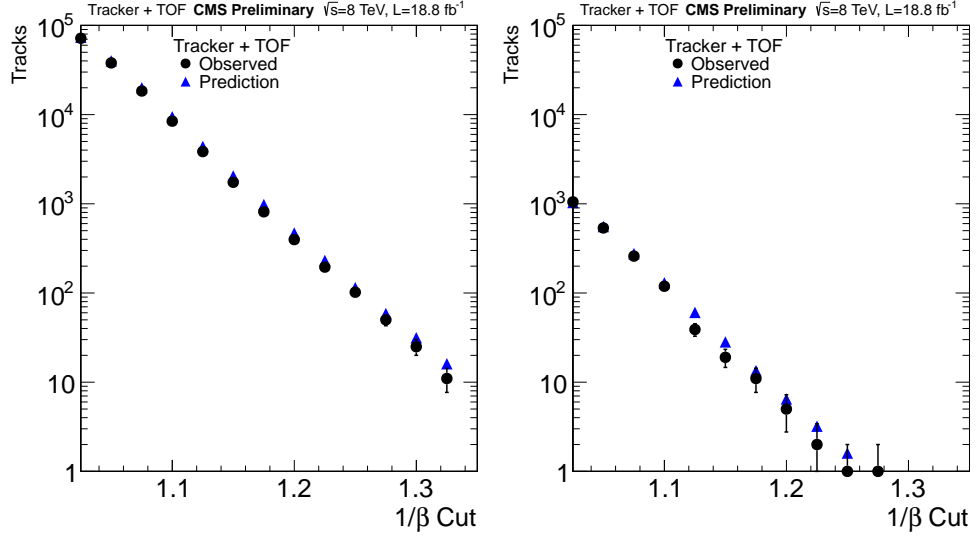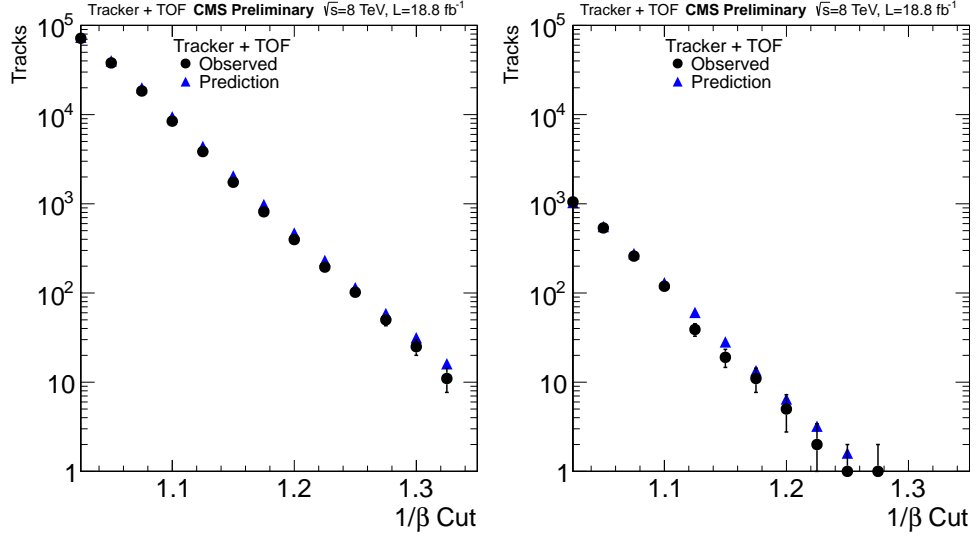
Figure 5.36: Number of observed and predicted events and their statistical error in the D region for $p_T > 55, I_{as} > 0.1$ (left) and $p_T > 80, I_{as} > 0.2$ (right). Threshold on $1/\beta$ defined by the x-axis

very similar and give about the same discriminating power. This is troublesome for two reasons.

The first is that using multiple different selections increases the risk of a statistical fluctuation of the background causing a spurious signal. To account for this a correction must be applied to the obtained local significance such that the value is correctly set to the probability of finding the signal in any of the used sets of thresholds. This means that the global expected reach could be improved by using fewer sets of thresholds even if it comes with the price of making the local expected reach worse.

The second reason is that the analysis becomes much more difficult to understand as there are multiple different sets of thresholds being used as well as multiple predicted and observed events. This complexity brings with it little
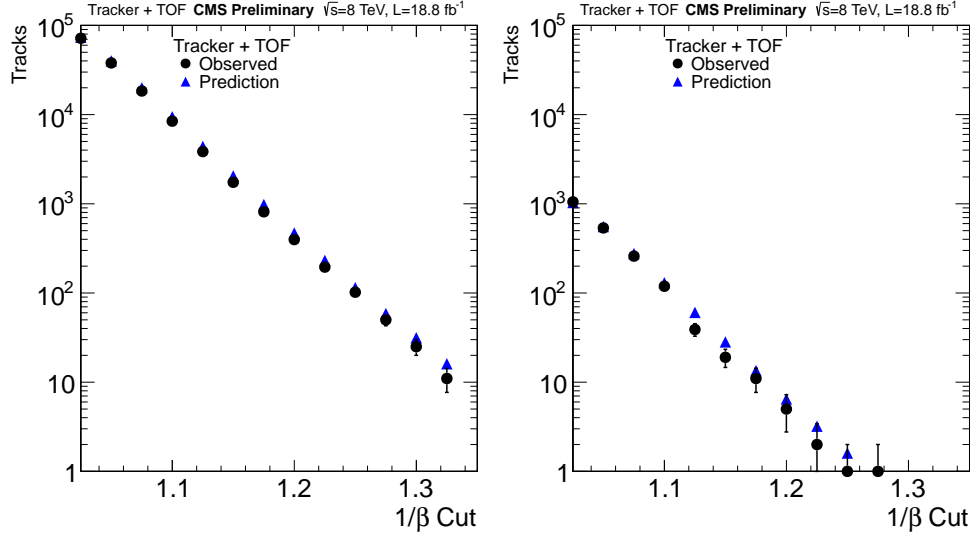
Figure 5.37: Number of observed and predicted events and their statistical error in the D region for $p_T > 55, I_{as} > 0.1$ (left) and $p_T > 80, I_{as} > 0.2$ (right). Threshold on $1/\beta$ defined by the x-axis

additional gain in the expected reach or cross section limit and unnecessary complexity is not something that is desired in an analysis. No matter how robust an analysis is, if it can not be understood by others then it can not have an impact on the scientific community at large.

For these reasons a second step is taken attempting to make the thresholds the same for the various mass/model points. If the harm to mass/model points to having the same thresholds is too large then using more than one set of thresholds is possible. However this was found not to be necessary and a single cut value is used in both the *muon only* and *muon+track* analyses. The final thresholds used as well as the number of observed and predicted events is shown in Table 5.6. The predicted and observed mass distribution with the final thresholds is shown in Figure 5.38.
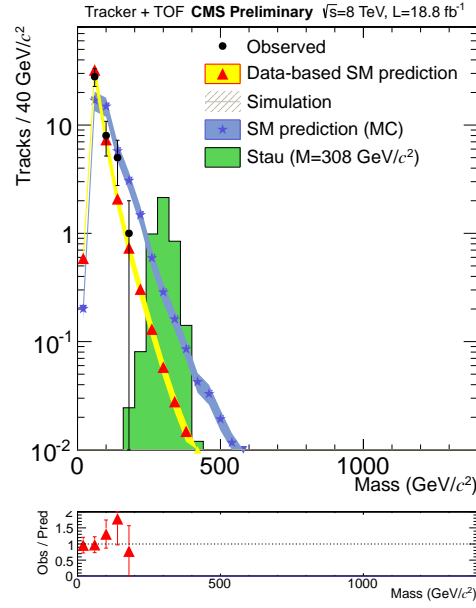
Figure 5.38: Observed and predicted mass spectrum for candidates in the D region in the *muon+track* analysis with the tight selection. The error bands are only statistical.

Table 5.6: Results of the final selections for predicted background and observed number of events. Uncertainties are statistical and systematic.

	Selection criteria				Numbers of events $\sqrt{s} = 8$ TeV	
	p_T (GeV/c)	I_{as}	β^{-1}	Mass GeV/c^2	Pred.	Obs.
muon only	> 230	-	> 1.40	-	5.6 ± 2.9	3
muon+track	> 70	> 0.125	> 1.225	> 0	43.5 ± 8.7	42
				> 100	5.6 ± 1.1	7
				> 200	0.56 ± 0.11	0
				> 300	0.090 ± 0.02	0

5.10   Systematic Uncertainties

Systematic uncertainties in this analysis can be split into three categories being the uncertainty on the number of predicted events, the signal efficiency, and the integrated luminosity. The uncertainty on the background luminosity is discussed in Section 5.7. The uncertainty is 4.4%(cite Lumi paper).

The signal efficiency in this paper is obtained from MC. To assess how well the MC matches data numerous studies were performed.

The uncertainty on the trigger efficiency can come from numerous different effects. A 5% difference on the muon trigger has been observed between data and MC(cite muon paper). An additional uncertainty uncertainty especially important to slow moving particles is the timing synchronization in the muon system. As an HSCP arrives in the muon system closer to the switching of the assigned bunch crossing number, a discrepancy in the modeling of this in MC would have

a larger effect than for SM particles. The timing of the trigger system is set at the local system level with the exact segmentation differing between the three muon subsystems. For the CSCs, the timing is set by the chamber that the particle passes through. The average trigger time with respect to the LHC clock and its RMS of each of the trigger timing components for each subsystem was measured from data. For CSCs this means a relative timing was found for each chamber and the value provided was the average of these 473 values and the RMS of the values. The average and RMS values are then used to form a gaussian distribution separately for each muon subsystem. Then, each trigger timing component, again a chamber for CSC, is assigned a shift value drawn from the gaussian representing the muon subsystem to which it belongs. The simulation of the detector electronics is then repeated with the time of the simulated hits in the detector shifted by the value associated with the portion of the detector the hit is in. Then the reconstruction and trigger simulation steps are redone. The effect on trigger efficiency was found to be less than 4%.

Also contributing to the trigger uncertainty is the accuracy of MET in MC. CMS has a group which compares the agreement between data and MC for jets. For both data and MC, the group releases corrections to the jet energy scale which can be applied after reconstruction to give the best measurement of the energy of the jet. The corrections come with corresponding uncertainties. The HLT jets that are used to calculate the MET are adjusted by their uncertainties and the MET is recalculated. The adjustment is done both by changing all of the jets to lower energy as well as applying the shift randomly by multiplying the change by a random number drawn from a normalized unit Gaussian. The effect was seen to be less than 1% in all cases.

The systematic uncertainty on muon (cite muon paper) reconstruction was

both found to be less than 2%. A 1% uncertainty recommended by the muon POG is applied on the correction factors described in Section 5.6.1.

The uncertainty on the β^{-1} measurement is studied using muons from the decay of Z bosons. Muons are required to pass a tight selection provided by the muon POG to give a pure muon sample. Additionally the event must have a pair of oppositely charged muons with a mass of $M_Z \pm 10\text{GeV}$. Only the two muons forming the combination are used. If more than one such pair exists, the pair with mass closest to M_Z is used. An uncertainty of 0.005 is taken on the β^{-1} measurement. This uncertainty has an effect less than 7% on all the considered models.

The uncertainty due to the p_T measurement is determined by varying the $1/p_T$ value by a prescription from the muon POG (cite muon paper). For the *muon only* analysis the $1/p_T$ of the stand alone track is shifted up by 10%. For the *muon+track* analysis the $1/p_T$ of the inner track is adjusted with the Equation

$$\frac{1}{p_T\prime} = \frac{1}{p_T} + \delta_{K_T}(q, \phi, \eta) \tag{5.9}$$

$$\delta_{K_T}(q, \phi, \eta) = A + B\eta^2 + qC\sin(\phi - \phi_0) \tag{5.10}$$

where A = 0.236 TeV^{-1}, B = -0.135 TeV^{-1}, C = 0.282 TeV^{-1}, and $\phi_0 = 1.337$. The effect was found to have a less than 10% effect on the efficiency to pass the final selection.

The effect of the uncertainty on dE/dx was evaluated with low momentum protons. Protons with less p less than 2GeV will have speed appreciably lower than the speed of light and thus will appear similar to signal candidates. A comparison of data and MC yields an uncertainty of 0.05 on I_{as} and 5% on I_h.

94

These uncertainties give an uncertainty up to ?% when propagated to the final to the final selection.

The uncertainty on the number of proton-proton collisions per bunch cross is found by varying the proton-proton cross-section used to determine the number of interactions in data. This leads to an uncertainty of less than 4%.

Figure 5.39 shows the different sources of signal efficiency systematic uncertainty for the various signal models considered in the *muon only* analysis. Figure 5.40 and **??** shows the same for the *muon+track* analysis for stau and $R-hadron$ models, respectively. The total signal efficiency uncertainty for all considered models is shown in Figure 5.42 for both the *muon only* and *muon+track* analyses. The signal efficiency uncertainty used for each signal point is what is shown in this figure. The uncertainty for all signal points is less than 15% for all signal points and less than 10% for a large majority of signal points.

5.11   Final Results

No excess was observed over the expected background for any of the used selection points with the largest excess being 1.5 sigma observed in the *muon+track* analysis with a mass cut of 150 GeV. Considering the numerous different mass cuts used in the *muon+track* analysis this is consistent with a background only interpretation. Therefore, limits are placed on the production rate of various models of new physics. The statistical method of determining the limits is discussed in Section 5.8. Figure 5.43 shows the cross-section limits in both analyses for all considered models. The official CMS results for the *muon+track* analysis combines the 8 TeV data collected in 2012 with 7 TeV data collected in 2011. The combined result places limits on the relative signal strength, σ/σ_{th}. The 7
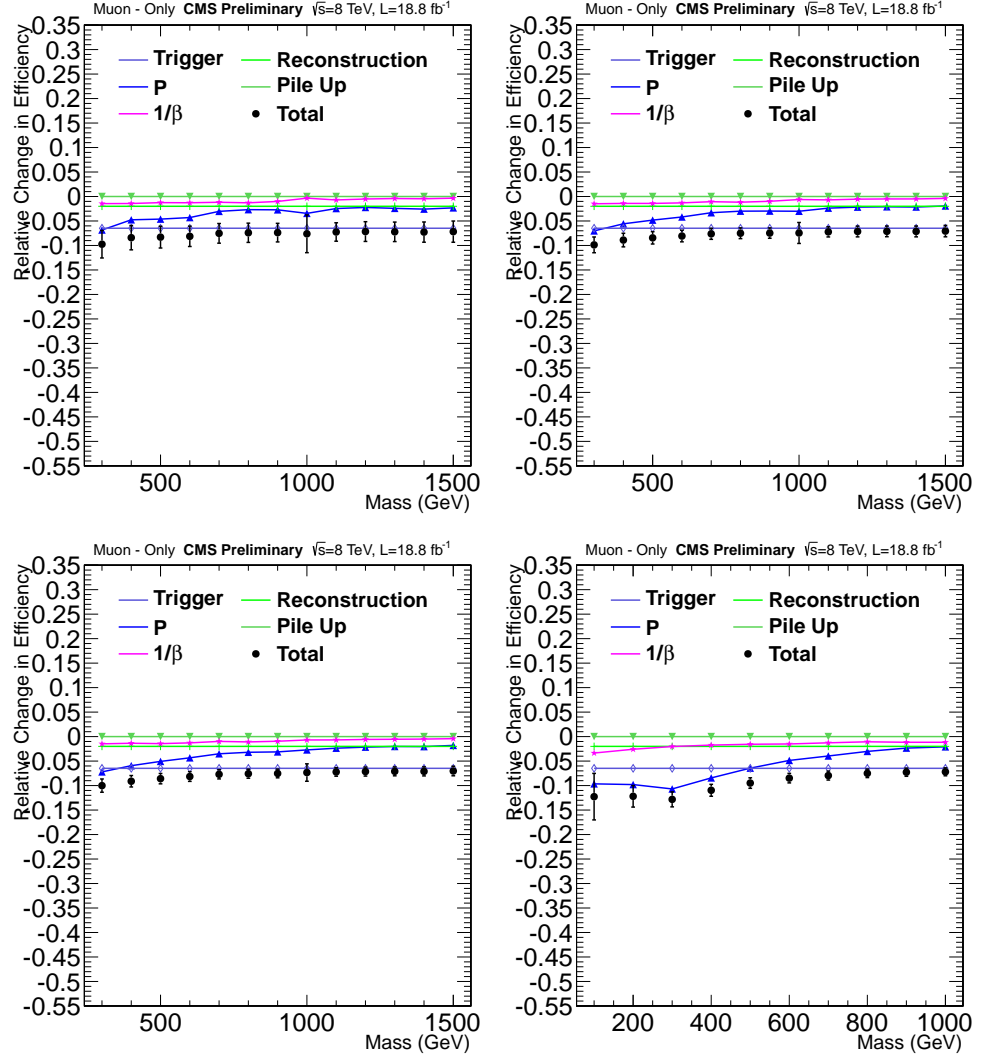
Figure 5.39: Relative efficiency change seen for the various sources of uncertainty in the *muon only* analysis. Top row: Gluino with $f = 1.0$ (left) and $f = 0.5$ (right). Bottom row: Gluino with $f = 0.1$ (left) and stop (right)
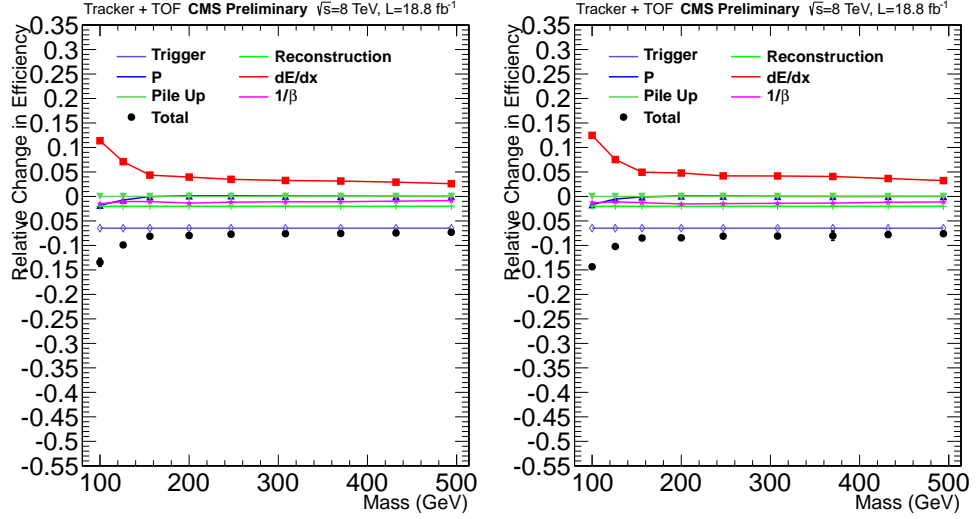
Figure 5.40: Relative efficiency change seen for the various sources of uncertainty for stau models in the *muon+track* analysis. GMSB (left) and PP (right) models.

TeV results are simply added here without further description. The limit on the relative cross-section for the *muon+track* analysis is shown in Figure 5.44.

Table 5.7 has the observed and predicted cross-sections for various signal points in the *muon only* analysis as well as the signal efficiency. Table 5.8 shows the same for the *muon+track* analysis adding in the limits on the relative signal strength.

Mass limits are placed on the various models by both analyses. The mass limit in the *muon only* analysis is found by the intersection of the observed limit with the center of the theoretical band. For the *muon+track* analysis it is found by where the limit on the relative signal strength crosses one. The *muon only* analysis gives mass limits of 1258, 1283, and 1300 GeV for gluino production with $f = 1.0$, $f = 0.5$, and $f = 0.1$, respectively. A mass limit on stop production is placed at 853 GeV. The *muon+track* analysis sets a mass limit on gluino production with
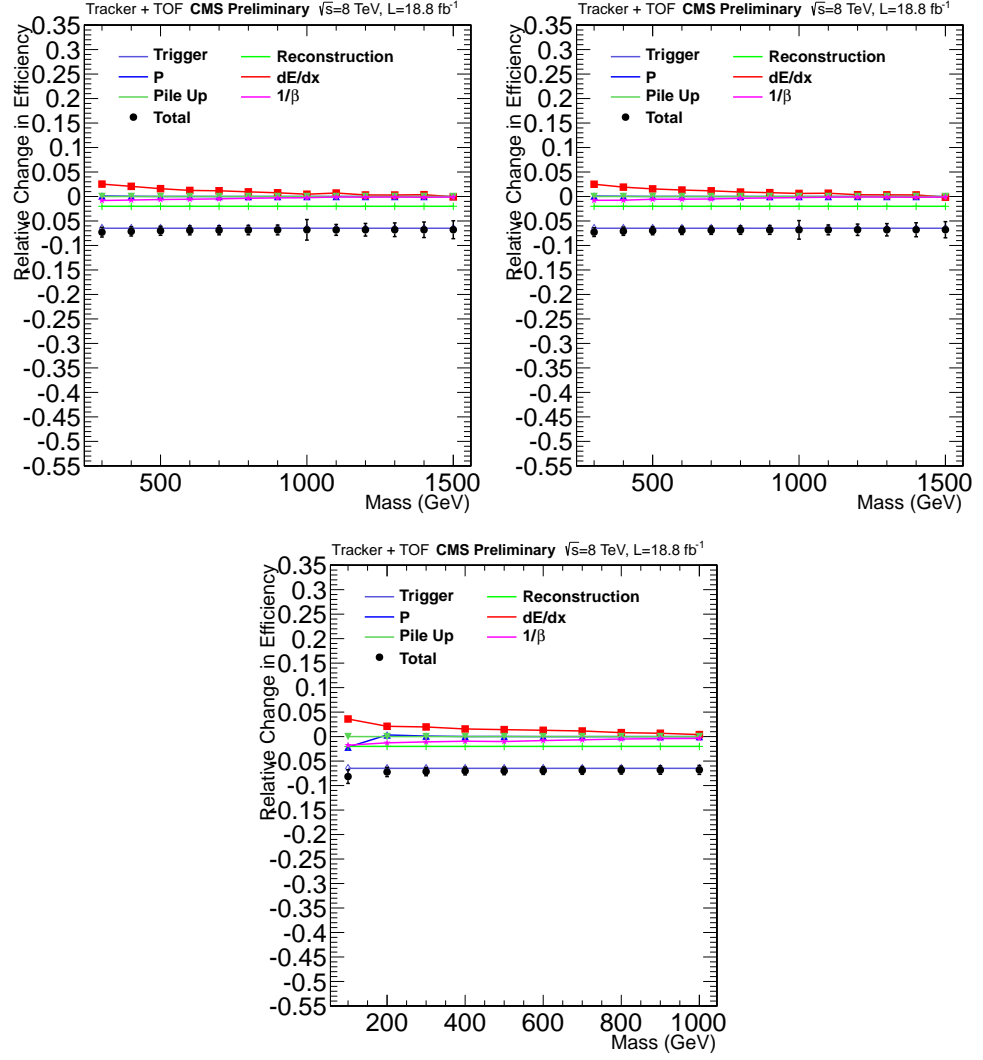
Figure 5.41: Relative efficiency change seen for the various sources of uncertainty for $R-hadron$ models in the $muon+track$ analysis. Top row: Gluino with $f = 0.5$ (left) and $f = 0.1$ (right). Bottom row: Stop

Figure 5.42: Total signal efficiency uncertainty for all considered models in the *muon only* (left) and *muon+track* (right) analyses.
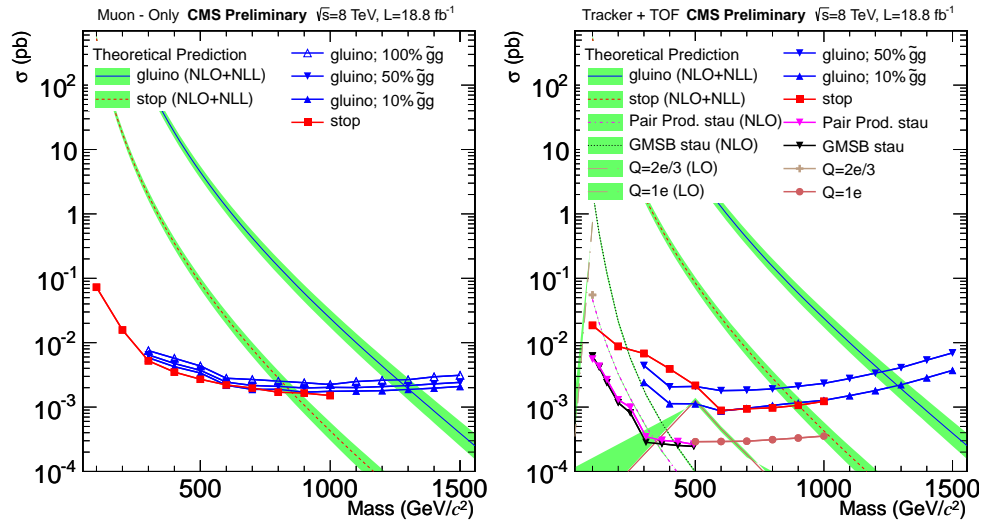
Figure 5.43: Cross-section limits for all considered models in the *muon only* (left) and *muon+track* (right) analyses.

Table 5.7: Summary table for the *muon only* analysis. $\sigma_{pred}(\sigma_{obs})$ is the expected(observed) cross section limits in *pb*.

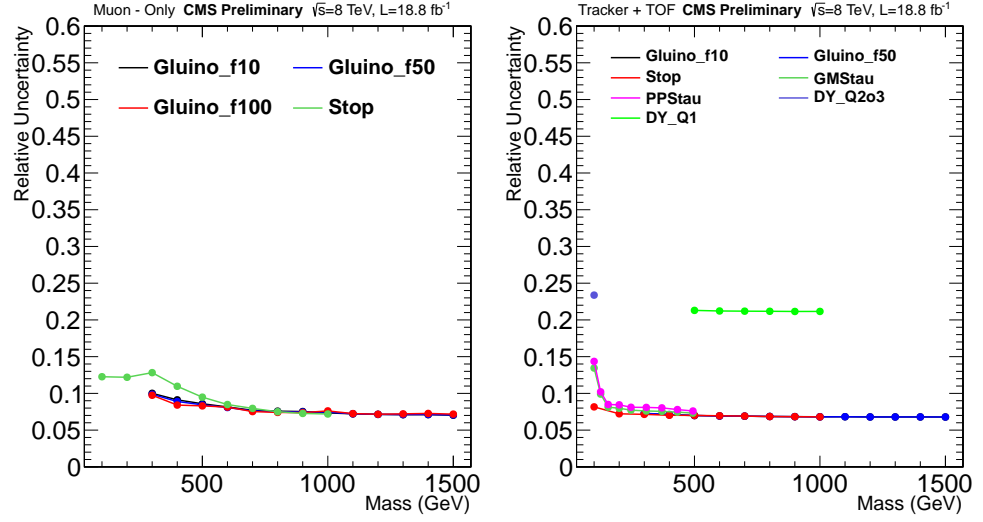| Sample	Mass		$\sqrt{s} = 8 TeV$		
	(GeV)	Eff	σ_{TH}	σ_{obs}	σ_{pred}
Gluino (f=1.0)	300	0.05	1.03E+02	7.65E-03	6.61E-03
Gluino (f=1.0)	500	0.08	4.46E+00	2.75E-03	3.87E-03
Gluino (f=1.0)	700	0.10	4.24E-01	2.70E-03	3.22E-03
Gluino (f=1.0)	900	0.11	5.88E-02	2.41E-03	2.93E-03
Gluino (f=1.0)	1100	0.11	1.00E-02	2.50E-03	3.03E-03
Gluino (f=1.0)	1300	0.10	1.93E-03	2.74E-03	3.28E-03
Gluino (f=1.0)	1500	0.09	3.93E-04	3.12E-03	3.80E-03
Gluino (f=0.5)	300	0.06	1.03E+02	6.52E-03	5.64E-03
Gluino (f=0.5)	500	0.10	4.46E+00	3.78E-03	3.25E-03
Gluino (f=0.5)	700	0.12	4.24E-01	2.23E-03	2.65E-03
Gluino (f=0.5)	900	0.14	5.88E-02	2.00E-03	2.41E-03
Gluino (f=0.5)	1100	0.13	1.00E-02	2.06E-03	2.45E-03
Gluino (f=0.5)	1300	0.12	1.93E-03	2.23E-03	2.65E-03
Gluino (f=0.5)	1500	0.11	3.93E-04	2.51E-03	2.98E-03
Gluino (f=0.1)	300	0.06	1.03E+02	5.85E-03	5.05E-03
Gluino (f=0.1)	500	0.11	4.46E+00	3.39E-03	2.93E-03
Gluino (f=0.1)	700	0.14	4.24E-01	1.95E-03	2.33E-03
Gluino (f=0.1)	900	0.15	5.88E-02	1.72E-03	2.13E-03
Gluino (f=0.1)	1100	0.15	1.00E-02	1.77E-03	2.13E-03
Gluino (f=0.1)	1300	0.14	1.93E-03	1.92E-03	2.29E-03
Gluino (f=0.1)	1500	0.13	3.93E-04	2.15E-03	2.55E-03
Stop	200	0.02	1.77E+01	1.58E-02	1.38E-02
Stop	400	0.08	3.51E-01	3.58E-03	4.21E-03
Stop	600	0.12	2.44E-02	2.20E-03	2.64E-03
Stop	800	0.15	2.82E-03	1.72E-03	2.13E-03
Stop	1000	0.18	4.27E-04	1.55E-03	1.86E-03

Table 5.8: Summary table for the *muon+track* analysis. $\sigma_{pred}(\sigma_{obs})$ is the expected(observed) cross section limits in *pb* and $\mu = \sigma/\sigma_{TH}$.

| Sample	Mass	Cut	$\sqrt{s} = 8 TeV$			$\sqrt{s} = 7 + 8 TeV$	
	(GeV)	(GeV)	Eff	σ_{TH}	σ_{obs}	σ_{pred}	μ_{obs}	μ_{pred}
Gluino (f=0.5)	300	> 110	0.07	1.03E+02	4.41E-03	4.07E-03	4.30E-05	3.10E-05
Gluino (f=0.5)	500	> 260	0.09	4.46E+00	2.14E-03	1.55E-03	3.65E-04	3.15E-04
Gluino (f=0.5)	700	> 400	0.09	4.24E-01	1.72E-03	1.69E-03	3.63E-03	3.56E-03
Gluino (f=0.5)	900	> 530	0.08	5.88E-02	2.09E-03	2.05E-03	3.14E-02	2.98E-02
Gluino (f=0.5)	1100	> 660	0.06	1.00E-02	2.72E-03	2.61E-03	2.43E-01	2.30E-01
Gluino (f=0.5)	1300	> 750	0.04	1.93E-03	4.09E-03	3.89E-03	1.92E+00	1.80E+00
Gluino (f=0.5)	1500	> 830	0.02	3.93E-04	6.88E-03	6.58E-03	1.68E+01	1.58E+01
Gluino (f=0.1)	300	> 110	0.14	1.03E+02	2.42E-03	2.23E-03	2.50E-05	1.70E-05
Gluino (f=0.1)	500	> 260	0.16	4.46E+00	1.20E-03	8.68E-04	2.03E-04	1.77E-04
Gluino (f=0.1)	700	> 410	0.16	4.24E-01	9.60E-04	9.25E-04	2.02E-03	1.97E-03
Gluino (f=0.1)	900	> 540	0.14	5.88E-02	1.15E-03	1.11E-03	1.71E-02	1.64E-02
Gluino (f=0.1)	1100	> 660	0.11	1.00E-02	1.48E-03	1.42E-03	1.31E-01	1.25E-01
Gluino (f=0.1)	1300	> 750	0.07	1.93E-03	2.21E-03	2.11E-03	1.06E+00	9.84E-01
Gluino (f=0.1)	1500	> 830	0.04	3.93E-04	3.67E-03	3.51E-03	8.71E+00	7.98E+00
Stop	200	> 0	0.12	1.77E+01	8.76E-03	8.51E-03	4.02E-04	2.61E-04
Stop	400	> 80	0.16	3.51E-01	3.96E-03	2.82E-03	7.25E-03	5.49E-03
Stop	600	> 210	0.18	2.44E-02	9.36E-04	8.94E-04	3.11E-02	2.98E-02
Stop	800	> 370	0.17	2.82E-03	9.91E-04	9.25E-04	2.92E-01	2.75E-01
Stop	1000	> 530	0.13	4.27E-04	1.20E-03	1.18E-03	2.36E+00	2.26E+00
GMSB Stau	100	> 20	0.16	2.28E+00	6.16E-03	6.32E-03	2.16E-03	2.45E-03
GMSB Stau	126	> 40	0.25	4.96E-01	4.15E-03	4.24E-03	6.38E-03	7.46E-03
GMSB Stau	156	> 70	0.32	1.21E-01	2.35E-03	1.73E-03	1.74E-02	1.32E-02
GMSB Stau	200	> 110	0.41	2.15E-02	1.18E-03	7.59E-04	5.60E-02	3.20E-02
GMSB Stau	247	> 150	0.50	5.75E-03	8.20E-04	4.49E-04	1.60E-01	6.83E-02
GMSB Stau	308	> 190	0.56	1.56E-03	2.94E-04	2.94E-04	2.18E-01	1.62E-01
GMSB Stau	370	> 240	0.60	5.64E-04	2.68E-04	2.60E-04	3.99E-01	3.80E-01
GMSB Stau	432	> 290	0.64	2.34E-04	2.50E-04	2.36E-04	9.37E-01	8.61E-01
GMSB Stau	494	> 330	0.66	1.06E-04	2.43E-04	2.33E-04	1.92E+00	1.90E+00
PP Stau	100	> 20	0.17	4.70E-02	5.98E-03	6.11E-03	9.98E-02	1.08E-01
PP Stau	126	> 40	0.24	2.02E-02	4.30E-03	4.37E-03	1.50E-01	1.83E-01
PP Stau	156	> 60	0.28	9.02E-03	2.68E-03	2.37E-03	2.31E-01	2.10E-01
PP Stau	200	> 100	0.34	3.27E-03	1.30E-03	9.97E-04	4.13E-01	2.63E-01
PP Stau	247	> 140	0.40	1.37E-03	9.63E-04	6.01E-04	8.56E-01	3.75E-01
PP Stau	308	> 190	0.46	5.03E-04	3.40E-04	3.56E-04	6.16E-01	6.24E-01
PP Stau	370	> 240	0.53	2.08E-04	3.09E-04	2.97E-04	1.38E+00	1.16E+00
PP Stau	432	> 280	0.57	9.40E-05	2.82E-04	2.66E-04	2.54E+00	2.40E+00
PP Stau	494	> 330	0.61	4.50E-05	2.69E-04	2.52E-04	4.89E+00	4.71E+00
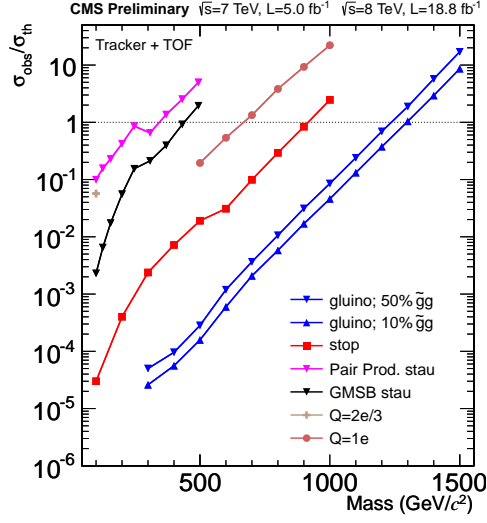
Figure 5.44: Limits on the relative signal strength, σ/σ_{th}, for all considered models in the *muon+track* analysis.

$f = 0.5$ ($f = 0.1$) of 1224 (1291) GeV. A limit on stop production is placed at 910 GeV. A limit of 435 and 339 GeV is placed on stau production in the GMSB and pair production models respectively.

The limits represent the most stringent limits in the world to date except for the gluino $f = 0.1$ and stop models where a variant of this analysis performed by CMS gives slightly better limits.

5.12   Conclusion

Two analyses were performed searching for heavy long-lived charged particles in proton-proton collision data collected by CMS. One search only requires the particle be found in the outer muon system allowing it to be sensitive to particles produced neutral and only becoming charged by interacting with the detector. The second analysis looks for particles reconstructed in both the inner tracker

and the muon system. This analysis is especially powerful lepton-like long-lived particles which will always be charged during the entirety of its passage through the CMS detector. The signatures of new long-lived charged particles, long time of flight, high momentum, and large ionization energy loss, are used to separate the signal from the large Standard Model background. A data-driven procedure is used to estimated the Standard Model background in the final selection region. Data are found to agree with the predicted background and limits are placed on the production rates of various models of new physics that predict the existence of long-lived particles. Most of the limits are the best produced to date and put important constraints on physics beyond the Standard Model.

CHAPTER 6

Conclusion

Give me a PhD.

References

[1] M. Fairbairn et Stable massive particles at , Phys. Rept. 438 (2007) 1, doi:10.1016/j.physrep.2006.10.002, arXiv:hep-ph/0611040.collidersal.,

[2] Beringer, J. and others "Review of Particle Physics (RPP)" Phys. Rev. **D86** (2012) 010001

[3] Chatrchyan et al. "Search for heavy long-lived charged particles in pp collisions at $\sqrt{s}$=7 TeV" Phys. Lett. **B713** (2012) 408

[4] "Need to cite something here"

[5] CMS Collaboration "Jet Performance in pp Collisions at $\sqrt{s}$=7 TeV" CMS Physics Analysis Summary CMS-PAS-JME-10-003 (2010)

[6] L. Evans and P. Bryant "LHC Machine" JINST 3 (2008) S08001.

[7] S. Chatrchyan et al., "The CMS experiment at the CERN LHC," JINST **3** (2008) S08004.

[8] G. L. Bayatian et al., "CMS physics: technical design report,",

[9] N. Arkani-Hamed and S. Dimopoulos, "Supersymmetric unification without low energy supersymmetry and signatures for fine-tuning at the LHC", JHEP 06 (2005) 073, doi:10.1088/1126-6708/2005/06/073, arXiv:hep-th/0405159.

[10] G. Giudice and A. Romanino, "Split supersymmetry" Nucl. Phys. B 699 (2004) 65-89 doi:10.1016/j.nuclphysb.2004.11.048, arXiv:hep-ph/0406088

[11] G. F. Giudice and R. Rattazzi "Theories with gauge mediated supersymmetry breaking", Phys. Rept. 322 (1999) 419-499, arXiv:hep-ph/9801271

[12] B. Allanach et al., "The Snowmass points and slopes: Benchmarks for SUSY searches", Eur. Phys. J. C 25 (2002) 113-123 doi:10.1007/s10052-002-0949-3, arXiv:hep-ph/0202233.

[13] T. Sjostrand, S. Mrenna, and P. Z. Skands "PYTHIA 6.4 Physics and Manual", JHEP 05 (2006) 026, doi:10.1088/1126-6708/2006/05/026, arXiv:hep-ph/0603175.

[14] F. E. Paige et al., "ISAJET 7.69: A Monte Carlo event generator for SUSY pp, and e^+e^- reactions", arXiv:hep-ph/0312045.

[15] J. Heisig and J. Kersten "Production of long-lived staus in the Drell-Yan Process", Phys.Rev. D84 (2011) 115009, doi:10.1103/PhysRevD.84.115009, arXiv:1106.0764.

[16] A. L. Read, "Modified frequentist analysis of search results (The CL(s) method)".

[17] W. T. Eadie et al., "Statistical Methods in Experimental Physics", North Holland, Amsterdam, 1971,

[18] F. James, "Statistical Methods in Experimental Physics", World Scientific, Singapore, 2006.

[19] A. C. Interactions of heavy stable hadronizing , Eur. Phys. J. C37 (2004) 91, doi:10.1140/epjc/s2004-01997-7, arXiv:hep-ex/0404001.

[20] R. Mackeprang and A. Interactions of coloured heavy stable particles in , Eur. Phys. J. C50 (2007) 353, doi:10.1140/epjc/s10052-007-0252-4, arXiv:hep-ph/0612161.matterRizzi, particlesKraan,

[21] R. Mackeprang and D. An updated description of heavy-hadron interactions in , Eur. Phys. J. C 66 (2010) 493, doi:10.1140/epjc/s10052-010-1262-1, arXiv:0908.1868.GEANT4Milstead,